VYSOKÉ UČENÍ TECHNICKÉ V BRNĚ

Fakulta strojního inženýrství

DIPLOMOVÁ PRÁCE

Brno, 2017 Bc. Antonín Sojka

VYSOKÉ UČENÍ TECHNICKÉ V BRNĚ
BRNO UNIVERSITY OF TECHNOLOGY

FAKULTA STROJNÍHO INŽENÝRSTVÍ
FACULTY OF MECHANICAL ENGINEERING

ÚSTAV FYZIKÁLNÍHO INŽENÝRSTVÍ
INSTITUTE OF PHYSICAL ENGINEERING

NÍZKOTEPLOTNÍ RASTROVACÍ TUNELOVÁ MIKROSKOPIE
LOW TEMPERATURE SCANNING TUNNELING MICROSCOPY

DIPLOMOVÁ PRÁCE
MASTER'S THESIS

AUTOR PRÁCE — **Bc. Antonín Sojka**
AUTHOR

VEDOUCÍ PRÁCE — **Ing. Michal Pavera, Ph.D.**
SUPERVISOR

BRNO 2017

VYSOKÉ UČENÍ TECHNICKÉ V BRNĚ
FAKULTA STROJNÍHO INŽENÝRSTVÍ

Zadání diplomové práce

Ústav:	Ústav fyzikálního inženýrství
Student:	**Bc. Antonín Sojka**
Studijní program:	Aplikované vědy v inženýrství
Studijní obor:	Fyzikální inženýrství a nanotechnologie
Vedoucí práce:	**Ing. Michal Pavera, Ph.D.**
Akademický rok:	2016/17

Ředitel ústavu Vám v souladu se zákonem č.111/1998 o vysokých školách a se Studijním a zkušebním řádem VUT v Brně určuje následující téma diplomové práce:

Nízkoteplotní rastrovací tunelová mikroskopie

Stručná charakteristika problematiky úkolu:

Dosažení velmi nízkých teplot v rastrovacích tunelových mikroskopech je zcela zásadní pro měření mnohých fyzikálních veličin a procesů. Příkladem může být měření hustoty stavů jako funkce energie pomocí rastrovací tunelové spektroskopie či magnetického uspořádání studovaných materiálů pomocí spinově–polarizované rastrovací tunelové mikroskopie.
Náplní diplomové práce je upravit stávající ultravakuový rastrovací tunelový mikroskop (STM) pro provoz při nízkých teplotách a testovat jej na vybraných systémech.

Cíle diplomové práce:

1. Popište základní fyzikální principy funkce STM a konstrukci nízkoteplotního STM
2. Proveďte konstrukční návrh úpravy stávajícího mikroskopu pro provoz v prostředí UHV a za nízkých teplot
3. Proveďte experimenty na vybraných materiálových systémech (např. Ir–Nb, Ir–V) pomocí nízkoteplotního STM.

Seznam doporučené literatury:

MEYER, E., HUG, H. J. a BENNEWITZ, R. Scanning probe microscopy: the lab on a tip. New York: Springer, c2004. ISBN 3540431802.

VŮJTEK, M., KUBÍNEK, R. a MAŠLÁŇ, M. Nanoskopie. V Olomouci: Univerzita Palackého, 2012. ISBN 978-80-244-3102-4.

HARNA, Z. Přesná mechanika. Brno: Vysoké učení technické, 1996. ISBN 80-214-0794-8.

ABSTRACT

The diploma thesis is divided into two main parts. The first part describes the production of chrome and cobalt tips for SP-STM with subsequent testing of chrome tips on the Fe-Ir system (111). Furthermore, the first results from the growth studies of niobium on iridium(111) are presented. In the second part is described in detail the experimental LT-STM microscope of the Faculty of Physical Engineering. The chapter deals with the development of the microscope and its testing on a HOPG sample under atmospheric and vacuum conditions. The chapter describes the biggest problems which were solved when the microscope was puting into operation state. The second part also introduces the design of a new vacuum transport system, which consists of a tip and sample transport pallet. At the end of the second part is described the testing of cooling systems for LT-STM and the design of their modifications.

KEYWORDS

low temperature scanning tunneling microscopy, LT-STM, spin polarized scanning tunneling microscopy, SP-STM, STM tips fabrication, electrochemical tip etching, chromium tips, cobalt tips, cryogenics, UHV, magnetism, iron, nanoskyrmion, Ir(111), Niobium, vacuum transport system, highly oriented pyrolytic graphite, HOPG

ABSTRAKT

Diplomová práce je rozdělena do dvou částí. První část pojednává o výrobě chromových hrotů pro SP-STM s následným testování chromových hrotů na systému Fe-Ir(111). Dále jsou v první části uvedené výsledky z růstových studií niobia na iridiu(111). Ve druhé části je detailně popsán experimentální LT-STM mikroskop fakulty Fyzikálního inženýrství. V kapitole je popsán vývoj mikroskopu a jeho testování na vzorku HOPG při atmosférických podmínek a ve vakuu. Kapitola uvádí největší problémy, který se při zprovozňování mikroskopu projevily a také jejich řešení. V druhé části je také uveden design nového transportní systému do vakua, který se skládá z paletky na transport hrotu a vzorku. V závěru druhé části je popsáno testování chladících systémů pro LT-STM a návrh jejich úprav.

KLÍČOVÁ SLOVA

nízko teplotní skenovací tunelová mikroskopie, LT-STM, spinové polarizovaná skenovací tunelovací mikroskopie, SP-STM, výroba STM hrotů, elektrochemické leptání hrotů, chromiové hroty, kobaltové hroty, kryogenika, UHV, magnetismus, železo, nanoskyrmiony, Ir(111), Niobium, vakuový transportní systém, vysoce orientovaný pyrolytický grafit, HOPG

SOJKA, Antonín *Nízkoteplotní rastrovací tunelová mikroskopie*: bachelor's thesis. Brno: Brno University of Technology, Faculty of Mechanical Engineering, Ústav fyzikálního inženýrství, 2017. 76 p. Supervised by Ing. Michal Pavera

DECLARATION

I declare that I have elaborated my bachelor's thesis on the theme of "Nízkoteplotní rastrovací tunelová mikroskopie" independently, under the supervision of the bachelor's thesis supervisor and with the use of technical literature and other sources of information which are all quoted in the thesis and detailed in the list of literature at the end of the thesis.

Brno ....

(author's signature)

Poděkování

Děkuji svému vedoucímu Ing. Michal Pavera, Ph.D. za trpělivost, vedení a rady při tvorbě této diplomové práce. Dále děkuji celé FSI skupině za nespočetné rady a pomoc s řešením určitých problému. Chtěl bych také poděkovat svým kolegům ze společnosti FEI, za pomoc jak s anglickou stránkou mojí práce, tak za nespočetné rady a schovívavost při nepravidelné pracovní docházce. Rád bych poděkoval prof. Alexi Ako Khajetoorians celému tým SPM skupiny na Radboud University za možnost pracovat ve špičkových laboratořích. Nakonec bych rád poděkoval své rodině a všem přátelům, bez kterých by tato práce nevznikla, za jejich podporu a trpělivost během celého mého studia.

Bc. Antonín Sojka

CONTENTS

INTRODUCTION

Scanning tunneling microscope belongs to a group of microscopes where the resolution is independent of diffraction limit [1]. This means that the resolution does not depend on the wavelength of the probe, such as the light in the optical microscopes or the electrons in the electron microscopes, but on the shape of the scanning probe [2]. As the predecessor of the tunneling electron microscopy was the topographer invented by Young and el. [3]. The microscope used tunneling of electrons to generate current between the probe and the tip. However, to achieve the atomic resolution the distance of the probe and the sample has to be around 1 nm [1]. Young et al. have failed to solve the major problem with the isolation of vibrations which is critical for approaching the probe close to the sample. Therefore, the resolution of the topographer was in orders of μm [3]. The vibration problems were firstly solved in 1981, by Binnig and Röhrer [4]. By new improvements the distance between the tip and the sample was reduced to dozens of nanometers. The microscope was named Scanning Tunneling Microscope (STM) and it was the first microscope which was able to image an atomic resolution in real time. Thanks to that, STM became very popular in the field of surface science in the following years. Shortly after the invention, new scanning probes methods like Atomic Force Microscopy (AFM), Magnetic Force Microscopy (MFM), Near Field Scanning Optical Microscopy (NSOM) and others were developed [5].

This work focuses on working with the two types of Low Temperature Scanning Tunneling Microscopes (LT-STM), the Omicron LT-STM and experimental LT-STM at the Institute of Physical Engineering at Brno University of Technology. For this reason the work can be divided into two main parts:

1. Study of superconducting-magnetic interface using STM (Chapter 4)
2. Development and testing of experimental LT-STM (Chapter 5 and Chapter 6)

The first chapter of this work focus on the introduction into the basics of the STM microscope. In this chapter the overview of STM, basic theory of tunneling effect and use of various STMs in different fields of science is discussed.

In the second and third chapters, attention is to paid to a certain part of the microscope design, such as the motion system, the vibration damping system, the tip production in the (chapter 2) and the problems with construction of components into a UHV (chapter 3).

Chapter four discusses the work that was done in the SPM group of Dr. Khajetorian in Nijmegen in the Netherlands. The first part of the chapter introduces the project of the study superconducting-magnetic interfaces and describes the LT-STM system, at which majority of work was done. Second part of the chapter focuses on the production of the chromium tips, followed by testing of the tips on the Fe-Ir(111) system. At the end of the chapter the growth study of the Niobium on Iridium is investigated.

The last two chapters (chapter 5 and chapter 6) are focused on the development and testing of the experimental STM microscope at the Institute of Physical Engineering in Brno. In Chapter 5, the system is described in details and also the proposals for a new transtport system of the samples and the tips are presented here. In the Chapter 6 the tests of the experimental STM in air and vacuum conditions are presented. In the last chapter the test of the cooling systems with two different cryostats is shown - the flow cryostat and the stationary cryostat.

1 TUNNELING MICROSCOPY THEORY

1.1 Overview

The Scanning Tunneling Microscope (STM) was invented by Binnig and Röhrer in 1981 [4]. The STM invention was awarded in the year 1986 by Nobel price [6].

A schematic of the basic principle of the STM microscope is shown in Figure 1.1. The basic principle of STM is based on the quantum effect called quantum tunneling. The quantum tunneling is a process of electron penetration through the barrier (space) between the probe and the sample. To achieve quantum tunneling, the distance between the probe and the sample has to be in the range of several nanometers, which is achieved by a scanner. [4]. It is device that ensures movement in the three axes and the probe, usually called the tip, is attached to a it. Ideally, the quantum tunneling occurs between one atom of the tip and one atom of the sample. Therefore, atomic resolution can be achieved.

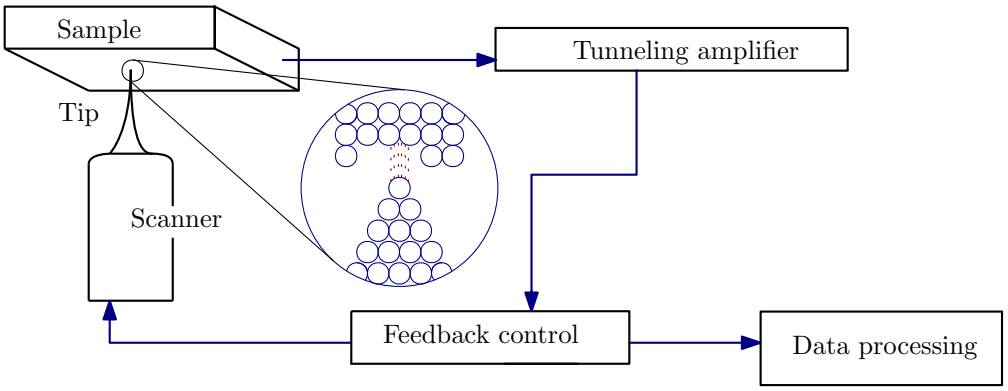

Figure 1.1: Schematic of the Scanning Tunneling Microscope. The basic STM is composed of the tip attached on the scanner, which provides the movement of the tip above sample surface. The measured tunneling current which occurs between the sample and the tip is amplified. By feedback controller the tunneling current is regulated or kept constant. The final STM image is composed from the 2-D map of the z position of the scanner.

However, electrons can tunnel through the barrier only if unoccupied electron states are available on the other side. Therefore the local density of states (LDOS) determines the amount of the tunneling current [7]. In the absence of an external field, the probability for electrons to tunnel from the sample to the tip, and in the opposite direction, is equal, and thus no tunneling current is measured. By applying a bias voltage V_{bias} one direction of the tunneling current is dominated. Typically, the tip is grounded and the bias is connected to the sample. If $V > 0$, the electrons are tunneling from the occupied state of the tip into the empty states of the sample and when $V < 0$ the situation is vice versa.

Moreover, if the tip scans the sample in the xy-plane, the distance between the sample and the tip is recorded and a 2-D map corresponding to the topography of the sample is formed (Figure 1.2). Typically the topography is displayed on a computer screen as a gray scale image (Figure 1.2 (a)). For a more quantitative representation of the topography, a contour plot along a given line is often provided, as shown in Figure 1.2 (b). Usually the bright spots correspond to higher features on the sample. Because the tunneling current does not depend only on the topography but also on

the LDOS, the interpretation of an image where two materials are present is not straightforward. The bright feature in the STM image may appear as a high spot, but in the reality it corresponds to a different material with higher LDOS.

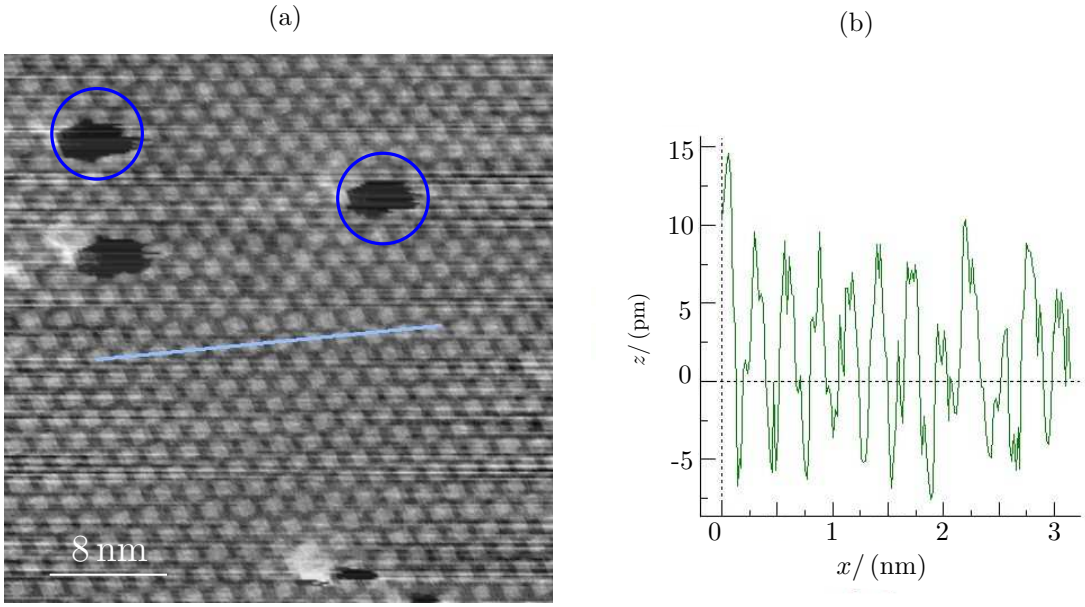

Figure 1.2: Grey-scale image and contour plot. (a) Topographic image of the Ir(111) surface. The bright spots represent protrusions and the dark spots represent lower areas. By blue circles are marked the missing atoms in the lattice. (b) The topographic contour along the blue line in the (a) for more quantitative representation.

1.2 Fundamentals of Tunneling

Contrary to classical mechanics, quantum mechanics allows electrons to penetrate into a barrier region with higher energy than its own.

A classical-mechanical model describes electron in electric field with potential $U(z)$ by [8]

$$\frac{p^2}{2m} + U(z) = E, \tag{1.1}$$

where p is the electron momentum, m is the electron mass and E is energy of the electron, which is smaller than U. According to classical mechanics, the electron cannot penetrate into any region with $E < U$. In contrast, according to quantum mechanics, it is possible for an electron to penetrate into an energy barrier higher than the electron's energy.

In 1926, E. Schrődinger published his work *Quantisierung Als Eigenwertproblem* in which he built the fundamentals of the Quantum Physics [10]. He based his work on the pre-condition given by Louis de Broglie [8], which states that a free particle can be associated with a plane monochromatic wave function of the form

$$\Psi\left(\vec{r}, t\right) = C \exp\left[-\mathrm{i}\left(\omega t - \vec{k}\cdot\vec{r}\right)\right], \tag{1.2}$$

where C is amplitude of the wave, $\vec{r}$ is position, ω is angular frequency, and $\vec{k}$ is angular wavenumber. De Broglie's precondition redefined modern physics and said that any particle can behave like a wave. In 1927, Davisson and Germer confirmed the de Broglie hypothesis experimentally [9].

The wave function Ψ does not have any physical interpretation, but its complex square gives the probability of finding the particle at a given location

$$\mathrm{d}P(\vec{r},t) = |\Psi(\vec{r},t)|^2 \,\mathrm{d}\tau, \tag{1.3}$$

where, $\mathrm{d}\tau = \mathrm{d}x\,\mathrm{d}y\,\mathrm{d}z$ is elementary volume. Because the particle has to be somewhere, integration over the entire space gives the total probability of 1

$$\iiint_{-\infty}^{\infty} |\Psi(\vec{r},t)|^2 \,\mathrm{d}\tau = 1. \tag{1.4}$$

The quantum mechanic solution of the Schrődinger equation describes the particle (in our case an electron) by a wave function $\Psi(z)$ [10]

$$\mathrm{i}\hbar\frac{\partial\Psi(\vec{r},t)}{\partial t} = -\frac{\hbar^2}{2m}\,\Delta\Psi(\vec{r},t) + V(\vec{r},t)\,\Psi(\vec{r},t)\,, \tag{1.5}$$

where, V is potential energy, and Δ is Laplace operator. When the V is independent on the time, the equation 1.5 can be solved using separation of variables

$$\Psi(\vec{r},t) = f(t)\,\varphi(\vec{r})\,. \tag{1.6}$$

Then derivation of function $f(t)$ is equal to

$$\frac{\mathrm{d}f(t)}{\mathrm{d}t} = -\frac{\mathrm{i}}{\hbar}Ef(t)\,, \tag{1.7}$$

and for function $\varphi(\vec{r})$

$$-\frac{\hbar^2}{2m}\Delta\varphi(\vec{r}) + V(\vec{r})\,\varphi(\vec{r}) = E\varphi(\vec{r})\,. \tag{1.8}$$

Equation 1.8 is called stationary (time independent) Schrődinger equation [10]. The exact analytic solution has been found only for a few examples where potential $V(\vec{r})$ has specific shape. For other forms of $V(\vec{r})$, solutions have to be found using numerical methods.

1.2.1 Transmission Coefficient

In Figure 1.3 a potential energy barrier (area II) represents the space between the tip (area I) and the sample (area III) in the STM. By solving the stationary Schrődinger equation 1.8, basic principle of STM can be described. The potential in Figure 1.3 is divided into three parts:

$$V(x) = \begin{cases} 0, & x < 0 \qquad \text{(area I)} \\ V_0, & 0 \le x \le a \quad \text{(area II)} \\ 0, & a < x \qquad \text{(area III)} \end{cases}$$

The sample and STM tip can be represented by the areas I and III, where, in the absence of any external bias, the electrons are at the Fermi level [11], which is conventionally taken to be at zero potential.

Thanks to the tunneling effect electrons from area I and III can cross the barrier in area II [10]. Calculations of the final solution are done separately and for simplicity, only one dimensional distribution of electrons is considered (in the x-direction). From equation (1.8) is obtained

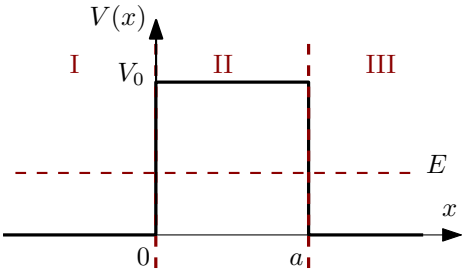

Figure 1.3: The scheme of the potential barrier. The area I represents the tip, area III represents the sample and the area II represents space barrier with width a and potential V_0 between them. The energy E represents the energy of an electron which is moving from left to right.

$$\frac{\mathrm{d}^2\varphi(x)}{\mathrm{d}x^2} + \frac{2m}{\hbar^2}\left[E - V(x)\right]\varphi(x) = 0. \tag{1.9}$$

The solution of stationary equation for area I, II and III are found in form

$$\varphi_{\mathrm{I}}(x) = A\exp(\mathrm{i}kx) + B\exp(-\mathrm{i}kx), \tag{1.10}$$

$$\varphi_{\mathrm{II}}(x) = C\exp(-\alpha x) + D\exp(\alpha x), \tag{1.11}$$

$$\varphi_{\mathrm{III}}(x) = F\exp(\mathrm{i}kx) + G\exp(-\mathrm{i}kx). \tag{1.12}$$

For areas I and III the parameter k is defined

$$k = \frac{\sqrt{2m(E-V)}}{\hbar} = \frac{\sqrt{2mE}}{\hbar} > 0. \tag{1.13}$$

Because the potential in areas I and III is zero, the term V inside the square root can be neglected. In area II the energy of electron E is smaller than potential V_0, therefore the $V_0 - E > 0$ and the parameter α is defined

$$\alpha = \frac{\sqrt{2m(V_0-E)}}{\hbar} > 0. \tag{1.14}$$

The constants A, B, C, D, and F from equation 1.10 - 1.12 are determined by using conditions of continuity of the functions and their first derivatives at the interface $x = 0$ and $x = a$:

$$\varphi_{\mathrm{I}}(0) = \varphi_{\mathrm{II}}(0) \quad \text{and} \quad \varphi_{\mathrm{II}}(a) = \varphi_{\mathrm{III}}(a), \tag{1.15}$$

$$\left.\frac{\mathrm{d}\varphi_{\mathrm{I}}(x)}{\mathrm{d}x}\right|_{x=0} = \left.\frac{\mathrm{d}\varphi_{\mathrm{II}}(x)}{\mathrm{d}x}\right|_{x=0} \quad \text{and} \quad \left.\frac{\mathrm{d}\varphi_{\mathrm{II}}(x)}{\mathrm{d}x}\right|_{x=a} = \left.\frac{\mathrm{d}\varphi_{\mathrm{III}}(x)}{\mathrm{d}x}\right|_{x=a}. \tag{1.16}$$

Only one direction of propagation of function φ (in the x direction) is considered. The wave is transmitted and reflected at the interfaces of areas I/II and II/III (Figure 1.4). Parameter G is equal to zero for area III because no other reflection barrier is present.

By putting equation (1.10),(1.11) and (1.12) to the condition of continuity of the function (1.15) and of first the derivative (1.16), the following equations are found

$$A + B = C + D, \tag{1.17}$$

$$\mathrm{i}k(A - B) = -\alpha(C - D), \tag{1.18}$$

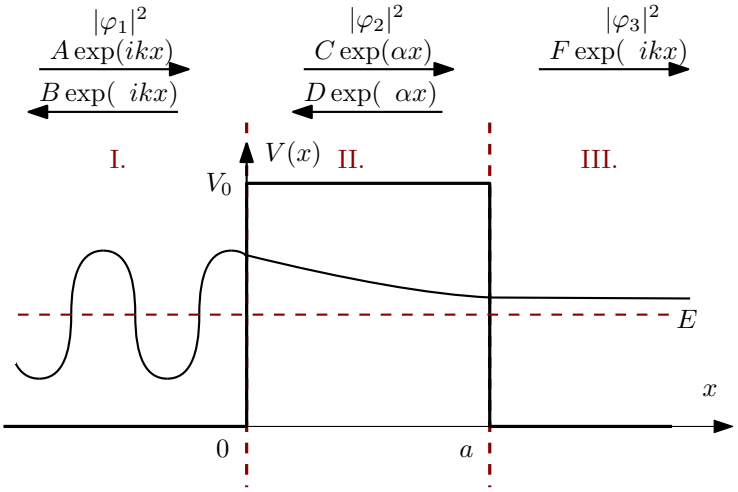

Figure 1.4: The probability function in the individual areas. The coefficient G in the solution for area III is zero because of propagation wave function φ_{III} is only in one direction.

$$C\exp(-\alpha a) + D\exp(\alpha a) = F\exp(\mathrm{i}ka), \tag{1.19}$$

$$-\alpha(C\exp(-\alpha a) - D\exp(\alpha a)) = \mathrm{i}kF\exp(\mathrm{i}ka). \tag{1.20}$$

Probability of electron penetration T is equal to ratios of probabilities of wave function in selected areas

$$T = \frac{|\varphi_{\mathrm{III}}(x)|^2}{|\varphi_{\mathrm{I}}(x)|^2} = \frac{|F|^2}{|A|^2}. \tag{1.21}$$

By applying solution from equation (1.17-1.20) to equation (1.21) transmission probability of electron through potential barrier is equal to [12]

$$T = \frac{16E}{V_0}\left(1 - \frac{E}{V_0}\right)\exp\left(-2\alpha a\right), \tag{1.22}$$

Equation (1.22) describes the penetration of electron through barrier. The probability decreases exponentially with size of the barrier, in case of STM with distance between the tip and the sample.

After the elementary model was introduced, it is possible to explain some basic features of metal-vacuum-metal tunneling. Starting from this elementary model tip (metal)-vacuum-sample (metal), we can explain some basic features of tunneling. Firstly, the work function Φ shown in the Figure 1.5 has to be defined. The work function is a minimum energy required to remove electron from the bulk to the vacuum level [7]. In general, work function depends on the material but in close view also crystallographic orientation can influence it. Without thermal excitation, Fermi energy E_F is upper limit of occupied states in metal. If the vacuum level is taken as the reference point of energy, then work function is equal: $\Phi = -E_{F,sample}$ [11].

When the surroundings of the tip and sample are the same, their work functions are equal and probability of tunneling of the electron through the barrier from the sample to the tip and vice versa are the same. After applying a voltage between the sample and the tip a tunneling current occurs. In close view, the electron with sample state Ψ_n and energy E_n which lies between $E_{F,sample}$ and $E_{F,tip}$ has an opportunity to tunnel into the tip (Figure 1.5). It is assumed that applied voltage is much smaller than the value of work function. That means energy levels which

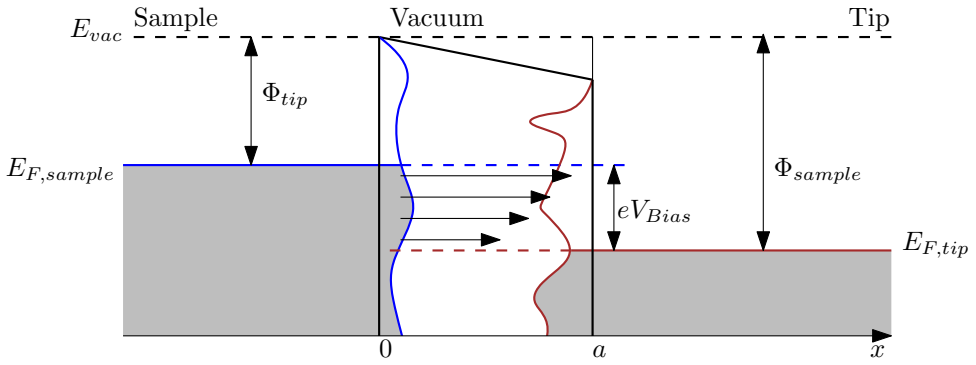

Figure 1.5: The sample, left, and the tip, right, are modeled as semi-infinite pieces of free-electron metal. When the distance a is small, the electrons of a sample state can penetrate into the region of the tip. By applying a bias voltage eV_{Bias}, the sample states between energy level $E_{F,sample}$ and $E_{F,tip}$ can tunnel to the tip, generating a tunneling current proportional to the bias voltage V_{Bias}.

provide tunneling electrons are very close to Fermi level $E_n \approx -\Phi_{sample}$. Using these arguments, transmission coefficient T (equation 1.22), which is the ratio of tunneling current from the tip at distance $x = a$ to the input current at the sample $x = 0$, can be simplified

$$\alpha = \frac{\sqrt{2m\Phi}}{\hbar}. \tag{1.23}$$

If the eV is used as the unit for the work function and nm^{-1} is used as the unit for the decay constant, then 1.23 can be simplified to:

$$\alpha = 5.1\sqrt{\Phi(\mathrm{eV})}\,\mathrm{nm}^{-1} \tag{1.24}$$

In the table 1.1 values of work functions Φ of materials used in STM experiments with the values of decay constant κ are shown. Average value of work function is $\phi \approx 5\,\mathrm{eV}$ which gives average value of decay constant $\kappa \approx 11.4\,\mathrm{nm}^{-1}$. According to the equation (1.22) the current decays by factor 9.78 by increasing the distance of 0.1 nm [7].

Table 1.1: Work functions and decay constants. Taken from [7].

Element	Al	Au	Cu	Ir	Ni	Pt	Si	W
$\Phi/\,(\mathrm{eV})$	4.1	5.4	4.6	5.6	5.2	5.7	4.8	4.8
$\kappa/\,(\mathrm{nm}^{-1})$	10.3	11.9	10.9	12.1	11.6	12.2	11.2	11.2

General Potential Barriers

The problem of the Schrődinger equation is that it can be analytically solved only for specific potential barriers. To describe the STM behavior more precisely, Wentzel-Kramer-Brilliouin (WKB) and Tersoff-Hamann approximation cen be used [7].

1.2.2 STM Modes

STM is able to measure in two different modes, constant height mode (CHM) and constant current mode (CCM) (Figure 1.6). Each of them has certain advantages and disadvantages.

a) CCM – Constant Current Mode
By using a feedback loop the tip is vertically adjusted so that the current always stays constant. As the current is proportional to the local density of states, the tip follows a contour of a constant density of states during scanning. A topographic image of the surface is generated by recording the vertical position of the tip in each point of the sample. The advantage of this method is that it is safer for the tip during scanning. On the other hand, the feedback loop can distort the image, and furthermore the scanning speed is relatively slow compared to CHM mode.

b) CHM – Constant Height Mode
Vertical position of the tip is not changed, feedback is disabled. The current is measured in each point of the sample and the image is formed by tunneling current and correlated with tip position. This mode is only appropriate for large atomically flat surfaces, otherwise a tip may destroyed. Advantages are that it can be used at high scanning frequencies (up to 10 kHz) and it has greater sensitivity for surfaces abnormalities because of disabled feedback loop.

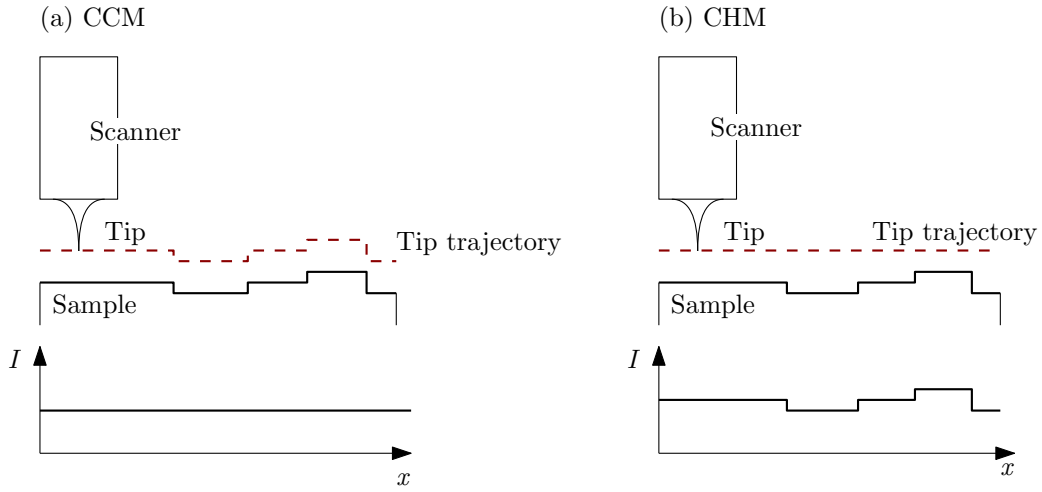

Figure 1.6: Comparison of (a) constant-height and (b) constant-current mode for STM.

1.3 Low Temperature STM

In modern age a lot of methods were developed for investigating structural or chemical information of the sample. One of the oldest method is called X-ray Diffraction [8]. Nevertheless, the most famous methods for surface study are Scanning Electron Microscope – SEM, Transmission Electron Microscope – TEM, Low-Energy Electron Diffraction – LEED, High-Energy Electron Diffraction – HEED, Atomic Force Microscopy – AFM and his varieties [5].

However, in the field of surface science techniques, STM and its varieties are still irreplaceable. Nowadays the most research studies are going with the Low Temperature STM (LT – STM), which enables similarly to STM, to display surface of material with atomic resolution in real time or even

go to subatomic resolution [7,12,13]. Thanks to the LT-STM, real time processes can be studied on the surface of the sample such as adhesion, collection of molecules, propagation of magnetic and electronic waves and more. With STM it is also possible to manipulate with atoms [15].

LT-STM is STM microscope working at temperatures less than 120 K [7]. To cool down the system the component cryostat which takes from the microscope the heat is part of the assembly. Typically, the cryostat uses as cooling element a liquid helium or liquid nitrogen to cool down the microscope. Thanks to low temperature, atomic movement is slowed down or completely stopped and therefore the new fields of surface study are opened.

One of the most used modification of LT-STM is the Scanning Tunneling Spectroscopy (STS) [16]. STS measures the energy dependence of the local density of states of the surface. During STS measurements the feedback loop is disabled and a bias voltage ramp to the tunneling junction. The tunneling current, as a function of bias, is the convolution of the tip LDOS and the sample LDOS.

Another used technique is called Spin polarized STM (SP-STM) [17]. By using ferromagnetic or anti-ferromagnetic tip, magnetic properties of the sample can be studied. The spin polarization of the tip electronic states plays a central role for generated tunneling current. The direction of the tip spin polarization is determined by two angle parameters. The degree of the tip spin polarization is characterized by a polarization parameter. All those parameters, including the direction and degree of spin polarization, often depend on energy level, or bias voltage.

Other uses of STM are shown in [7].

2 INSTRUMENTATION

Generally, STM microscopes are complex devices which require knowledge of several different branches of science, for example: common tunneling experiments, which include low temperature, surface science, vacuum physics, microscopy and vibration isolation technique (Figure 2.1) [7]. A typical STM microscope assembly consists of a microscope head where a sample, tip and positioning system is located, a chamber providing the required environment, a damping platform containing vibration damping, and electronics and in case of LT-STM the cryostat is included.

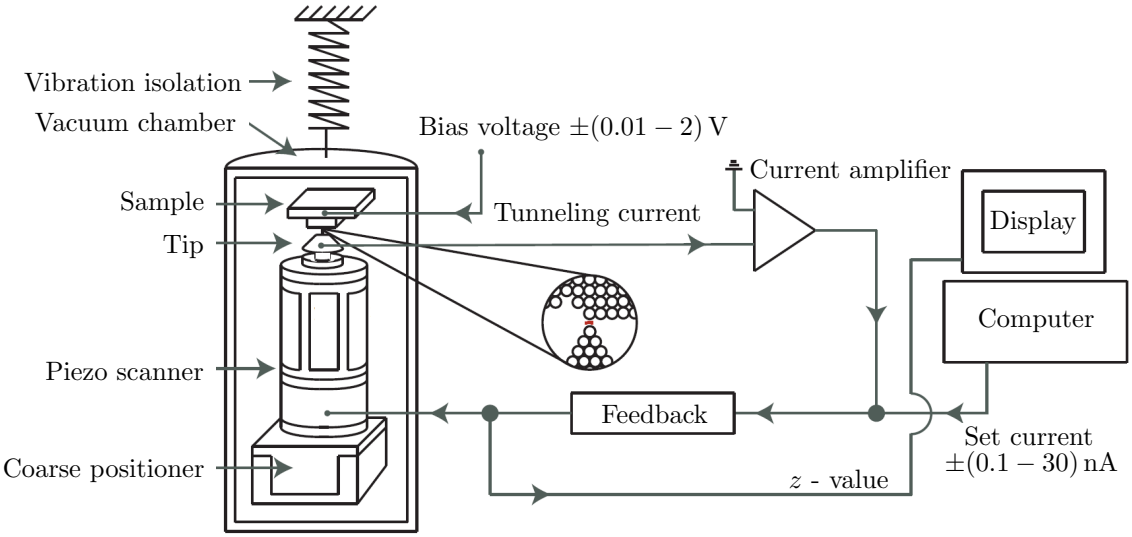

Figure 2.1: Scheme of the typical STM microscope. The microscope head is located in the chamber which hangs on vibration isolation. The tunneling current is amplified and the feedback loop adjusts the tip-sample distance to obtain a set value for current intensity. The feedback loop signal is imaged on the display as a topography of the sample.

To measure the tunneling current, the bias voltage has to be applied. Typical range of the bias voltage V_{bias} is between 1 mV to few V. The measured tunneling current is then in the range of 0.1 - 30 nA [7]. Such a current is too low to be measured, therefore the current amplifier has to be a part of the system. Moreover, the tunneling current exponentially depends on the thickness of the barrier (around several nm) and therefore the background vibrations can affect the STM measurement [4]. Stability of barrier is achieved by suspension the microscope on damping platform which uses different elements to limit the transmission of vibrations from the background to the microscope head.

Typically, the STM is equipped with two moving parts which provide the movement of the tip - scanner and coarse positioner. The scanner is mostly made of piezoelectric components (piezodrivers). Upon applying a voltage, the piezoelectric compoments expand or contract. This results in a high accuracy of movement in certain axis up to tenth of nanometers range. By applying a saw–tooth voltage on the x-piezodriver (x electrode of the piezoelectric scanner) and a ramp voltage on the y-piezodriver, the scanner moves in such way that the tip can raster–(scan) on the x-y plane of the sample. Because the range of scanners is in the micrometers range, a second moving component – coarse positioner is part of the microscope system. The coarse positioner is mainly used for approaching the tip to the sample or coarse movement in the plane of the sample.

The working range of coarse positioners is usually in millimeters range [7].

STM can be used in different pressures (typically 10^{-10} Pa – 10^{4} Pa), temperatures (typically 4 mK – 1000 K) [18], [19] and different environments (for example liquids or gases) [20], [21]. Based on these parameters, different phenomena can be observed. Nevertheless, the most widely used STMs are in Ultra High Vacuum (UHV) environment. Due to the UHV conditions, the contamination of the sample surface is reduced, and therefore the sample surface remains clean for longer period (several days) [22]. However, UHV environment brings more design restrictions, such as UHV compatible material have to be used.

2.1 Scanner and Coarse Positioner

The heart of every STM is the scanner. It is used to scan small areas of the sample with picometre precision. .

In basic, by applying the voltage on the piezoceramics, deformation is generated as showed in Figure 2.2. The direction of this deformation depends on Remnant polarization. This effect is called inverse piezoelectric effect and was predicted by Lippmann [24] and confirmed experimentally by Curie brothers in 19th century [25]. Another research revealed that the basic assumption of materials exhibiting piezoelectric properties depends on the asymmetry of their lattice structure [23]. However, the magnitude of the piezoelectric properties of natural crystals is relatively small, and therefore special materials have been developed, collectively referred to as piezoceramics. The most used piezoceramics are lead-based, zirconium and titanium-based material (PZT, lead-titanite) [23].

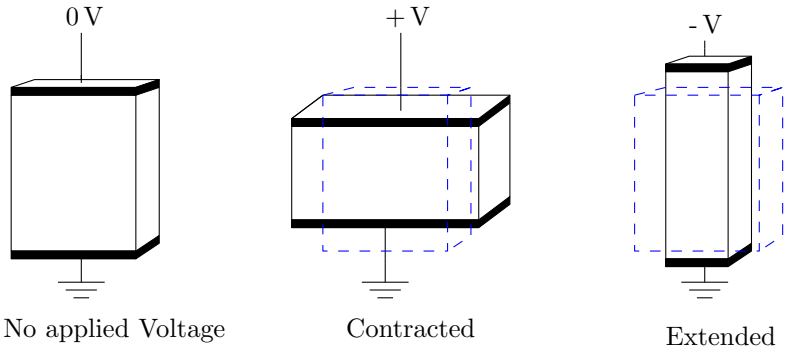

Figure 2.2: Schematic description of the generation of inverse piezoelectric effect by applied voltage.

Among many scanner types (tripod scanner, lever scanner and band scanner [23]), the tube scanner is very popular and in addition it is in systems which are described in this work. The tube scanner is popular mainly because of its high piezoelectric constant, high resonant frequency that allows it to achieve higher scanning speed, price, and low space consumption. On the other hand, because of the design of the tube scanner, the movements in one direction influence movements in other directions, and therefore must be compensated by special control.

The tube scanner is usually manufactured in two configurations (Figure 2.3). Both are made from a single piezoelectric ceramics, which is coated by six or five (depends on the type) metal electrodes. In configuration (b) by applying a voltage between all four outer electrodes, deformation in z axis is achieved. To generate deformation in x or y axis, a voltage has to be applied between two opposite electrodes. In this way one side expands and the other side contracts.

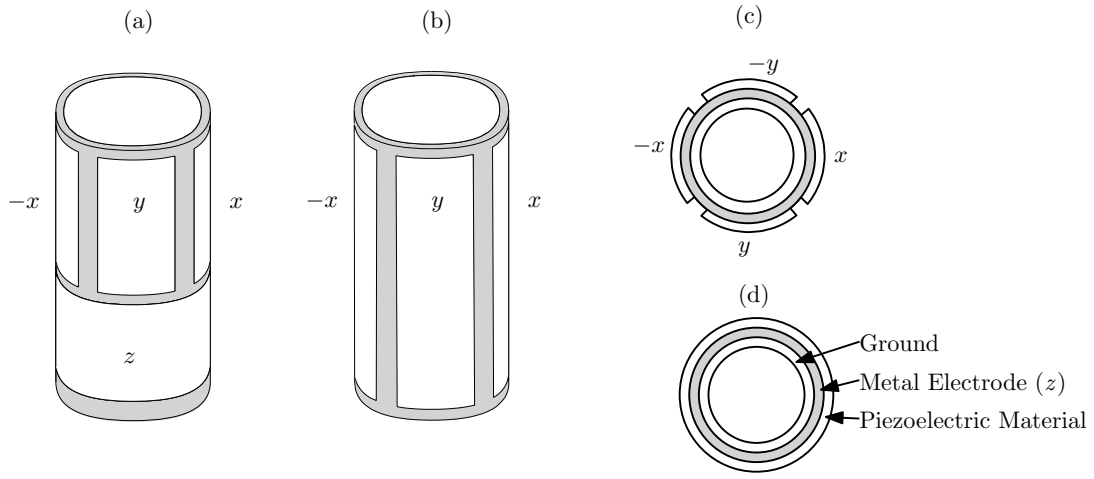

Figure 2.3: Schema of the two types of tube scanners (a) Tube scanner equipped with 6 electrodes. Two for x direction, two for y direction one for z direction, and one ground electrode inside the tube. (b) Tube scanner with 4 electrodes, two x direction and two for y direction. Deformation in the z direction is generated by applying voltage to all four electrodes. (c) Top view on both types of scanners, (d) bottom view at tube scanner with 6 electrodes

Coarse Positioner

The coarse system in STM is responsible for movement in the plane of the sample for long distances and together with a scanner to the safe approach of the tip to the sample at the distances of few nanometers (Figure 2.4). There are many types of coarse systems used in UHV. The most common so-called walker, kangaroo or the match [7]. The range of macro drivers is usually several millimeters. The description of the function of the walker positioner (coarse positioner used in our system coarse) together with the safe approach of the tip to the sample is shown in the Figure 2.4.

2.2 Vibration Isolation

At the beginning of STM, it was recognised that to achieve atomic resolution vibrations has to be suppressed [4]. The typical ridge-grove amplitude for STM atomic resolution image is about 10 pm (Figure 1.2 (b)). Therefore, the disturbance from external vibration must be reduced to one picometer or less. Today, there is no single way yet to isolate the microscope from vibrations in the entire frequency range. However, modern systems use multistage design with a several different damping components to minimalize the vibrations transfer.

The vibrations which degrade resolution of STM can be divided into low frequency vibrations ($<$ 100 Hz) and high frequency vibration ($>$ 100 Hz) [26]. The main source of low frequency vibrations are vibrations caused by walk (1 Hz - 3 Hz), vibration of building (10 Hz - 25 Hz), background noise and speech ($\approx$ 100 Hz) working machines (10-100 Hz) and electricity network ($\approx$50 Hz). By using damping systems such as rubber pads, suspending the microscope on damping springs, damping systems based on magnetic damping, low frequency noise can be minimized.

High frequencies are created mostly by mechanical vacuum pumps, cooling systems and the tools which are used around the microscope. The main way to eliminate high frequency of vibration is to use elastic components.

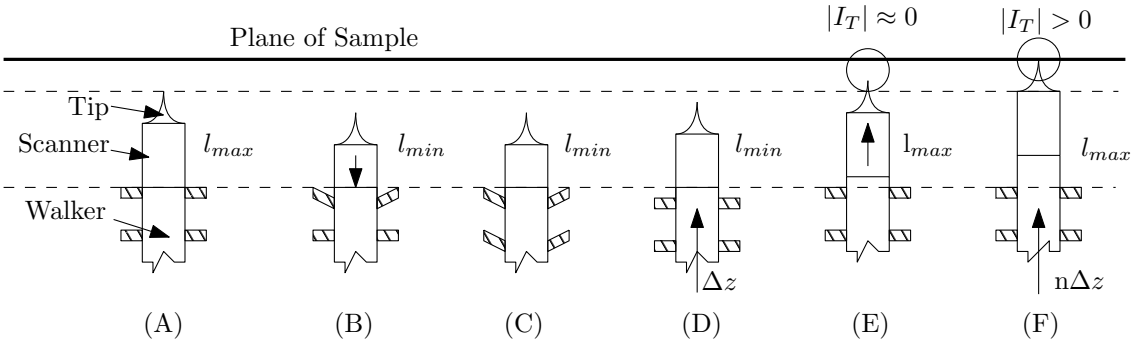

Figure 2.4: Scheme of approach of the tip to the sample using walker coarse system: (A) At the home position, the scanner is extended to maximum length, (B) the scanner is pulled down and two piezoelectric ceramics (piezo driver) of the walker positioner are bent while other two hold the scanner in fixed position. (C) The other two piezo drivers are bent down while the first two hold scanner fixed, (D) all four piezodrivers bend back with scanner. (E) The scanner is slowly extending to the maximal length and during the movement of the scanner toward the sample, the tunneling current is measured. If the measured current is zero in the maximum length of the scanner, (F) the first five cycles are repeated (A-E) until the tunneling current is established.

In most cases, damping systems are focused on frequencies from 1 Hz 1000 Hz [7]. These frequencies are transfered from the floor to the microscope. Frequencies lower than 1 Hz are not involved in to measurements because typically, the tip and the sample are placed into rigid body and oscillate with the same frequency and phase [5]. Vibration frequencies higher than 1000 Hz have only small amplitude, and therefore they do not affect measurement.

2.2.1 One-Stage System

Easy way to describe physics of vibration isolation in STM can be illustrated by vibrating system with one degree of freedom [27].

The vibrations from the ground and the air are always transmitted to the frame of the microscope. The vibrations transferred to the microscope are a type of forced oscillations. Source of vibrations oscillates with a fixed frequency ω which is transferred to the system. The simple model of damping system of STM is shown in Figure 2.5.

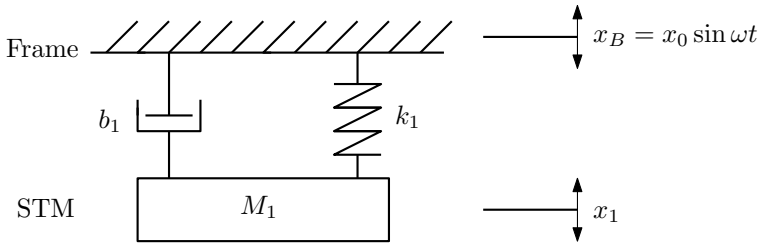

Figure 2.5: Scheme of the damping system. A mass M_1, which represents STM, is connected to the frame, which oscillate with deviation x_B through a spring k_1 and viscous element b_1. The frame represents the floor where the STM is placed.

The microscope head is represented by the mass M_1 which hang on the frame through the spring of the stiffness k_1. To make model simpler, the tip, sample holders and the base of the microscope are absolutely rigid body. Typically, for vibration isolation, the mass is mounted to the frame through a soft spring.

The restoring force of the spring action on the mass is

$$f = -k(x_1 - x_B) \tag{2.1}$$

In addition, for damping transferred vibration viscosity elements are used. A damping forces act between the frame and the mass,

$$f = -c(\dot{x}_1 - \dot{x}_B) \tag{2.2}$$

By introducing standard parameters, the natural frequency f_{01} of the mass M_1 and damping constant γ can be defined as

$$\omega_0 = 2\pi f_0 = \sqrt{\frac{k}{M_1}}, \tag{2.3}$$

$$\gamma = \frac{c}{2M_1}. \tag{2.4}$$

Model deviation for mass M_1 can be then described by Newton's equation [28]

$$M_1\ddot{x}_1 + b\dot{x}_1 + kx_1 = 0, \tag{2.5}$$

where x_1 is the deviation of the mass M_1, k is stiffness of the spring, b is coefficient of the viscous damping element.

Solution for the transfer ratio of one-stage system can be found in [29]

$$T_1(\omega) = \frac{x_B}{x_1} = \frac{\sqrt{\omega^4 + 4\gamma^2\omega^2}}{\sqrt{(\omega_0^2 - \omega^2)^2 + 4\gamma^2\omega^2}} \tag{2.6}$$

The examples of the transfer function for different damping values are in Figure 2.6.

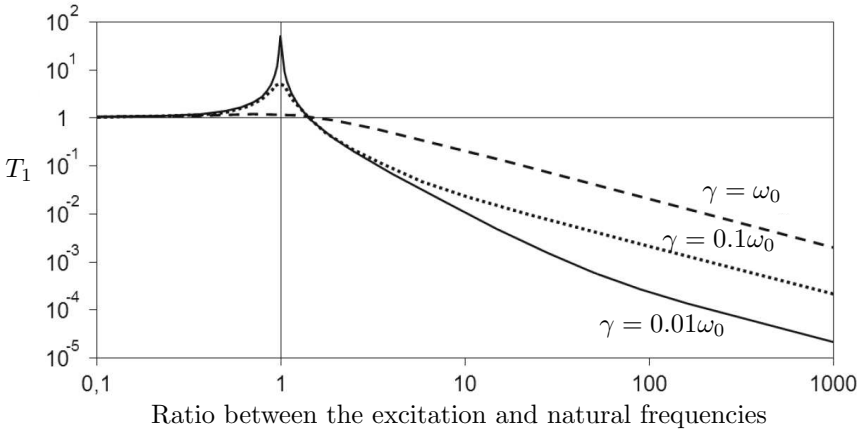

Figure 2.6: The example of the transfer function according to equation 2.6 for different damping values. Taken from [29].

2.2.2 Two-Stage System

In most cases for proper STM measurements more levels of sophisticated vibration systems are needed. For theoretical model that will be shown, vibration damping system uses a two-stage damping – spring and the magnetic damping (Figure 2.7). In reality, the pneumatic system is commonly used for second stage of damping. The following analysis is based on the study of Okano et al. [30].

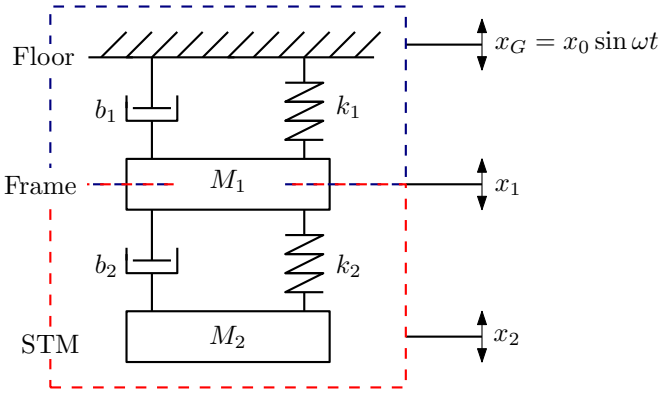

Figure 2.7: A two stage system for vibration isolation.

Two masses hang from the frame via two springs k_1 and k_2 and two damping elements b_1 and b_2 are present. The STM is represented by mass M_2, the frame by the M_1. For this system, Newton's equations for two masses M_1 and M_2 are

$$M_1\ddot{x}_1 + b_1\dot{x}_1 + b_2(\dot{x}_1 + \dot{x}_2 + k_2(x_1 - x_2) = b_1\dot{x} + k_1 x_G \tag{2.7}$$

$$M_2\ddot{x}_2 + c_2(\dot{x}_2 - \dot{x}_1) + k_2(x_2 - x_1) = 0. \tag{2.8}$$

Actual deviation of floor is

$$x_G(t) = X_0 \exp(\mathrm{i}\omega t). \tag{2.9}$$

To find solutions of the equations 2.7 and 2.8, the equations can be brought onto matrix form,

$$[A]x = x_G \tag{2.10}$$

$$[A] = \begin{bmatrix} k_1 + k_2 - M_1\omega^2 & -k_2 \\ -k_2 & a_{m,2} \quad k_2 - M_2\omega^2 \end{bmatrix} + \mathrm{i}\omega \begin{bmatrix} c_1 + c_2 & -c_2 \\ -c_2 & c_2 \end{bmatrix} \tag{2.11}$$

where

$$x = \begin{pmatrix} x_1 \\ x_2 \end{pmatrix} \qquad x_G = \begin{pmatrix} x_G \\ 0 \end{pmatrix}. \tag{2.12}$$

The transfer function, in units of decibels, is:

$$T = 20 \log_{10} \left| \frac{x_2}{x_G} \right| \tag{2.13}$$

Because obtaining an analytic solution for the transfer function of the matrix (2.13) is complicated, computer is used for displayed curves of a simulated system (Figure 2.8).

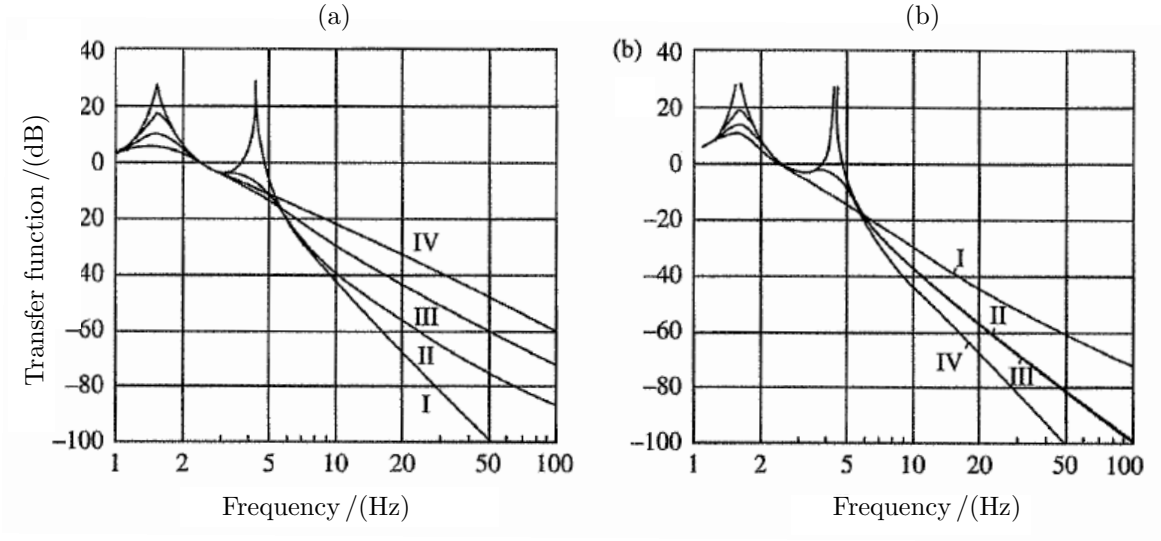

Figure 2.8: Curves of transfer function of two-stage vibration damping systems. Parameter used to calculate curves for both a) and b) M_1= 2.4 kg, M_2= 2.9 kg, k_1= 800 N/m, k_2 = 700 N/m. Separate values for a) damping stages are equal $c_1 = c_2 = c$. For I. $c = 0$ Ns/m, II. $c = 10$ Ns/m, III. $c = 20$ Ns/m and IV. $c = 50$ Ns/m. Separate values of damping for b) I. $c_1 = c_2 = c = 20$ Ns/m, II. $c_1 = 20$ Ns/m and $c_2 = 0$ Ns/m, III. $c = 0$ Ns/m and $c = 20$ Ns/m IV. $c_1 = c_2 = 0$ Ns/m. Taken from [7].

Generally, the two-stage system for vibration damping is much more effective than the one-stage system. For both systems, when viscous damping is removed, the vibration isolation is optimized for higher frequency (Figure 2.8 (a), curve I). As it can be seen in model, to suppress the resonance it is possible to introduce various numbers of viscous elements (for example Figure 2.8 (a), curve II). Moreover, it can be seen that one viscous damping element (Figure 2.8 (b), curve II) is sufficient to suppress the resonance frequencies.

2.2.3 Vibration of Microscope Head

From the perspective of STM microscope the most critical movement is movement of the tip toward to the sample (Figure 2.9). The situation is similar to the one-stage system (Figure 2.5).

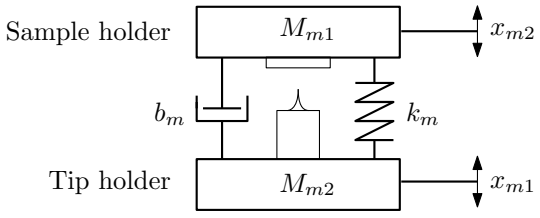

Figure 2.9: Scheme of the vibrating system. A mass M_{m1}, which represents sample holder is connected to the mass M_{m2}, which represents scanner tip holder, through a spring k_m. The vibrations are damped by the viscous element b_m.

The transfer rate of microscope head is described as a ratio of the relative tip-sample distance and the amplitude of the tip holder vibration. For the relative distance x_r of sample-tip is equal

$$x_r = x_{m1} - x_{m2}. \tag{2.14}$$

Then the transfer function is equal to

$$T_2 = \frac{x_{m1} - x_{m2}}{x_{m2}} = \frac{x_r}{x_{m2}}. \tag{2.15}$$

Solution for transfer ratio of microscope head can be found in [29]:

$$T_2(\omega) = \frac{\omega_{m2}^2}{\sqrt{(\omega_{0m1}^2 - \omega_{m2}^2)^2 + 4\gamma_{m2}^2\omega_{m2}^2}}. \tag{2.16}$$

The transfer function $T_2(\omega)$ 2.16 is shown in the Figure 2.10. The character is opposite in comparison to the transfer function for the one-stage system. The maximal of the function occurs, when the initiative frequency is equal to natural frequency of the system, but for the frequency lower than own frequency the transfer function is closed to one. For the frequency higher than own frequency the function has a decreasing character which is dependent on the damping system.

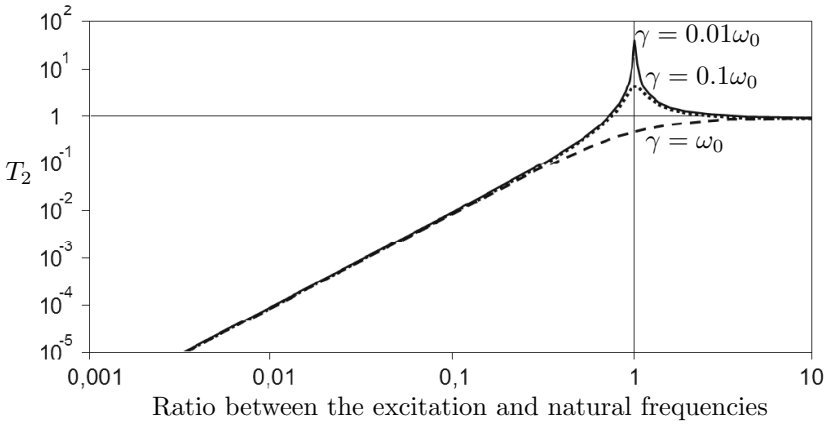

Figure 2.10: The example of the transfer function according to equation 2.16 for different damping values. Taken from [29].

2.2.4 Vibration immunity of STM

In most cases, two levels of damping vibrations are used for construction of STM (Figure 2.11). Nowadays STMs are build with design where the tip and the sample are placed in solid body, called microscope head (Figure 2.11). It is the easiest way to isolate the system from low frequency vibrations ($\sim$ 0-100 Hz). By choosing closed design of STM measure head with mass M, the excitation frequency is much lower than the natural frequency of the microscope head, then the assembly moves closely with the frame and low-frequency vibrations do not affect the measuring processes in the head. To make the microscope head sufficiently rigid, it is required to have the mechanic loop [1] as short as possible [90].

[1] Mechanic loop is the shortest way from the sample to the tip.

Isolation of high frequency vibrations ($\sim$ 100-10000) Hz is realized by soft connection between microscope head and the ground. Damping elements can be also used for high frequency damping, for example by hanging the microscope head on the soft spring or adding magnetic damping systems to the system. Because the spring changes the resonant frequency to higher value compared to original value, less frequencies are transferred to the system, which are then damped by the viscous element.

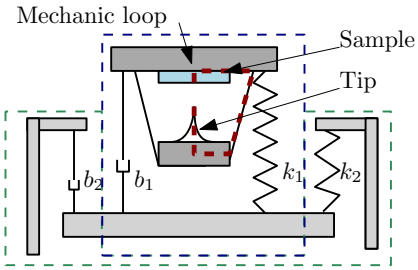

Figure 2.11: Scheme of two stage damping system with closed microscope head. The mechanic loop represented the shortest way from the tip to the sample.

Real systems are more complex and they have a huge number of own frequencies. For this reason exact calculations of transfer function are almost impossible, and thus the numerical simulations are done in computer programs for example [31].

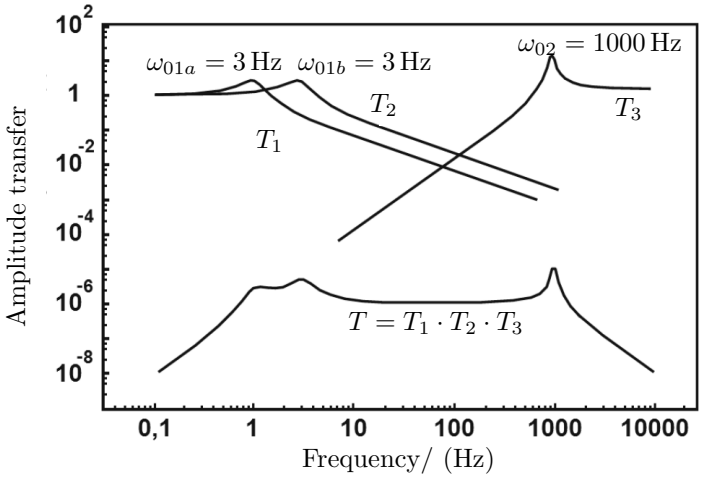

Figure 2.12: The example of the two stage damping isolation system (Figure 2.11). T_1 and T_2 represent transfer function of two-stage system with natural frequency $\omega_0 = 1$ Hz and $\omega_0 = 2$ Hz. T_3 represents transfer function of rigid microscope head with natural frequency $\omega_0 = 1000$ Hz. Total transmission function of the system is given by their multiplication. From experiments, the value of transmission function 10^{-6} is sufficient to reach an atomic resolution with STM.

In summary, the most critical point in vibration transfer are bonds between source of vibration and the object. The resulting transfer function T is given by multiplication of the individual transfer functions T_1, T_2 and T_3. Corresponding to previous solution of two-stage system Figure (2.8) and microscope head system (Figure 2.10). Transfer function T expresses the ratio of relative

tip-sample distance and vibration amplitude for different initial frequencies. The transfer funtion in the range of 10^{-6} is sufficient to achieve atomic resolution.

2.2.5 Vibration Damping Options

Vibration dampers can be divided into two groups - passive and active damping. Generally, active damping systems are composed of the active drive that responds to relative movements of pendulums. These movement forces are typically controlled by computer and created by manipulators. They are usually part of pneumatic damping systems or independent piezoelectric drivers. The biggest advantage is the efficient damping of a large range of vibration frequencies. On the other hand, the price of such devices is several times higher than passive damping system.

To sum up previous topic, the main goal of damping platform is to avoid transfer of the vibrations to the head of the microscope. If some vibrations are transmitted, the system has to be equipped with an efficient system to reduce them. Most of the systems working in the air conditions are strongly damped thanks to the surrounding air. In UHV conditions density of residual particles in chamber is so small that their resistance is negligible. Other ways to damp the vibration in UHV conditions have to be used.

The passive damping only acts in dependence on the relative movement of the pendulum to the damper. Examples are pendulum in air conditions, where the resistance force of the air acts against movement of pendulum. The advantages are low price and simplicity. In UHV conditions, the most common passive damping use magnetic damping. By moving magnet against metal elements the eddy currents are generated in conductive materials. Eddy currents creates a magnetic field acting against the magnet's motion [5].

2.3 Tip Preparation

The technology of the STM is based on the tunneling effect which occurs between the tip and the sample. The importance of the tip treatment, which strongly influences the STM resolution, was recognized by Binnig and Rohrer from the beginning of their experimentation. To achieve atomic resolution by STM measurements, typically tips have only one atom at the end, which provides or gather electrons from the sample [32].

The most common method for fabrication STM tips is cut-off method and eletrochemical etching. More advanced methods for fabrication are sharpening by focused ion beam (FIB), controlled crashing, emission/evaporation or ion milling [7]. Among commonly used materials for fabrication of the STM tips are metal wires like tungsten (W), platinum-iridium (Pt-Ir) or gold (Au) for their small work function.

2.3.1 Cut-off Method

This method is very similar to mechanically grinding down a wire until reaching a very sharp tip, however in this case instead of using a grinder we are using a fine wire cutters and we are taking advantage of the ductility of the material. The most common material used in this method is platinum-iridium (Pt-Ir) [33]. Upon applying the right force to a cut, tips with one atom at the end can be produced.

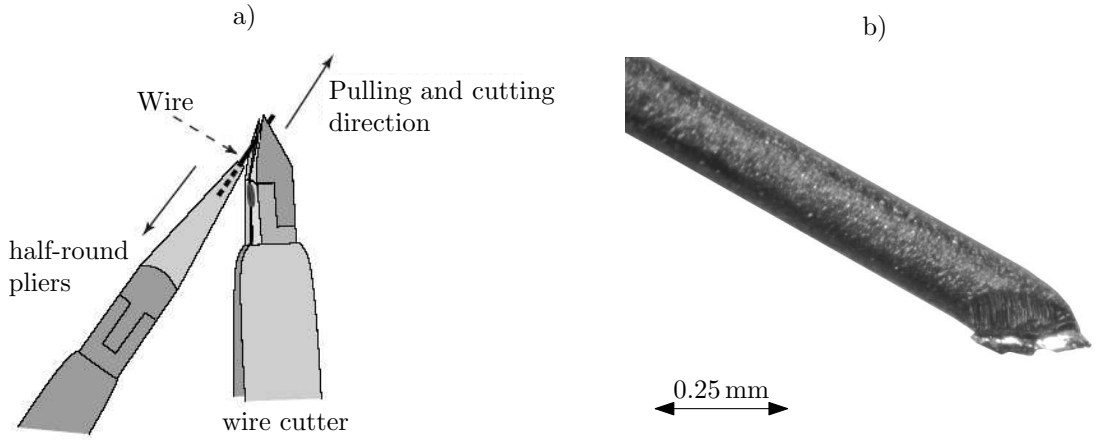

Figure 2.13: (a) Scheme of fabrication of the tip by cut-off method. Taken from [33]. (b) The picture of the tip fabricated by cut-off method.

2.3.2 Electrochemical Tip Etching

Electrochemical tip etching is one of the most used method for tip preparation [53]. Mainly for the good quality sharp tips which can be produced. The method was developed in 1950s for preparing samples for Field Ion Microscopes [7].

For common materials like tungsten (W), Cobalt (Co), Chromium (Cr), Gold (Au) the principle of electrochemical etching is simple [35], [34]. Part of wire is immersed into electrolyte together with electrode. By applying voltage the current is generated and the wire starts to be etched. After a while, the wire in the area of the meniscus (the area of contact wire and surface of electrolyte) is etched more than the surrounding parts of the wire. After certain time, the thickness of the wire in the meniscus area is so small that it can not hold the weight of bottom part of wire. By tension the wire mechanically breaks off and bottom part falls down. For bottom part the electrical contact is lost and etching is stopped. For top part the etching is stopped by control unit, but only few milliseconds of etching are enough to make top part rounded.

After the bottom part is detached, in order to achieve high sharpness of the top part of wire two controls are used to stop the etching.

- Threshold method measures the current of etching. When the value falls down under the set value, the etching is stopped. The problem of the method is to find the threshold value. Hence, numerous experiments have to be done for each material and each diameter of wires.
- Differential method measures the change of the measured current in time. By setting a value of sensitivity to current change, the controller can stop etching when the current drops too fast.

2.3.3 Ex Situ Tip Treatments

The tips from tungsten, chromium, cobalt and other materials are after electrochemical etching covered with thin layer of oxide and often contaminated with sodium compounds from electrolyte as well as organic molecules. Therefore, procedures to remove oxides and other various contaminants must be executed before the tip is inserted into the STM. The contamination of the surface can prevent conductivity and therefore the tunneling current.

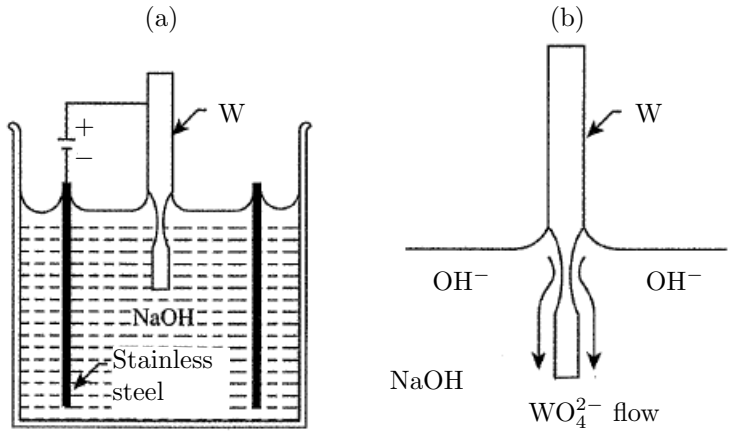

Figure 2.14: (a) Scheme of electro-chemical etching of tungsten wire in NaOH electrolyte. As a counter cathode a stainless steal electrode is used. (b) Detail of the etching process. Taken from [7].

The most common ex situ tip treatment method is annealing. The tip in the vacuum is annealed to a temperature higher than 1000 °C to remove the contaminants and oxides. For the tip with low melting point, methods like field evaporation, controlled deposition, atomic metallic ion emission can be used [7].

3 CONSTRUCTION IN UHV CONDITIONS

This chapter deals with the description of construction condition for low temperature systems in UltraHigh Vacuum (UHV).

UHV is the vacuum regime characterized by pressures lower than 10^{-7} pascal or 100 nanopascals (10^{-9} mbar, 10^{-9} torr). The mean free path of gas molecules in the UHV conditions is approximately 40 km. That means that gas molecules will collide with chamber walls many times before colliding with each other. This is very useful for surface studies. By low density of gas particle in the chamber the time to cover the sample surface with one mono-layer of gas molecules takes several days.

In general terms, UHV conditions are created by pumping the gas out of the UHV chamber with multi-pumping level system [22]. In the first level, the mechanical pumps such as rotary pumps or scroll pumps are used. In the second level, the turbomolecular pumps decrease the preassure to high vacuum (10^{-3} Pa – 10^{-7} Pa). To drain the chamber to the ultra vacuum level, the chamber has to be baked and then the third level of pumping done by ion pumps. There are also other options to achieve UHV pressures. These options are discussed in more details in [22, 36, 37].

However, using the multi-stage pumping is not enough and other conditions play an important role in achieving the required level of vacuum. First of the conditions is the right choice of materials and properly cleaning all the components before inserting them into the vacuum chamber. Then, there are general rules of mechanical design which shorten the pumping time[1].

3.1 Selection of Material for a UHV Environment

In general, the required properties of UHV-compatible materials are: thermal and mechanical stability, electrical and thermal conductivity, low vegetation and a small amount of micro cracks. By avoiding low amount of micro cracks and low vegetation of material better pumping time is achieved.

3.1.1 Low Desorption of Gases

If the material contains a large amount of gas in bulk or molecules on the surface, the molecules will be released. Therefore, the pumping time and the possible lowest pressure will increase. Assuming a perfectly tight chamber, the pressure in the chamber can be described using the equation

$$p = \frac{QA}{S}, \tag{3.1}$$

where S is the pumping speed, A is the total surface are in the chamber and Q is the coeficient of desorption [22]. The pressure in the vacuum chamber depends on the amount of particles, which escape from the surface or the bulk. For this reason, there are certain materials which are suitable for vacuum conditions and some materials that are not suitable. The biggest group of materials suitable for use in the vacuum are metals, especially different types of stainless steel [38]. The biggest advantages of these materials are the mechanical stability and relative reasonable price. Another suitable representative of metals is tungsten, tantalum and molybdenum for their high melting temperature. For components, where the high thermal and electrical conductivity is required, oxygen-free copper is mainly used.

[1] Pumping time is the time that is needed to pump the chamber to the lowest pressure value which is achievable by the pumping system

For some parts the non-electrically conducting materials, or materials with a certain thermal conductivity are required. In these cases, mainly polymers or ceramic materials are used. For example for electric isolation it is common to use Kapton [39]. As an electrical insulator with, mainly materials like machinable glass ceramic (Macor) [40] and Polyether Ether Ketone (PEEK) are used [41]. Both materials are able to be machined by conventional methods used for metals in compare to ceramics.

To achieve the UHV conditions, the amount of water in the chamber plays an important role. In air conditions, water forms a thin layer on the surface of all materials. In vacuum conditions, the water starts to evaporate and appears as a source of particles, which prevents to reach desired conditions. To remove the water from the chamber, the chamber has to be baked to a temperature above 100 °C for several days. Water receives energy in the form of heat, desorbe from the surface of the matrix and is more easily pumped out, in comparison with to spontaneous gradual release.

Table 3.1 shows basic materials compatible with UHV conditions such as metals, polymers, ceramics and others.

Table 3.1: Selected materials suitable for use in the UHV.

Metal	Stainless Steel, Copper, Aluminum, Titan, Tungsten, Tantalum, Molybdenum, Gold
Polymers	Kapton, Viton, PEEK, Teflon
Ceramics	Macor, Alumina
Others	Glass, Sapphire, Silica

3.1.2 General Rules to Design in UHV

Besides the right choice of material, certain design principles for the proposed devices are also to be used for UHV condition.

Virtual leakage

In addition to releasing gas directly from the material or by desorbing particles from the vacuum vacuum walls, the gas can escape gradually from closed cavities (Figure 3.1). This results in increased pumping time, or decrease in available pressure, which is the same as leakage of the vacuum system. Therefore, it is necessary to avoid ungrounded space in the design of the device, among which the blind bolt holes are the most common. If a through-hole is not possible to construct, hollow screws with a through hole along the axis or a partially threaded thread are used.

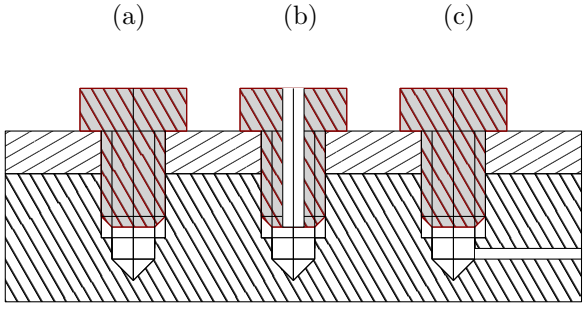

Figure 3.1: Schema of possibilities to avoid the closed cavities in left (a), (b) drilling a hole along the screw axis, (c) drilling the cavity from side. Taken from [23].

Heat transfer

The heat transfer by flow is practically negligible in the low pressure under UHV conditions. However, this is a major problem when parts of the device operating in a vacuum need to be cooled down. Difficulties also include the heat of the electric conductors themselves, which dissipate part of the transmitted power due to the resistance. Possible melting of the insulation may lead to an increase in the desorption of the insulating material or interruption of the conductor by electric cut.

In the case of devices at variable temperature, the different thermal expansions of different materials must also be taken into account. Vertical or shape joints may become loose due to temperature changes.

Cleanliness of parts

In compliance with UHV, parts must also be properly clean before use. Particular attention should be paid to removal of residual oil and lubricants (eg after machining) which have low saturation vapour pressure and can increase pump time. Various materials are cleaned differently and the appropriate procedure should be chosen.

For all materials, due to gas adsorption and desorption is important the surface quality of the vacuum components. Surfaces should be smooth, free of pores and cracks. For processing and achieving the required surface quality, sanding, shaving, mechanical or electrochemical polishing is used.

4 PREPARATION OF SUPERCONDUCTING-MAGNETIC INTERFACES

In recent years, the research in the field of monolayer systems have become very popular. In particular magnetism at the nanoscale [43], [44], [45] and preserving the superconductivity in superconducting materials when reaching the ultra thin film limit [46], [47] was topic of high interest. When these two phenomena are put into one system, a relatively new and interesting field might be opened. By bringing a conventional superconductor into the system in the presence different state of matter, a topological superconductor, can be created. On the edge of such a topological superconductor, Majorana Femions are predicted to confine [48].

This chapter presents my work in the SPM group of Alexander Ako Khajetoorians in Nijmegen. My work was a part of a long running research project. The goal of the project was to investigate superconducting-magnetic interface by SP-STM. The desired system of superconducting-magnetic interface is described in Figure 4.1.

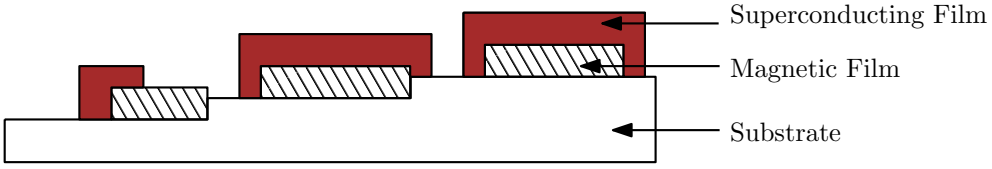

Figure 4.1: Schematic drawing of the required superconducting-magnetic interface system.

The project can be divided into five preparative parts:

1. Preparing of tips for SP-STM.
2. Preparing of atomically flat and clean substrate surface.
3. Controlling of growth of a magnetic film on the substrate without losing the magnetic properties.
4. Controlling of the growth of a superconducting material on the substrate while preserving the superconducting properties.
5. Controlling the growth of the films on top of each other.

The project is still in progress, my role in this project was the preparation and testing of chromium tips and then follow up the work on the project of Ing. Aleš Cahlík on the first parts of this project [49], the grow study of the superconducting materials such as vanadium, tantalum or niobium on substrate.

4.1 LT-Omicron Experimental Set-up

The LT-STM microscope, used for the most of the work described in this chapter belongs to the first generation of Omicron low temperature microscopes (Figure 4.2) [50] and was improved by the SPM group [49].

The Omicron system consists of three main parts: the Load-Lock chamber, the Preparation chamber and the LT-STM chamber. The chambers are separated from each other by gate valves. Because of this, the pressure in the chambers are independent and can be separately modified.

Load-Lock Chamber

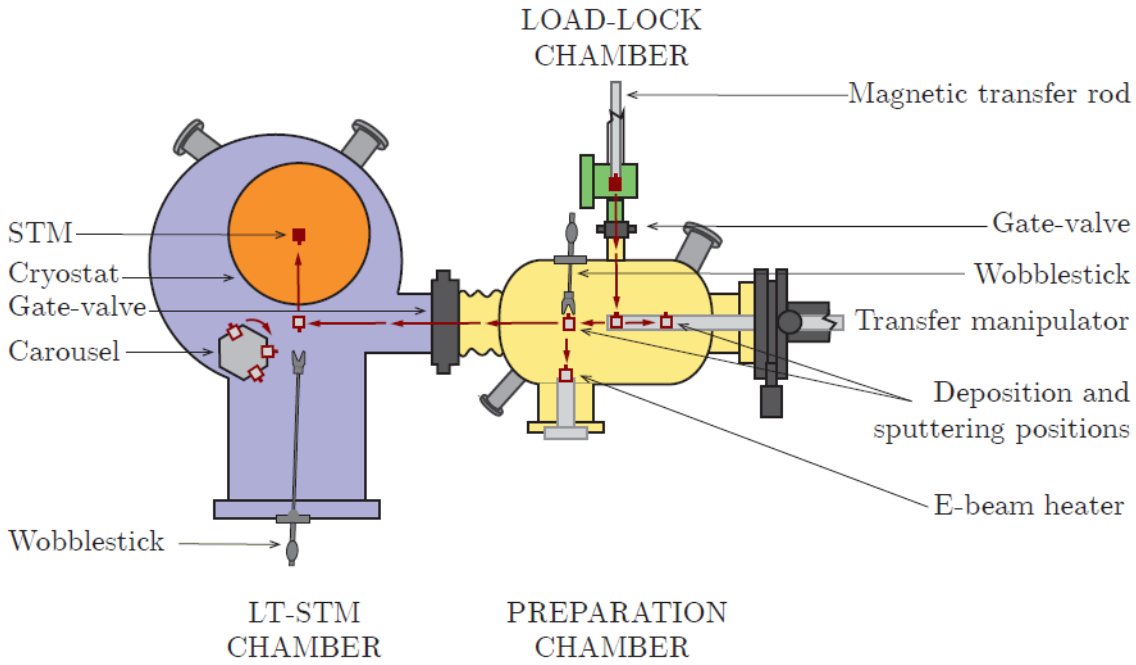

Figure 4.2: Schematic drawing of the experimental set-up of the Omicron UHV LT-STM and the sample transfer line (placed in city Nijmegen). Load-Lock chamber – green. Preparation chamber – yellow. LT-STM chamber – blue. Taken from [49].

The Load-Lock chamber mainly serves for insertion of the samples into the system. Due to the small volume of the chamber the chamber is pumped in short time and the contamination by the residual gas of other chambers is almost negligible. The Load-Lock chamber is pumped by a separate system that comprises the turbo with the scroll pump. In normal operation mode, the pressure in the chamber after 30 min of pumping is reduced to 10^{-3} Pa which is sufficient pressure for moving the sample into the preparation chamber. For the transfer of the sample to the preparation chamber the magnetic transfer rod is used.

Preparation chamber

The preparation chamber is employed for cleaning and preparation of samples. The chamber is equipped with an e-beam heater that can heat up samples to more than 1000 °C. A sputtering gun for removing top layers of the samples by Ar^+ or Ne^+ ions and a deposition system with variable options of materials are also present. Moreover, in the chamber there are additional flanges at which optional devices can be mounted.

The sample from the Load-Lock chamber is inserted into the transport manipulator by the magnetic transfer rod. It can move in a chamber in four axes (x, y, z, and rotate around the manipulator z axis) and it is capable of transporting the sample to the LT-STM chamber. In addition, the manipulator is equipped with a resistive heating system which can heat up the sample to a temperature 400 °C.

The sample in the manipulator can be also cooled down by cooling element (liquid nitrogen, helium, and other). The temperature is measured by a thermocouple which is located in the vicinity of the sample. Another device capable of manipulating samples located in the Preparation chamber is called a wobble stick. The wobble stick is a magnetic transfer arm with tweezers at the

end. It gives a possibility of precise movement with the sample and it is mainly used to transport the specimen from the transfer manipulator to the e-beam heater.

The pumping system of the Preparation chamber consists of ion pumps, turbo pumps, and titanium sublimation pump, so that the chamber is continuously pumped even during STM measurements at 10^{-9} Pa.

LT-STM chamber

The main science activity takes place in the LT-STM chamber, where LT-STM is located. The microscope uses a suspension system in order to suppress vibrations.

The low temperature microscope is cooled through two stationary cryostats – outer and inner. To achieve the lowest temperature, the microscope is equipped with two radiation shields. The steady sample temperatures are for liquid nitrogen around 77 K and for liquid helium 4.4 K.

The sample is moved from the preparation chamber to LT-STM chamber via a transfer manipulator. Into the microscope head (part of the Omicron STM, where the tip, scanner and sample are placed), the sample is inserted by using the second wobble stick, which is located in the LT-STM chamber. For storing up to 6 samples a carousel is used and is located in the LT-chamber next to the microscope.

The vacuum is maintained in the LT-STM chamber similarly to the Preparation chamber. The LT-STM chamber is pumped individually with an ion and sublimation pump. In addition, when microscope is cooled down, it behaves like a cryo pump and the pressure in range of 10^{-10} Pa can be reached in the chamber.

4.2 Fabrication of SP-STM Tips

The Spin Polarized Scanning Tunneling Microscope (SP-STM) is a variation of the classical UHV-STM. The microscope has the same spatial resolution as STM, but it is more sensitive to the spin orientation of tunneling electrons. The main technical difference between STM and SP-STM is in the material which the STM tip is made. SP-STM tip is made of a material with a well-defined spin-polarization such as ferromagnetic or anti-ferromagnetic materials [17]. If the magnetic tip is inserted into the STM without the external magnetic field, the spin of the last atom that is responsible for the tunneling current can be changed during the measurement. Therefore, it is not clear what is its orientation and to which direction it is sensitive. That is the reason why magnets are typically mounted around the tip, and thus ensuring the orientation of the spin on the tip and sample during measurement.

There are several possibilities to create a tip for SP-STM. One of the first options is to cover the non-magnetic tip with the magnetic material. Another possibility is to dip the tip into the magnetic material and create a cluster of magnetic material at the apex of the tip. The third and the most commonly used option is to prepare the bulk magnetic tip by chemical etching.

Each of the techniques outlined in Figure 4.4 has its advantages and disadvantages which are mentioned in [17]. However, the best sensitivity for measuring and fabrication re-production is provided by etching of the bulk magnetic tip. Typical materials for fabrication ferromagnetic tips are Cobalt, Iron or Nickel and for anti-ferromagnetic are Chromium and Manganese.

The difference between ferromagnetic and anti-ferromagnetic tips is the range of the sensitivity and influence on the sample by its own magnetic field [53], [52]. As compared to the anti-ferromagnetic tips, the ferromagnetic tips have a higher sensitivity, but on the other hand, its magnetic field affects the magnetic properties of sample during the measurement.

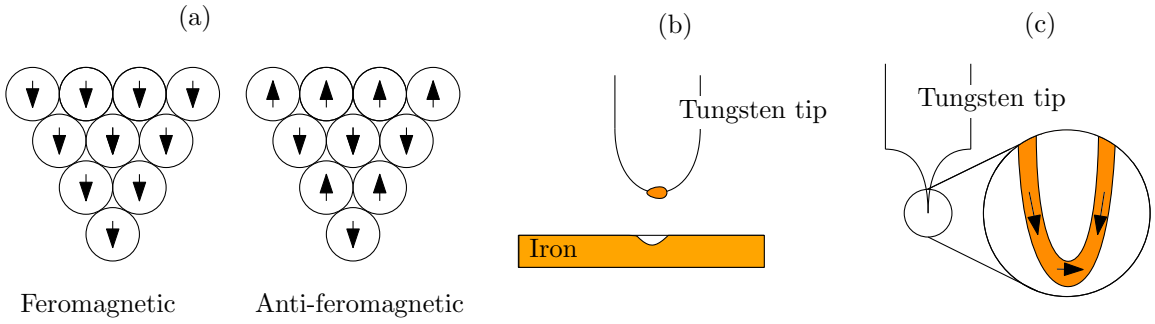

Figure 4.3: Schematically illustrated three types of tip for SP-STM: a) structure of bulk magnetic-material tip (mostly using electro-chemical etching), b) illustration of a magnet tip produced by dipping tip into a magnetic material, and c) illustration of magnetic tip which was fabricated by deposition magnetic material at the end of the tip.

For our project, material for the production of anti-ferromagnetic tips was represented by chromium. Tips were chosen in accordance with procedure mentioned in [51], [52] for chromium tips.

Etching Station

The Omicron etching station consists of an etching controller (Figure is not present here) and a handling device that ensures precise insertion of the tip together with the electrode into the Petri dish (Figure 4.4) [55].

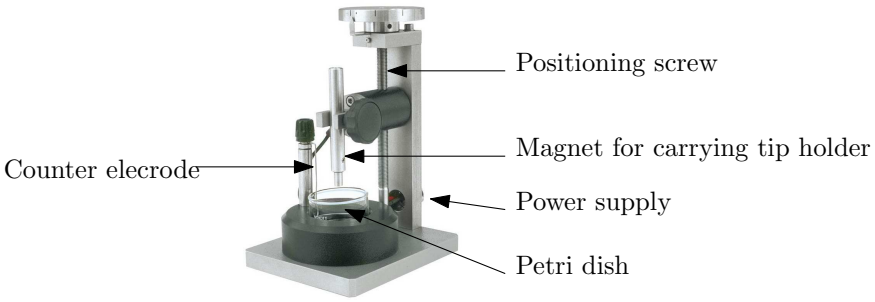

Figure 4.4: Picture of the handling device together with labels of functional parts.

The etching controller allows to adjust the voltage and measures the current between the electrode and the tip. Moreover, the controller has two cut-off options during etching with adjustable parameters to achieve sharp tips, which were discussed in the chapter 2.

4.2.1 Chromium Tips

The purity factor of etched chromium wire was ensured at least 3 N (i.e. 99.9 % of Chromium in the wire). The etching of the chromium tips was done in configuration where most of the bottom part of the etched wire (which is immersed in the electrolyte) was covered by a nail polish. Thanks to the nail polish, most of the bottom part of the wire immersed in the electrolyte is protected from etching. The etching occurs only in the small area of wire in electrolyte, which is not covered

by nail polish. As a result, after the disconnection of the lower part of the wire, the bottom part can be caught from the bottom of the Petri dish. This way allows to produce two tips in one procedure.

The NaOH solution was used as the electrolyte for chromium tip etching, and as the electrode material was used stainless steel. Circuit voltage during etching process was 4 V (Configuration is similar to the figure 2.14). The equation of etching process which takes place on anode is:

$$\mathrm{Cr} + 8\mathrm{OH}^- \rightarrow \mathrm{CrO}_4^{2-} + 4\mathrm{H_2O} + 6\mathrm{e}^- \tag{4.1}$$

The results of bottom and top part from the etching can be found in Figure 4.5. Detailed views of the end of the tip of both parts are shown in Figure 4.6. The pictures were taken by confocal microscope [56].

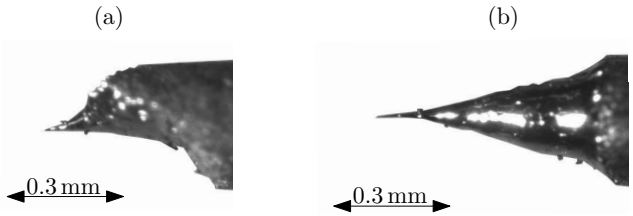

Figure 4.5: Two parts of chromium wire, (a) bottom part which fell to the bottom of petri dish, (b) top part which was stopped after the etching in the tip holder. Voltage of 4 V was used.

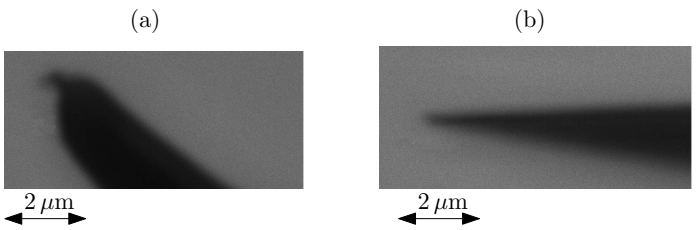

Figure 4.6: The detail of apex of the tips from Figure 4.5. (a) The bottom part of the wire, (b) The top part of the wire.

After the etching process, the tip was rinsed in acetone and ethanol to remove the nail polish which covered the bottom part of the wire and to desorb the organic compounds from the tip surface. In the vacuum, the tips were annealed to remove oxide layers from the surface.

4.3 Testing of SP-STM

Chromium tips were then tested on the Fe-Ir system (111). This system is characterized by the fact that the magnetic structures of the skyrmion lattice can be observed by measurements in the correct configuration (temperature under 20 K and using SP-STM tips) [59]. In addition, the system Fe-Ir(111) is also suitable to the overall project (for layers magnetic film and substrate in Figure 4.1).

All 2-D images were crated by FFT, which used convention $k = 1/\lambda$ in software WXSM [60].

4.3.1 Preparation of Substrate – Ir(111)

All measurements in this chapter are performed using a tungsten tip at temperatures of 77,K. Unless test of chromium tips on system Fe-Ir(111) (Figure 4.9).

The main reason for selection iridium as a substrate was the good knowledge of the systems from large amount publications dealing with the study of the surfaces at the atomic level [58].

Iridium belongs to the Group VIII transition metals, which play a vital role in many important industrial catalytic reactions. Iridium crystal has the fcc structures with a lattice constant $a = 2.84\,\text{Å}$ [57]. The calculated distance between the closest atoms in plane (111) is $b = 2.34\,\text{Å}$. A common procedure for cleaning the irridium crystal surface according to [58] is composed of three steps. In the first step, dynamic Ar^+ or Ne^+ sputtering of the sample surface is done. As a result, the contaminated top layers of Iridium crystal are removed.

In the second step of the cleaning procedure, the sample is annealed in partial oxygen pressure. During this annealing, carbon diffuses from the volume of the crystal to the surface where it reacts with O and forms CO and CO_2. These molecules desorb from the surface and are pumped out of the chamber. Due to the high temperature of annealing (below the melting point of the iridium), the atoms on the surface receive enough energy to overcome the diffusion barrier and travel to the surface, thereby re-aligning the surface after the bombardment. However, oxygen is still adsorbed to the surface. To remove the residual oxygen on the surface, the third step of the cleaning procedure is needed. In the third step the sample is heated to a temperature of about $1500\,°\text{C}$. This ensures the desorption of oxide and ions from the sputtering procedure from the sample surface. The high temperature also gives to the atoms sufficient energy to migrate on the surface and smoothen the surface. Parameters used in the three cleaning steps for achieving atomically clean surface are given in the table 4.1.

Table 4.1: Summary of Ir(111) surface cleaning procedure.

Procedure	Time/ (min)	Temp/ (°C)	Pressure/(mbar)s
O_2 anneal.	15	-	Oxygen $2 \cdot 10^{-7}$
Ar^+ ion sputtering	15	1300	Argon $5 \cdot 10^{-6}$
Flash	2	1500	$< 1 \cdot 10^{-9}$

After the cleaning process was done, in Figure 4.7 (a) is Show a clear surface of the iridium after application of the cleaning process. The image in the Figure 4.7 (b) shows an atomic resolution image. The inset shows the 2D Fourier transformation ($k = 1/\lambda$ convention) of the atomic structure. From the FFT reciprocal space, the average distance between the closest atoms (marked by the green line) was determined as $b = (2.44 \pm 0.27)\,\text{Å}$. This also agrees with the theoretical calculated value for the Ir(111) plane $b = 2.34\,\text{Å}$. The blue circles marks missing atoms in the surface plane. To sum up, we succeeded in preparing of the cleaning procedure of Ir(111). This was confirmed by reaching atomic resolution on the Ir(111) plane with correct dimensions.

4.3.2 Growth of a Magnetic Film on the Substrate – System Fe-Ir(111)

As mentioned above, the reason why iron was chosen as a magnetic layer on iridium is that there are publication as [59] by Bergmann who has already created this system. He also studied in detail the magnetic structure observed by SP-STM on the first iron layer at 5 K [59]. This magnetic structure was later identified by the Heinze group as a nanoskyrmion lattice [44].

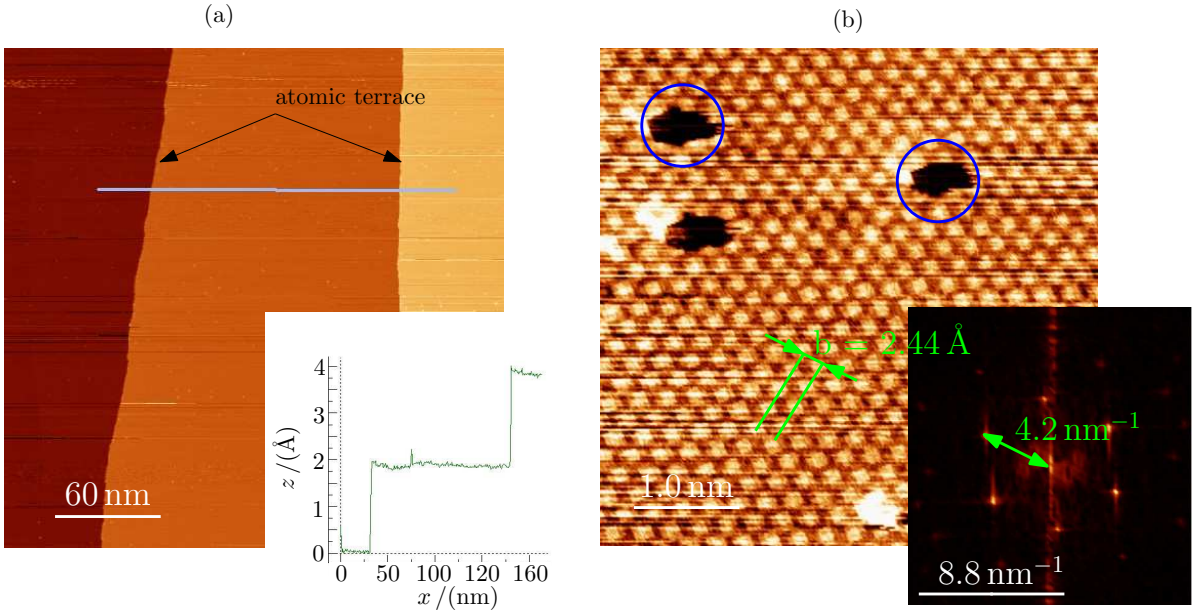

Figure 4.7: (a) Representative image of the cleaned Ir(111) surface with atomic terraces of height $h_{\mathrm{Ir}(111)} = (2.1 \pm 0.2)$ Å. The image set up: $V_{\mathrm{bias}} = 0.75\,\mathrm{mV}$, $I_{\mathrm{setp}} = 500\,\mathrm{pA}$ (b) Image showing an atomic resolution of the surface with missing atoms in the lattice (blue circles). The inset shows the 2D-FFT ($k = 1/\lambda$ convention) of the STM image with measured reciprocal distance between the rows of atoms – the corresponding distance in the real space is represented by green lines in the STM image. The image set up: $V_{\mathrm{bias}} = 4\,\mathrm{mV}$, $I_{\mathrm{setp}} = 26\,\mathrm{nA}$.

Iron belongs to the 3d transition metal groups of the periodic table. Bulk iron crystallizes in the bcc structure with a lattice constant $a = 2.87$ Å. To test the produced SP-STM tips, the aim was to reproduce Bergmann's approach [59] to our system in other words to create *wires* of iron monolayers that should formed at the step edges of iridium.

Iron was deposited using an electron beam evaporator. To achieve the surface diffusion of the iron adatoms towards the iridium step edges, the sample was kept on the temperature $T = 300\,^{\circ}\mathrm{C}$. To create *wires* on the edges no post-annealing was needed. A representative image of the Fe-Ir(111) surface is presented in Figure 4.8. Iron has apparently diffused to the iridium step edges, has creates a monolayer iron *wires* along them, exactly as was described by Bergmann [59].

The height of the iron layer is $h_{\mathrm{Fe}} = (2.5 \pm 0.2)$ Å, which is approximately about 0.5 Å higher than the height of iridium step $h_{\mathrm{Ir}(111)} = (2.1 \pm 0.2)$Å.

4.3.3 Testing of Chromium Tip of SP-STM

The pseudomorphic growth of the Fe on Ir(111) was confirmed by matching the dimensions of the observed iron lattice to the values measured previously on clean Ir(111). To reproduce the observation of nanoskyrmion lattice it is nessesary to use a magnetic tip and perform the measurements at the liquid helium temperature (under 20 K) [59].

For measuring iron monolayers using SP-STM, chromium tip was used in order to observe a skyrmion lattice. Figure 4.9 shows measured skyrmion lattice. The structure was found on *wire* larger than 10 μm. The periodicity of magnetic structure was (7.0 ± 0.2) Å which is comparable with the value for skyrmion lattice [59]. Moreover, due to the absence of an external magnetic

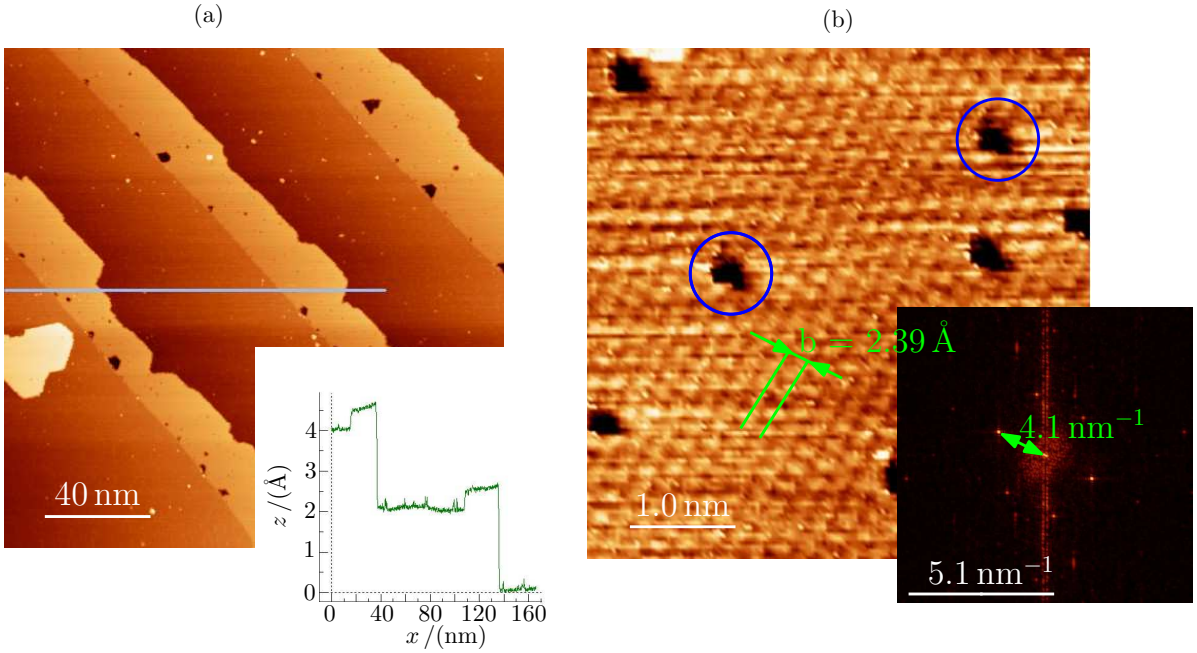

Figure 4.8: (a) Image of the iron wire along the step edge. Around 30 % of iron was deposited on the heated sample surface ($T = 40\,°\mathrm{C}$) using an evaporator. The average iron wire height is $h_{\mathrm{Fe}} = (2.5 \pm 0.2)$ Å and the height of the iridium step is $h_{\mathrm{Ir(111)}} = (2.1 \pm 0.2)\mathring{A}$ Å. The image set up: $V_{\mathrm{bias}} = 750\,\mathrm{mV}$, $I_{\mathrm{setp}} = 500\,\mathrm{pA}$. (b) Atomically resolved image taken on iron phase. The inset shows its 2D-FFT from which the grid constant was determined. The lattice constant of the iron monolayer was determined $b = (2.39 \pm 0.17)$ Å. The image set up: $V_{\mathrm{bias}} = 5\,\mathrm{mV}$, $I_{\mathrm{setp}} = 7.4\,\mathrm{nA}$.

field, spin orientation on the apex of the tip was neither defined nor maintained. As a result, spin orientation could change spontaneously during the measurement. Because the SP-STM is sensitive to the different spin orientations on the sample during one measurement, the measured image is also slightly changed, as seen in the Figure 4.9.

To shortly summarize, the tips were successfully etched and cleaned. By measuring the magnetic structure in the Fe-Ir(111) system, its functionality was confirmed.

4.4 Study of System Nb-Ir(111)

After the tips for SP-STM were successfully prepared and tested, Ir(111) surface was cleaned and Fe was successfully grown on the Ir(111) substrate. The next step of the project was growth study of niobium on Ir(111) substrate. Niobium as well as iron belongs to the group of transition metals. Bulk niobium crystallizes in bcc structure with a lattice constant of $a = 2.87$ Å [11]. Bulk niobium has superconducting transition temperature $\mathrm{T_c} = 9.2\,\mathrm{K}$[1]. Its thin-film growth on the Ir(111) substrate has never been published and therefore no relevant information on the preparation procedure are available.

Before each niobium deposition, the iridium sample was cleaned by the iridium cleaning procedure described in subsection 4.3.1. To deposition exact amount of niobium, niobium evaporator

[1]The temperature, when the niobium become superconductive.

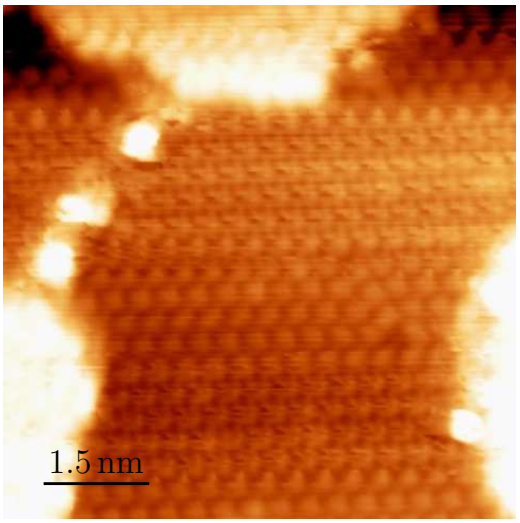

Figure 4.9: Image of skyrmion lattice on iron island on the Ir(111) surface measured by chromium tip. Changes in the image could be explained as a change in spin orientation at the tip apex during the measurements due to the absence of an external magnetic field. Periodicity of skyrmions lattice is $a_{\mathrm{skirmion}} = (7 \pm 0.2)$ Å. The image set up: Temperature $4,\mathrm{K}$, $V_{\mathrm{bias}} = 500\,\mathrm{mV}$, $I_{\mathrm{setp}} = 1\,\mathrm{nA}$.

was used. Niobium evaporator was continuously degassed for five days before the calibration of the deposition was done.

Our next step was to deposit niobium atoms on the surface – roughly 6 % of monolayer (ML) (Figure 4.10). No additional process was used and the sample was inserted into the STM for measurement. The STM images revealed that the niobium deposited at the room temperature forms on or two-layer thick islands with undefined shape on the sample. The size of the islands was random but the island height was $h_{\mathrm{Nb_1}} = (1.5{\pm}0.1)$ Å for the first layer and $h_{\mathrm{Nb2}} = (2.9{\pm}0.2)$ Å for the second layer.

In the next step, the sample was withdrawn from the microscope and annealed at 250 °C for 10 min. Surveying the surface of the sample, we found that after heating the sample, niobium begins to create the island with more compact shapes. Also, the second layer of island with the height $h_{\mathrm{Nb2}} = (2.9 \pm 0.2)$ Å is less frequent. Moreover, contamination of the sample's surface and stripes on the larger islands becomes visible.

In order to form bigger regular clusters, 12 % of ML of niobium was deposited on the sample and annealed. The sample was annealed at different temperatures. The niobium seems to have huge diffusion barrier, because defined islands after annealing at low temperatures were not observed. Niobium islands started to form regular shapes when annealing temperature around 800 °C was reached. In addition, it has been shown that larger islands are formed by annealing the sample over a longer period of time (25 minutes).

The measurement of the system is shown in the Figure 4.11. As was expected, bigger clusters were formed. Islands were mostly double-layered (Figure 4.11 (b)). The higher islands which formed hexagonal shape or wires on the step edges and second lower islands with well-seen periodical structure. The higher islands were (2.2 ± 0.3) Å tall, lower islands were (1.3 ± 0.2) Å tall with surface lattice constant (3.2 ± 0.1) Å. The coverage of the surface with the addition of the first and second layers was determined to be 23 %, 11 % more than what was deposited. Moreover, the edge of the step no longer appears to be a straight line typical for the step of pure iridium, but is

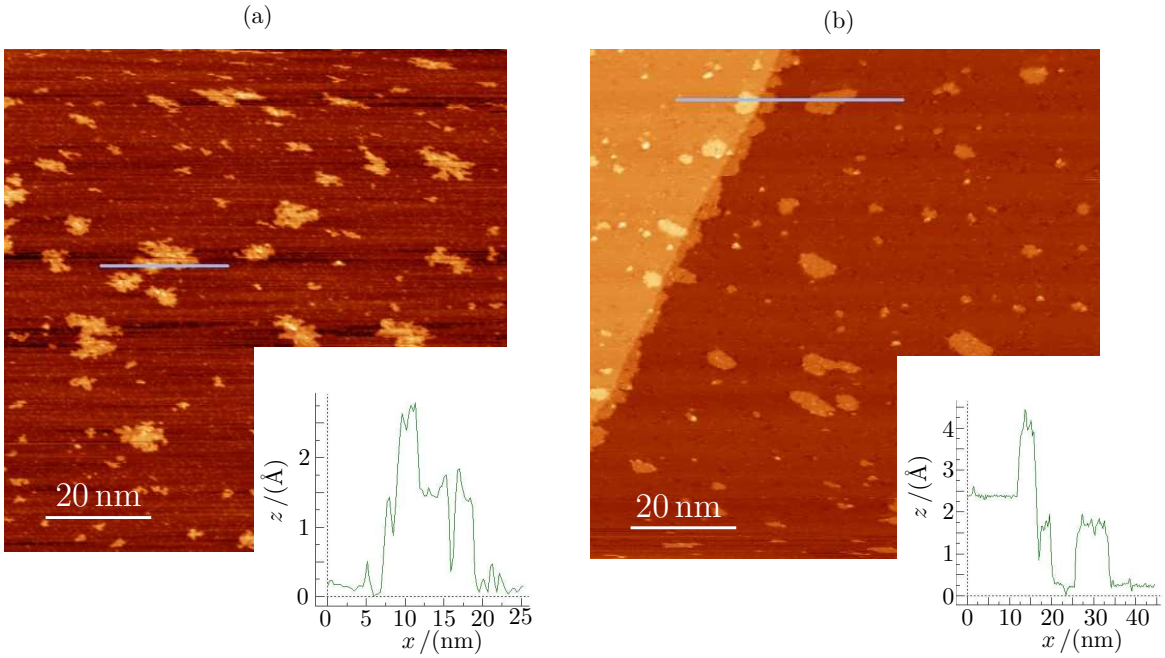

Figure 4.10: (a) Iridium surface image after deposition of 6 % niobium without any post-deposition processes. The height of the first layer of niobium islands is $h_{Nb1} = 1.5 \pm 0.1$ Åand the height of the second layer is $h_{Nb2} = 2.9 \pm 0.2$ Å. he image set up: $V_{\text{bias}} = 750\,\text{mV}$, $I_{\text{setp}} = 500\,\text{pA}$(b)Image of the Ir-Nb system after annealing the sample at 250 ^{o}C for 10 minutes. niobium formed islands with a height $h_{Nb1} = 1.5 \pm 0.1$ Å. Increasing concentration of islands along step-edges is observed. The image set up: $V_{\text{bias}} = 750\,\text{mV}$, $I_{\text{setp}} = 500\,\text{pA}$.

slightly raised compared to the rest of step. Probably the higher islands accumulate near its edge.

Moreover, in the lattice of lower islands black spots with very low electric density were observed. This might be a gap after missing atoms (vacation) or carbon atoms from bulk of the crystal. The sample was annealed at 1000 °C for 25 minutes but density of the black spots was not changed. For this reason black spots can not be assigned to the carbon atoms diffusing from bulk of crystal and therefore the black spots are probably the vacations in the lattice. The lower island was measured at different voltage to see changes (images not shown here). It is possible to say with certainty that the periodic structure is due to topography because no change was observed.

In the next experiment slightly more than half of monolayer of the niobium was deposited on the surface and annealed to 1000 °C for 5 minutes (Figure 4.12).

As it can be seen the behavior of the system matches with the previous experiments. Niobium has again formed two types of islands with a clear predominant representation of the lower islands. In addition, both types of islands grown with well-defined shapes, coverage reduces to 40 % of ML. In addition, the reconstruction was measured on the lower ridges. The black spots had higher density with periodical constant (12.0 ± 0.1) Å (Figure 4.13). Reconstruction was imaged on the structure using different bias voltage between 1 to -1 V to identify electronic structure from topological structure but no changes were recorded.

After the study of lower islands was done, the next step was the detailed investigation of higher islands and the substrate surface.

Figure 4.14 compares both structures (higher islands and substrate). At the first glance, there

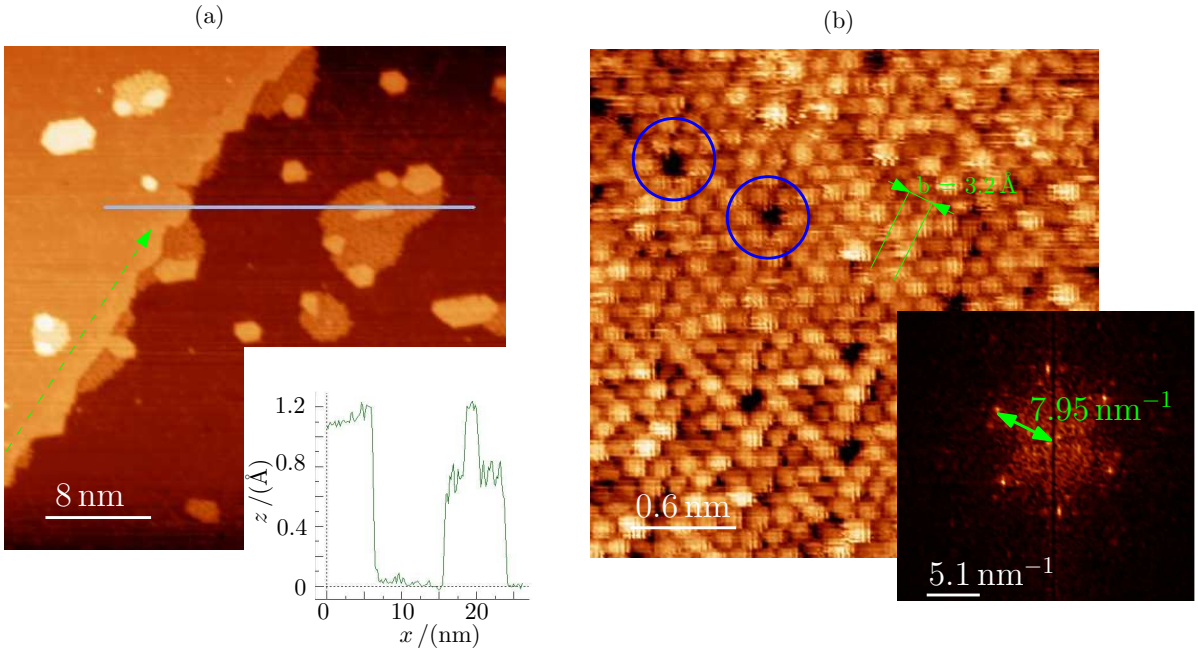

Figure 4.11: (a) Iridium surface image after deposition of 12 % niobium and annealed at 800 °C for 25 minutes. The height of the first layer of islands is $h_{\mathrm{Nb1}} = (1.3 \pm 0.2)$ Å and the height of the second layer is $h_{\mathrm{Nb2}} = (2.2 \pm 0.3)$ Å. The inset image is the height profile of gray line where at the step etch end a slight increase in the hight is seen. The slight increase is probably referring to higher islands. The green dashed line represents Ir step edge. The image set up: $V_{\mathrm{bias}} = 750\,\mathrm{mV}$, $I_{\mathrm{setp}} = 500\,\mathrm{pA}$. (b) The surface detail of the first layer together with the inset FFT image. The periodicity of the structure was determined at (3.2 ± 0.1) Å. Black dots are marked with blue circles that are probably missing atoms in the grid. The image set up: $V_{\mathrm{bias}} = 120\,\mathrm{mV}$, $I_{\mathrm{setp}} = 1.2\,\mathrm{nA}$.

are many similarities between surfaces. There are black spots around triangular structures in both figures. Well-noticeable is undoubtedly the periodicity of background atomic structure on both surfaces. The FFT images of both structures are comparable, and the same three-fold symmetry is found. The FFT image of the higher islands shows also the second three-fold symmetry which can be assigned to the black spots in the image. Lattice parameter of the same three-fold symmetry was determined to be (2.7 ± 0.1) Å.This size coincides with lattice constant of Ir (111).

According to the previous results, it can be said that when niobium is deposited on the surface of iridium and subsequently annealed, it is possible that iridium and niobium forms an alloy on its surface. As niobium reacts with iridium, it is likely that part of the iridium is pushed out of the alloy to make the higher islands that had been observed. These hypotheses, however, are theories built on the background of the experiments, to understand the system in more detail, further experiments are needed. Therefore, a post-experiment was performed. If the iridium and niobium alloy were able to create a monolayer on the substrate, and the monolayer would be superconducting, the order of the structures in the project could reverse and the system can be used.

After previous experiments, the more that 1.4 ML of niobium was deposited and heated (Figure 4.15) (a)). It was found that niobium prefers island growth rather than layered growth. Furthermore, after 12 hours, we checked the system again and we saw that the islands are highly unstable,

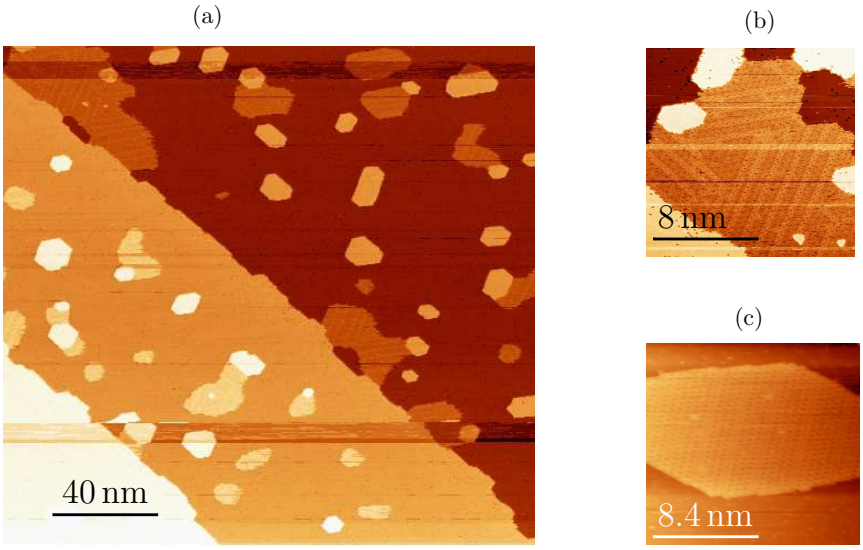

Figure 4.12: (a) Image of the system with two visible island types - higher with hexagonal shape and lower with sharp edges and surface reconstruction. The image set up: $V_{\text{bias}} = 750\,\text{mV}$, $I_{\text{setp}} = 500\,\text{pA}$. (b) Detail of the reconstruction of the lower islands next to step edge The image set up: $V_{\text{bias}} = 750\,\text{mV}$, $I_{\text{setp}} = 500\,\text{pA}$. (c) Details of the reconstruction of the lower island that grew outside the step edge. The image set up: $V_{\text{bias}} = 750\,\text{mV}$, $I_{\text{setp}} = 500\,\text{pA}$.

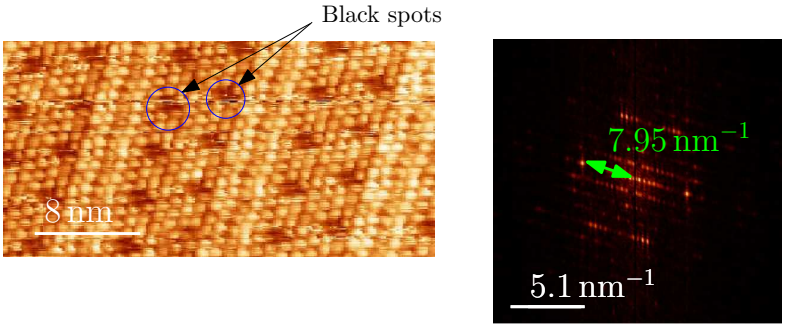

Figure 4.13: Atomic resolution image measured on the lower islands. Reconstruction is well visible. The black dots are periodically situates with the periodicity of $(12.0 \pm 0.1)\,\mathring{A}$. The image set up: $V_{\text{bias}} = 80\,\text{mV}$, $I_{\text{setp}} = 2\,\text{nA}$.

because the top islands were broken down and atoms started to create close layers on the top of the lower islands (Figure 4.15) (b)).

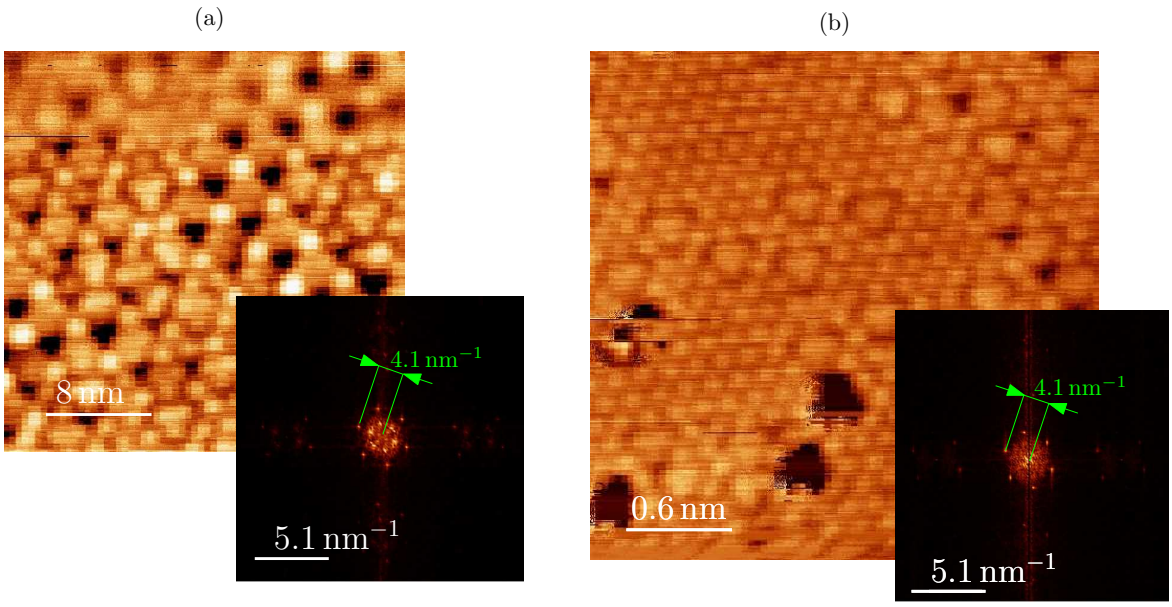

Figure 4.14: Comparison of the surface of the higher islands (a) and the surface of the substrate The image set up: $V_{\text{bias}} = 20\,\text{mV}$, $I_{\text{setp}} = 3.5\,\text{nA}$ (b) with adjacent FFT images. It is possible to notice the similarities between the two images while the main three-fold symmetry in the FFT are the same. The image set up: $V_{\text{bias}} = 22\,\text{mV}$, $I_{\text{setp}} = 1.2\,\text{nA}$.

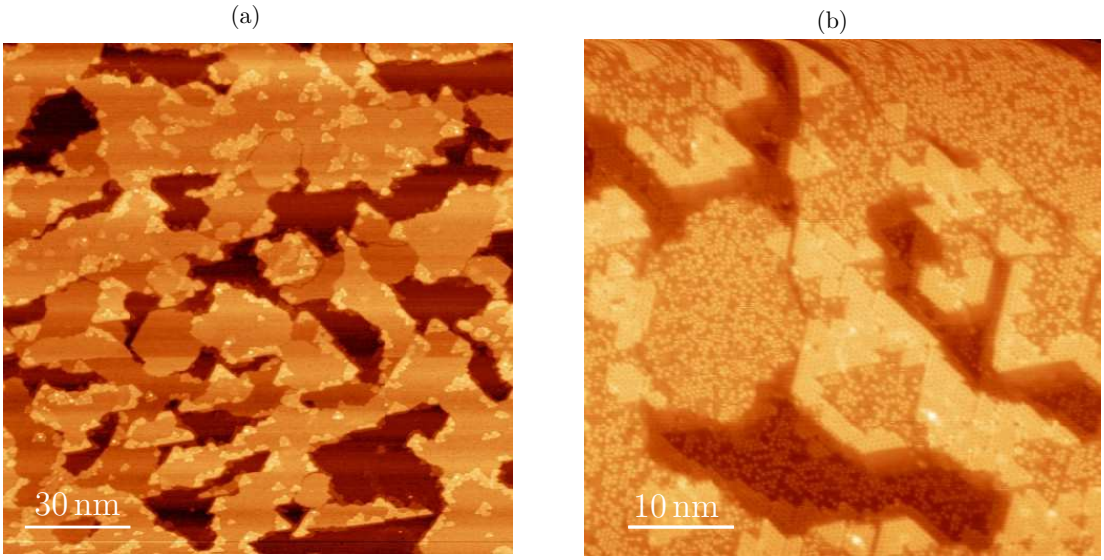

Figure 4.15: (A) Depth 1.4 monolayer niobium and subsequent annealing at 1000 degrees. The image set up: $V_{\text{bias}} = 750\,\text{mV}$, $I_{\text{setp}} = 500\,\text{pA}$ (B) The same system after twelve hours. niobium has tendency to not close layers but to grow the layer on the layer. The image set up: $V_{\text{bias}} = 750\,\text{mV}$, $I_{\text{setp}} = 500\,\text{pA}$.

5 DESCRIPTION OF EXPERIMENTAL LT STM

After my return from the internship in the Netherlands, I started working on developing new experimental LT-STM microscope at the Institute of Physical Engineering (IPE) in Brno. The experimental LT-STM microscope should be able to work in vacuum in temperature range 20 K - 300 K. Thanks to the experience with the functional LT-STM which I have gained in the Netherlands, I have been able to work more efficiently on developing, testing and improving different parts of the experimental LT STM system. The main reason for the development of the the new LT-STM microscope is its location in the chamber *Zeryk* in the vacuum complex *Antonín* (Figure 5.1). Thanks to the location of STM in vacuum complex, it is possible to immediately look at the sample surface after the different process such as annealing, deposition or sputtering. Without the necessity of extracting the sample from the vacuum environment to imagine the surface, the surface is avoided to contamination from air and can be studied further.

In this chapter it is in detail described the new experimental set up which was developed at the Institute of Physical Engineering (IPE) in Brno. The design of the experimental LT STM was adapted to the vacuum complex system (Figure 5.1). Even though the *Žeryk* chamber is separated from the rest of the complex by a bellows and placed on pneumatic legs, vibrations are still transmitted to the chamber. To achieve atomic resolution with the STM, the damping platform for STM had to be designed.

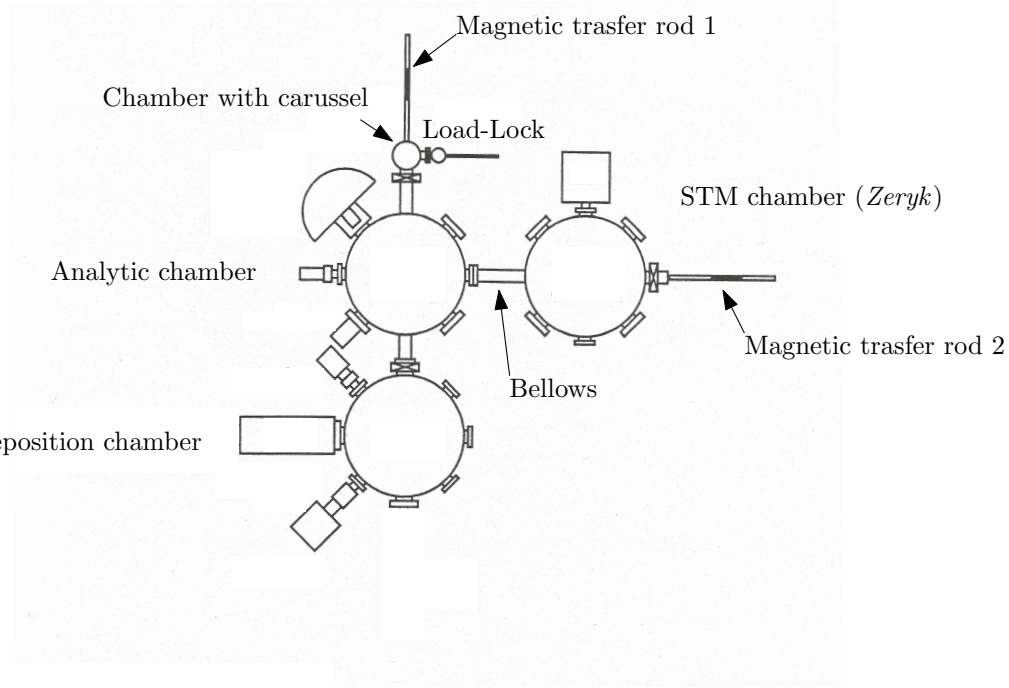

Figure 5.1: Vacuum complex Antonin. The complex consists of three chambers: Analytic chambers , Deposition chamber and STM chamber (*Zeryk*). For vibration isolation of the STM chamber, the chamber is connected to the other by a bellows. The sample is loaded into the complex using the Load Lock. Once the load lock has been pumped, a sample is placed into the sample storage carousel (chamber with carussel) or can be transport over the complex by magnetic transfer rods 1 and 2. Taken from [62].

Several students took part in the design proposal, each of them designed one of the STM parts such as microscope head [23], damping platform and cooling system [29], vacuum transport system [63].

5.1 Damping Platform

Design of the STM platform was created by Ing. Tomas Dao in his master thesis (Figure 5.2) [29]. In addition to the vibration isolation platform, a low temperature system is also present in its work.

In vacuum, heat can spread by two ways - a mechanic contact or radiation [8]. In order to achieve the lowest possible measuring temperatures, the primary cooled component (microscope head) must be separated from the rest of the assembly and therefore its mechanical contact with the rest parts of microscope must be as small as possible. Due to this, the microscope head hangs on the frame via thin stainless steel wire. At the bottom, the tension spring helps to fix the microscope head in the center of the frame. Thanks to small contact area (thin stainless steel wire and spring) the design of the head attachment reduce heat transfer from the frame to the microscope head. To protect the STM from the heat radiation of the surrounding components, a radiation shield is placed in the assembly, which is also cooled.

The system for reducing and damping vibration uses passive damping components (section 2.2). The frame hangs on a long support spring which is hidden in the tube column. This spring eliminate the vibration transfer to the system. For further damping of transferred vibration eddy current damping systems are used. The copper tubes move around fixed magnets and by generated eddy current in the copper tube the magnetic field is generated. The generated magnetic field act against the magnetic field of the magnet and therefore the movement of the frame is reduced.

Next part of the damping system is an anti-damping weight. The anti-damping device was designed to reduce vibrations which can be transferred to the head through wires and cooling braids [1] [29].

Another part of the damping platform is the system for locking the microscope head. By rotation of the locking screw the frame is pulled down until the microscope head sits at the bottom of anti-damping weight which sits at the bottom of the radiation shield. The locking system serves mainly to fix the microscope head inside the radiation shield and allow the insertion of the sample holder or the transfer palette for the tip holder into it. Another useful use of the locking system is when the microphone is cooled. As the head is in a locked position in mechanical contact with the radiation shield, an addition thermal bridge is created. The way, when the microscope head begins to cool down in the fixed position and then, after a certain amount of time, it is released (the microscope head is then cooled only by the braid), a faster cooling is achieved.

5.2 Microscope Head

The microscope head typically contains functions components of STM such as Scanner, coarse positioner, tip and the sample. The design of the microscope head for experimatal LT UHV STM was created by Ing. Michal Pavera PhD. during his PhD studies (Figure 5.3) [23].

At the bottom part of the microscope head are placed the z-coarse positione model ANPz101 manufactured by company Attocube [64], two titan blocks, tube scanner and mechanism for fixing the tip holder (contains from the magnet in the cap for tip holder). Titan blocks have same

[1] A bundle of copper wires

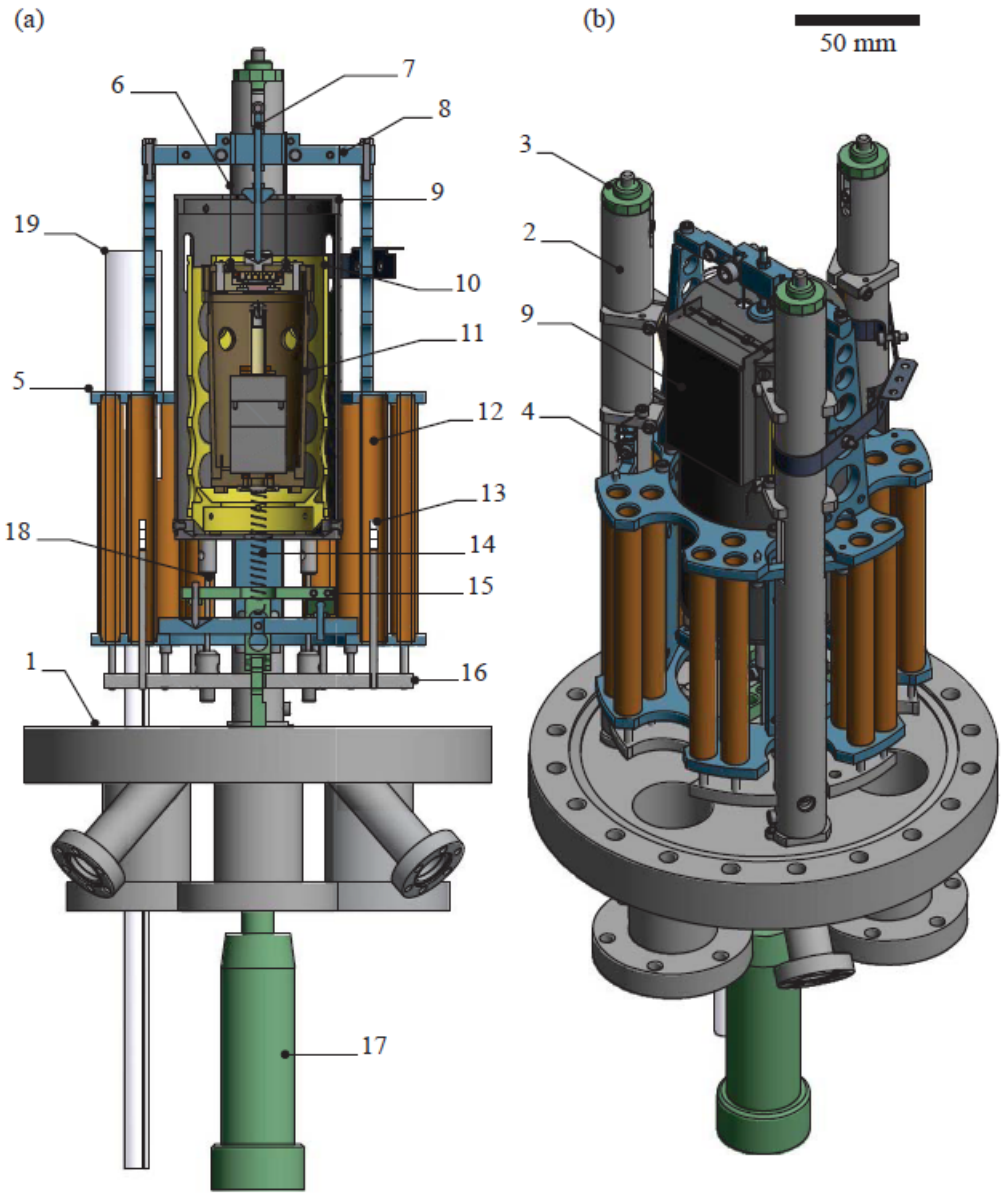

Figure 5.2: Model of the STM microscope with the flow cryostat, a) cut by platform b) isometric view. Individual parts: (1) flange DN160CF, (2) tube column, (3) set screw, (4) supporting screw, (5) platform, (6) stainless steel wire, (7) arresting needle, (8) frame, (9) radiation shield (10) anti-vibration weight, (11) microscope head, (12) copper tube, (13) magnet, (14) tension spring, (15) Arrest warrant, (16) support desk, (17) lock screw, (18) thin-walled tubes, (19) flow cryostat. Taken from [23].

dimensions and weight as x and y coarse positioners which will be installed in the future. At the top of the tube scanner a cap with magnet inside is glued. The tip holder is made of magnetic stainless steel and therefore the magnet attracts the tip holder and fix it in its position.

In the top part of the microscope head the sample holder together with the connectors are placed. Two connectors on the sides are designed for wires of heater and temperature sensors. The

middle connector, which obtains five contacts is for sample plate connection.

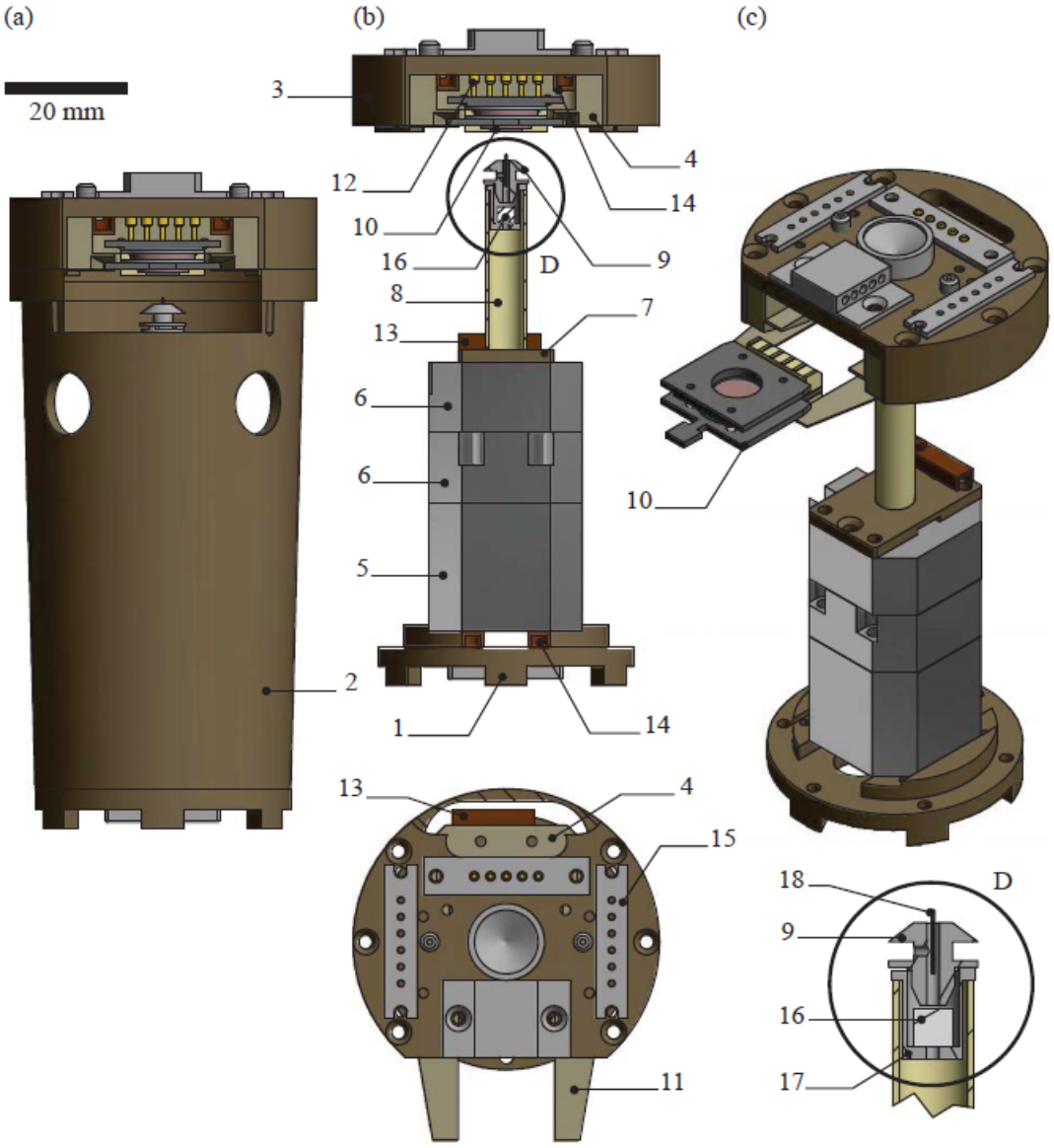

Figure 5.3: Model of the STM microscope head (a) with the cover body, (b) without cover body and top view, (c) isometric view with the sample holder. Individual parts: (1) bottom, (2) cover body,(3) top cap, (4) palette holder, (5) Z-coarse positioner ANPz101, (6) metal blocks, (7) Adapter, (8) tube scanner, (9) tip holder (10) plate with the sample, (11) , pressed sheet metal (12) connector UBEK 12001, (13) temperature sensor, (14) heater, (15) connector, (16) magnet, (17) cap for tip holder, (18) tip. Taken from [23].

The microscope head is also equiped with two temperature sensors PT-100 Platinium resistance thermometers (Figure 5.4) [65]. One of the temperature sensor is placed next to the sample and the second is placed at the bottom of the tube scanner. PT-100 temperature sensors offer excellent accuracy over a wide temperature range (from -245.0 to $+330$ °C) and are used in Four-terminal sensing configuration [66].

For stabilization low temperatures, two heaters are placed above the sample plate holder and

two under z-coarse positioner [63]. Each heater is made of seven SMD 2K70 resistors in parallelly connected to a printed circuit board [67]. The output of each SMD resistor is 0,25 W and therefore The output of one heater is 1.75 W. The minimal power to heat or stabilized the system was calculated by Ing. Pavel Urban Ph.D. and it was established to be 5 W. Our system contains four heaters resulting in total output of 7 W. Our total output is grater than 5 W and therefore conditions for minimal require power has been met.

For better handling and assembly, the temperature sensors and heaters were glueded into copper capsule showed in the Figure 5.4 by thermal conductive epoxid glue H-77 [68].

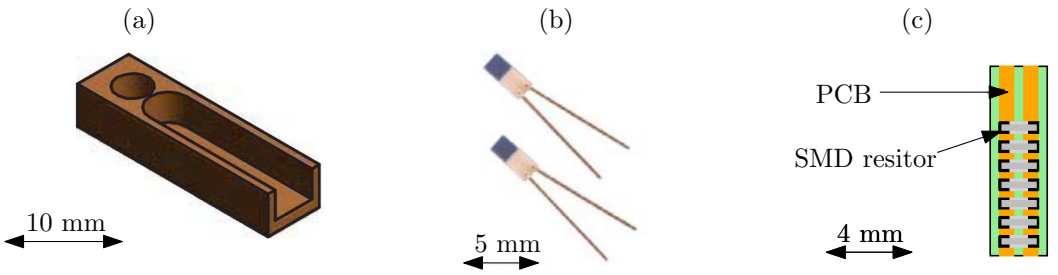

Figure 5.4: a) Model of the copper capsule, b) picture of the temperature sensor PT-100 and c) schema of heater.

5.2.1 Tube Scanner

The scanning in the STM is realized by tube scanner manufactured by company EBL products. Because the first scanner that was used in the STM [23] was destroyed, a new scanner was implement. The type of the new scanner is PZT-4 (EBL 2) [69]. Scanner electrodes distribution is showed in the Figure 5.5. By choosing this distribution of electrodes, each electrode can be controlled independently.

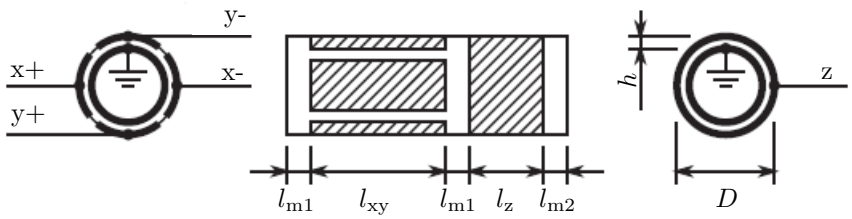

Figure 5.5: Sketch of used scanner in LT UHV STM. The coated parts indicate the electrodes. The individual dimensions are: $l_{xy} = 14.5\,\text{mm}$, $l_z = 10.5\,\text{mm}$, $l_{m1} = 1\,\text{mm}$, $l_{m2} = 2\,\text{mm}$. D=14.75 mm and h=0,9 mm. Taken from [23].

The range of the scanner in the z-direction can be determine as [70], [71].

$$\Delta z = \frac{d_{31} l_z U}{h}, \tag{5.1}$$

where d_{31} is piezoelctric constant and for our scanner is $d_{31} = -173\,\text{pm/V}$ [70] and U is maximally used voltage which is for our system 400 V ($\pm$200). In the same way range in axis x and y can be

calculated:

$$\Delta x = \Delta y = 2\frac{\sqrt{2}}{\pi}\frac{d_{31} l_{xy}^2 U}{Dh}. \tag{5.2}$$

Range of the scanning filed was roughly calculated to be $(650 \times 650)\,\mathrm{nm}^2$ and the range in z direction is 800 nm.

5.3 Cryogenic Systems

Two types of cryostats have been tested for our system in this work – flow and stationary types (Figures 5.6 and 5.7). Both, cryostat and their connection to the microscope are described bellow.

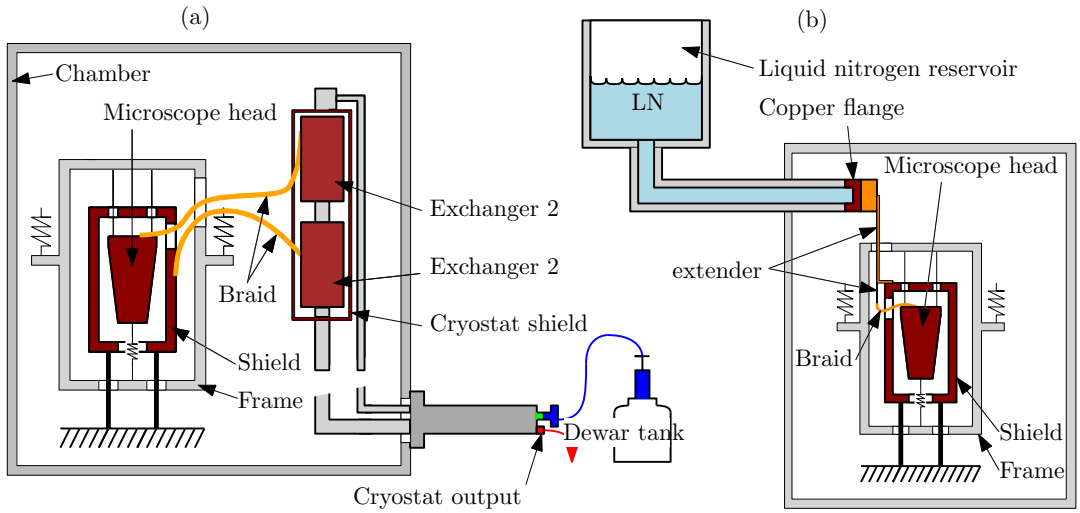

Figure 5.6: Schema of the (a) cryogenics systems left, flow cryostat and (b) stationary cryostat.

- Flow cryostat
  By cooperation with the group from Institute of scientific instruments (ISI) in BRNO the flow helium – nitrogen cryostat was designed, as seen in Figure 5.6 a). The fluid cryostat is divided into two segments. Liquid helium or nitrogen is fed from Dewar tank through the thin pipe to the top of the primary heat exchanger (exchanger 1). The primary exchanger is connected through a copper braid to the microscope head. The liquid helium absorb the heat from the microscope head and continue into the secondary exchanger (exchanger 2) which is connected thought a braid to the radiation shield and anti-damping weight. Heated helium is piped away from the cryostat through cryostat output into surrounding air or into the recovery line, where it can be liquefied and reused.

  The biggest advantages of fluid cryostat is his size. On the other hand disadvantages are huge vibration generation by flow and evaporation of helium or nitrogen in cryostat.

- Stationary cryostat
  The stationary cryostat shown in the Figure 5.6 b) was designed by Tomáš Axman and Ing. Petr Bábor Ph.D. at the IPE. The cryostat consists of a liquid nitrogen reservoir and a long hollow tube ending with a copper flange that leads to the vacuum chamber. At the end of the copper flange copper extender and plates are attached. One plate is firmly screwed to the radiation shield, and the second one is localized close to radiation shield. From the second

copper extender, a copper braid is then drawn to the microscope head of the microscope. This solution should eliminate transfer of vibrations from the cryostat to the microscope head.

Advantages and disadvantages of the stationary cryostat are opposite as compared to the fluid cryostat.

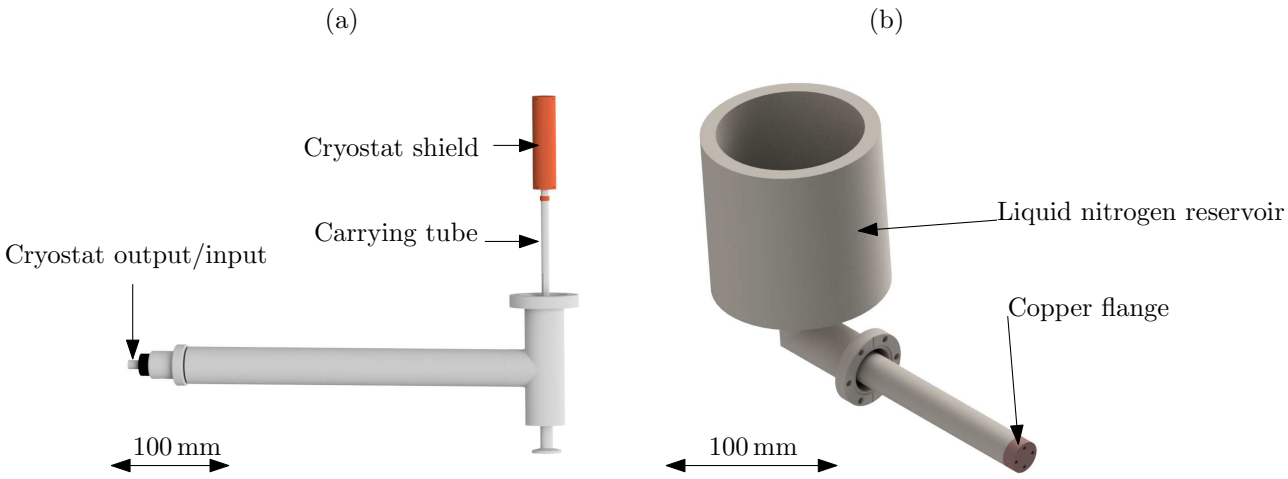

Figure 5.7: 3D models of used cryostats: (a) flow cryostat(b) Stationary Cryostat.

5.4 Tip-Sample Vacuum Transport System

To work with the microscope under vacuum conditions, the new transport system of the sample and the tip in the vacuum chamber was designed [63]. The transport system consisting of vacuum tweezers, sample holder and transfer palette for tip holder (Figure 5.8). The biggest issue concerning the insertion of samples and tips to the microscope head is off-axis access between the microscope head entry and the position of the vacuum manipulator called wobble stick. To solve the problem, the vacuum tweezers (Figure 5.8) were designed and then attached to the end of the wobble stick. In the tweezers, the sample holder and transfer palette for tip holder (Figure 5.9) has one degree of freedom. Because of the design of tweezers, the sample holders and transfer palette for tip holder can be easily inserted or removed from the microscope head or the carousel as is shown in the (Figure 5.9).

5.4.1 Improving the Transport System

When the microscope was tested, few limitations appeared. For example, the samples in the sample holder can be heated only to temperature of 500 °C due to the epoxy adhesives H-22 which is used for contants [72].

Next part, which needed to be improved, is the palette for tip transfer. The tip holder is fixed in the palette by pre-tensioned plates (Figure 5.10). To pull out the palette for tip transfer from the microscope head, the tip holder, together with the tip, is extended by a z-coarse positioner to the maximum length in the microscope (Process of the inserting/removing tip holder is shown in Figure 5.9). Then a transfer palette is inserted into the microscope. The tip holder has to

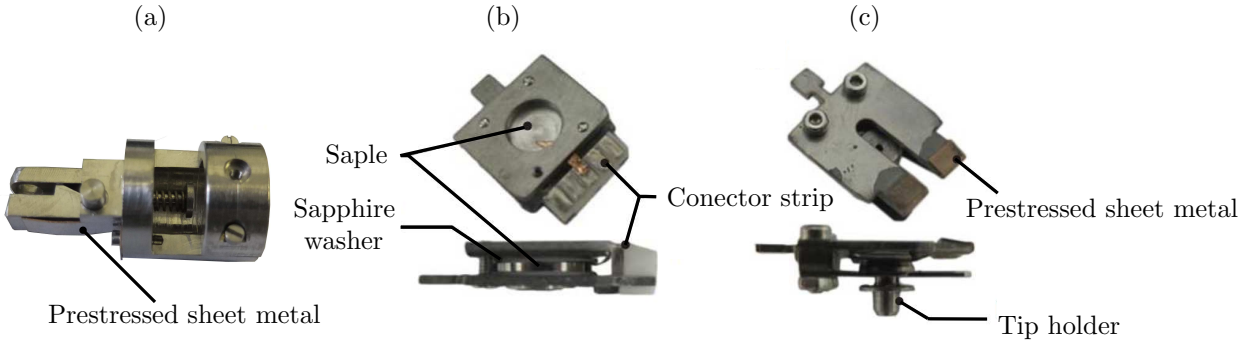

Figure 5.8: The system for sample and tip transfer into the microscope in vacuum chamber. (a) Vacuum tweezers (b) sample holder (c) transfer palette for tip holder.

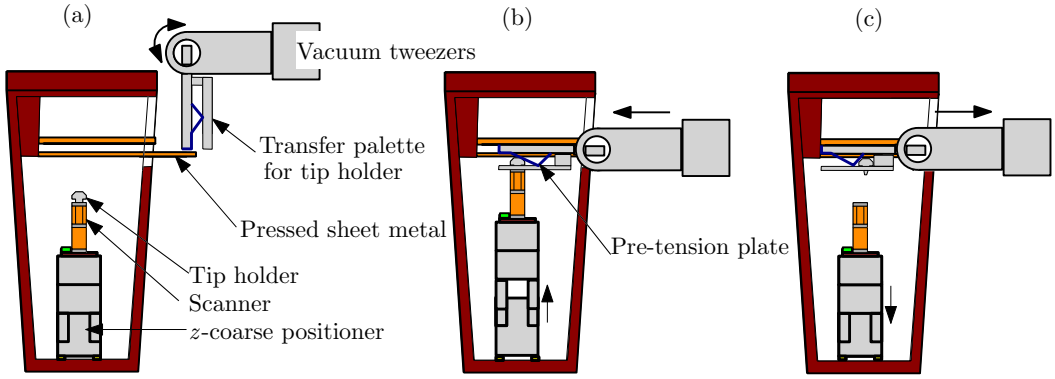

Figure 5.9: Schema of the loading process of a transfer palette for tip holder with the removing the tip holder from the Scanner palette into the microscope. (a) Due to the gravity, the palette hangs down from the vacuum tweezers. Using the vacuum tweezers, the palette is placed on the pressed sheet metal out of the microscope head. (b) The scanner is extended at the maximal his length by z-coarse positioner. Using a rotary motion of the vacuum tweezers, the palette is rotated to the horizontal position and by pushing it forward it is inserted to microscope head. By pushing patette forward, tip holder has to overcome the preload of the pre-tension plate. (c) The tip holder is fixed in the palette and the scanner is retracted. In this moment the pallet can be remove from the microscope head by vacuum tweezers. To insert the tip holder, the sequence of steps is reversed

overcome the force of the pre-tensioned plates after it is fixed in defined position in palette. In the extreme case, the force could destroy the scanner.

Finally, a change was done in the tip fixation in the tip holder. The existing solution fixs the wire by a screw. This approach is inappropriate for several reasons. When the probe tip is approaching the sample by a coarse positioner, the vibrations are generated. In some cases the screw is released together with the tip. In other case the tip holder can rotate in a scanner, and the position of screw may prevent inserting of the transfer palette into of the microscope.

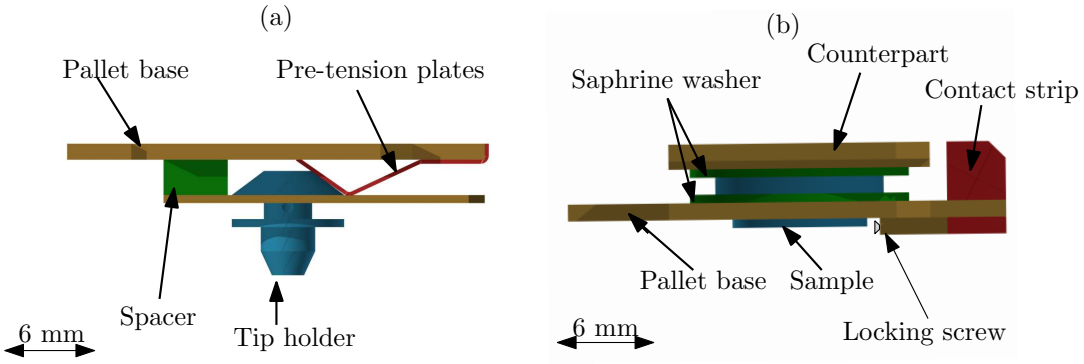

Figure 5.10: 3D model of old transport design with labels: (a) transfer palette for tip holder and (b)sample holder.

Sample Holder

The main requirement for a new palette was to increase the maximum allowed operating temperature from 500 °C to 1200 °C. Such a high temperature is needed during the annealing in the cleaning procedure. The old design of the sample holder had five contacts which were made from epoxy adhesive on the contact strip made of the Macor (Figure 5.10). The design of the new palette is the same as the original (Figure 5.8) except for a contact strip. In the new design, there is only one contact made from phosphor bronze plate, which is placed between two ceramic plates (because of electrical isolation) and it is fixed by stainless steal anvil. The palette base and counterparts are made of molybdenum because of its good thermal conductivity (Figure 5.11). Sapphire washers were used to electricaly isolate the sample and to achieve high thermal conductivity at the same time.

Another requirement was to make parts easier to manufacture. For this reason in the new design the recess and the locking screws were eliminated (Figure 5.10). Thanks to these modifications, it is possible to produce all the parts up to the anvil by a laser and the only work in the mechanical workshop is the production of threads in the palette and the anvil production.

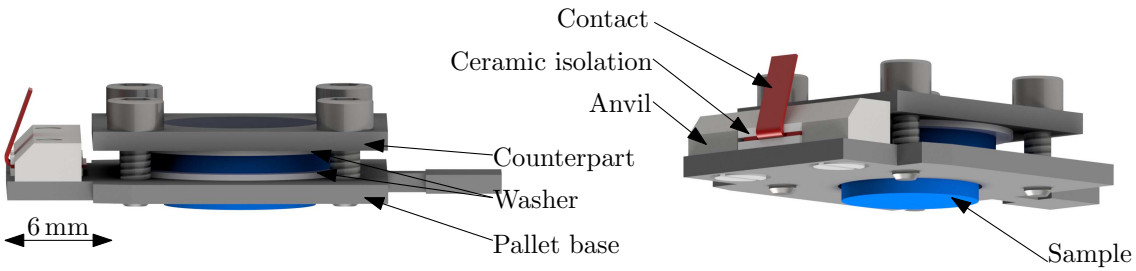

Figure 5.11: 3D model of the sample holder with descriptions of individual parts.

Transfer Palette for Tip Holder

As was already mentioned in the introduction of this section, the old design of the palette created a lot of pressure on the scanner when the palette was inserted into the microscope (Figure 5.8). A

major design problem lies in the absence of a sharp displacement of the x and y axis scanner. The only movement can be done in z axis, in the direction of the sample.

The design of the palettes is based on the similar design (Figure 5.12). The difference is in fixing the tip holder in the palette by magnet instead of pre-tensioned plates. The magnet is placed in mechanical recess in the spacer. Thanks to this, the tip holder is secured in the palette. For better guidance of the tip holder when it is inserted into the microscope a counterpart has a V - cut and for increased safety of the tip transport, a groove is also cut in the palette base. Moreover, the groove provides a clear view of the tip for ex-situ tip treatments like e-beam or ion bombarding, depositions.

There are no special material requirements on the palette parts and therefore all parts are made of stainless steel.

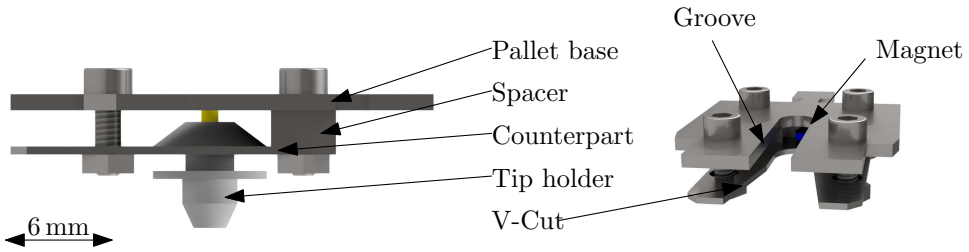

Figure 5.12: 3D model of the palette for tip transport holder with descriptions of individual parts.

Tip Holder

Comparison of the new and the old design of the tip holder is shown in Figure 5.13. In the case of the original tip holder, it often happens that the tip will bend when the screw is tightened (Figure 5.13 (a)). Furthermore, in some cases the tip holder would get stuck in the palette during the tip transfer due to the screw. This would typically result in dropping of the tip or impossibility of palette insertion into the microscope.

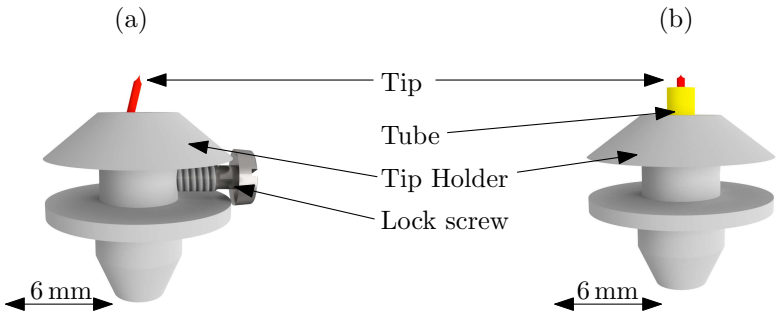

Figure 5.13: The model of the tip holders design:(a) the old design of tip holder using the screw for fixing the tip, (b) new design using the single-use tube for fixing the tip.

In the new design, a fixed attachment is introduced using a single-use hollow tube. The tube has a slightly larger outer diameter than the hole diameter in the tip holder. This little conception

makes it possible to snap a tube into the holder with a force. The tip is then inserted into the tube and it is fixed by squeezing the end of the tube with the pliers.

5.5 Electronics

The individual components of the microscope are connected with the control electronics by three different types of wires from LakeShore company [73]. The coaxial cables LakeShore type SS [74] were used for signals from the tip, sample and the z-piezo fo scanner. The signals from that parts play the most important role in the functionality of the microscope, and therefore it is important to maintain their purity of signals. The temperature sensors were connected by cable type DualTwist 72AWG[2] and the The DualTwists 36AWG cable was used to connect the rest of the components [75]. The 72AWG and 36 AWG cables were used intentionally, due to their low thickness and low coefficient of heat dissipation. That that, heat and vibration transfers to the microscope head are minimized. The detailed electrical diagram of the microscope connection can be found in [63].

Because the tunneling current size during STM measurement is in nA range, it is necessary to use amplifiers (Figure 5.14 (b)) [76]. By tunneling amplifier the tunneling current is converted to voltage and amplifies the signal in order of tens of magnitude.

The main control unit of the STM is shown in the Figure 5.14. From the top to the bottom of the shelter followig controlers are positioned: ANC300 of company Attocube for control coarse positioners [64], homemade high voltage controller for control tube scanner [77], SPM controller Mk2-810 of company SoftDB with control software GXSM [78]. From the PC, the movement of tube scanners, reading the signal of measurement from tunneling current amplifier and feedback loop can be controlled.

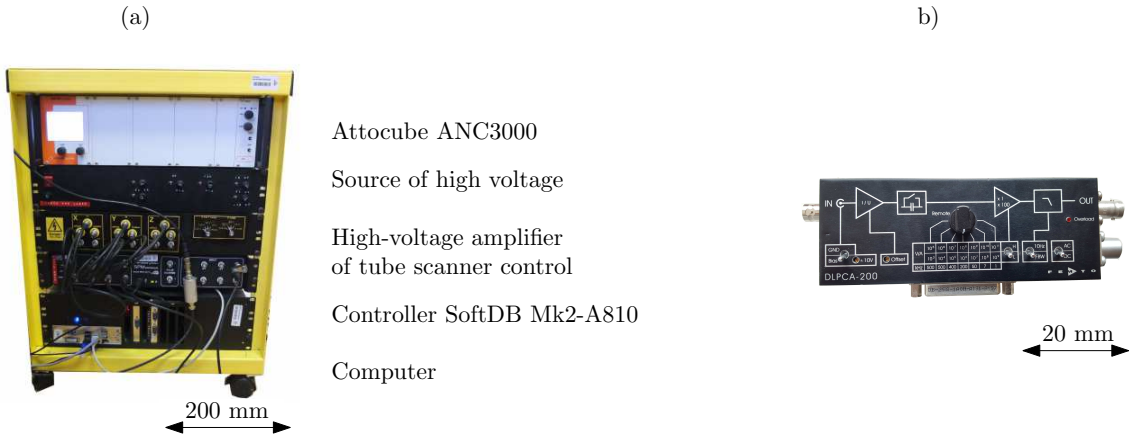

Figure 5.14: The picture of the control electronics: a) main electronics, b)amplifier.

[2]American wire gauge (AWG)

6 TESTING OF EXPERIMENTAL LT STM

This chapter describes tests and improvements of the experimental LT STM. Firstly, the basic information about Highly Oriented Pyrolytic Graphite (HOPG) are present. Then the summary of previous results are shown. The main part of this chapter is then focused on the results from following tests of LT STM in the air and vacuum conditions are shown. At the end, the tests of stationary and flow cryostat are presented.

All images shown in this chapter are performed by Pt-Ir tips (made by cut-off method) on HOPG sample at room temperature.

6.1 Highly Oriented Pyrolytic Graphite

All tests in this chapter were performed on the Highly Oriented Pyrolytic Graphite (HOPG) sample which was bought from the Brooker company [79]. The HOPG sample was selected for initial testing due to the well known structure (Figure 6.1 a)).

HOPG is a unique form of material that is produced by decomposition of hydrocarbon gas at high temperatures in vacuum. Thanks to this procedure, an ultra-purity material with mechanical, electrical and thermal properties, which are much better compared to the conventional graphite is created.

Graphite belongs to lamellar materials and consists of identical stacked planes (Figure 6.1 b)). Carbon atoms within a single plane interact much stronger than with those from adjacent planes. That explains the lamellar behavior of graphite. Each atom within a single plane has three nearest neighbours. The network of carbon atoms connected by shortest bonds looks like honeycomb. This two-dimensional and single-atom thick plane is called *graphene*.

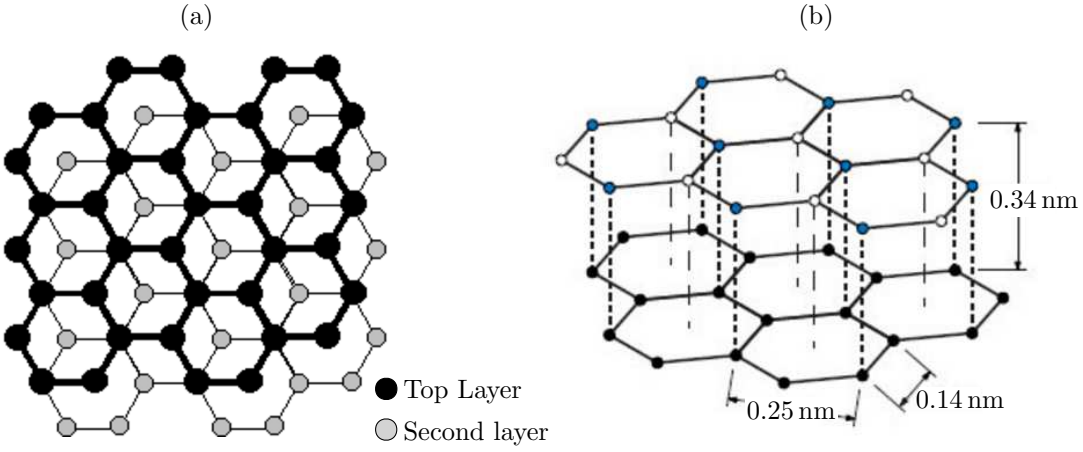

Figure 6.1: (a) Top view on model of HOPG surface; (b) 3D lattice model of HOPG.

Another advantage of the HOPG sample is that the graphite does not tend to oxidize. However, if the surface of HOPG is contaminated, it is possible to remove the top most layers from the sample, and thus receive a new clean surface. To create clear HOPG surface in easiest process the tape is needed. In first step the piece of the tape is stuck to the surface. Then the tape is pulled off. The topmost layer of the sample should stick to the tape, leaving a freshly exposed graphite surface.

6.2 Summary of Previous Results

The microscope was assembled and put into the operation for the first time during my bachelor thesis [63]. First tests were performed on two samples: Highly Oriented Pyrolytic Graphite (HOPG) and gold test grating (Figure 6.2).

Figure 6.2: The best images taken during the first test of the experimental LT STM. (a) Image of the HOPG surface, (b) image of the gold test grating.

The Figure 6.2 (a) shows the best measured image. There are no features in the picture, which would confirm the microscope functionality. The second image in the Figure 6.2 (b) shows the best measurement of the golden grid sample. However, during the measurements on the golden grid the microscope was not able to keep constant distance between the tip and the sample and therefore in most cases the tip crashed after a while of scanning of the image.

6.3 Testing of Experimental LT STM in Air Conditions

All tests in this chapter were carried out in the clean laboratory at the Institute of Physics Engineering (IPE).

Before the new tests of the microscope's functionality started, the new scanner was implemented because previous scanner was destroyed during the testing of the cooling system. Parameters of the new scanner with the expected ranges for each axis are discussed in section 5.2.1.

The old system had a problem with wires management around the microscope head. The wires were sometimes in contact with radiation shield resulting in unwanted heat and vibration transfer. Therefore the support plates were produced (Figure 6.3). The plates are used for leading the wires from the bottom of the microscope head to the hole in the radiation shield by pressing them against the cover body of microscope head .

The detailed wiring diagram can be found in the appendix.

New measured images of the HOPG sample show features which look like sharp edges and they have believable depth profile values (Figure 6.4 (a)). However, the problem occurred after scanning the entire image. Certain edges did not show any changes throughout the measurement period. If the scanning direction was rotated by 90°, the measured image showed center symmetry features (Figure 6.4 (b)). The same features were visible on the entire sample area. These results were showing abnormal function of the microscope and therefore all hardware parts were checked. After checking the microscope's electric wires, a short circuit between the two electrodes on the electric

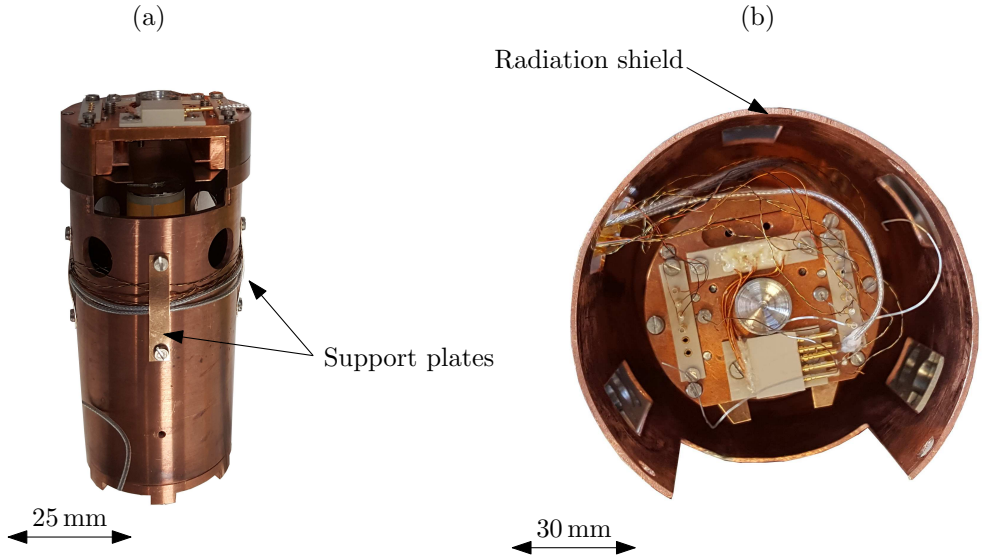

Figure 6.3: (a) Microscope head with installed support plates. The cables leading from bottom of the microscope head are pushed by the supporting plates to the microscope head along the path to the hole in the radiation shield. This avoids contact between the microscope head and the radiation shield.(b)The microscope head is placed in the radiation shield.

clutch outside of the microscope head was found. That led to the disconnection of the electric signal from one electrode and caused the STM to scan mainly in one line.

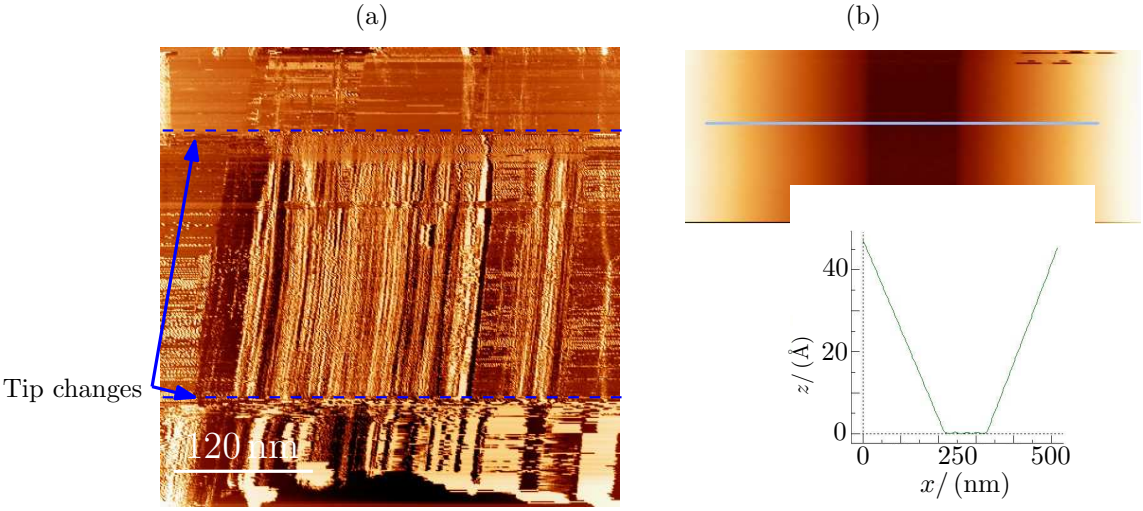

Figure 6.4: (a) Measurement in the vertical direction of the line of the sample does not change except the spontaneous tip change. (b) Scanning the sample in horizontal direction. Visible center axis symmetry. The scales in the images do not match the real values and are only indicative because the scanner has not yet been calibrated. The image set up: $V_{\text{bias}} = 0.25\,\text{V}$, $I_{\text{setp}} = 1.5\,\text{nA}$.

While the wires were reconnected, purity of the signal from the tip and the sample (how much electrical noise is measured in the non-contact state) were also checked. The abnormal noise in the

wire carrying signal from the sample was measured by an oscilloscope when the tip was sufficiently distant from the sample that the tunneling current was not generated (non-contact state). Detailed investigation revealed that the shielding of the wire was damage therefore the wire was replaced. The comparison of the original and new wire signal is shown in the Figure 6.5.

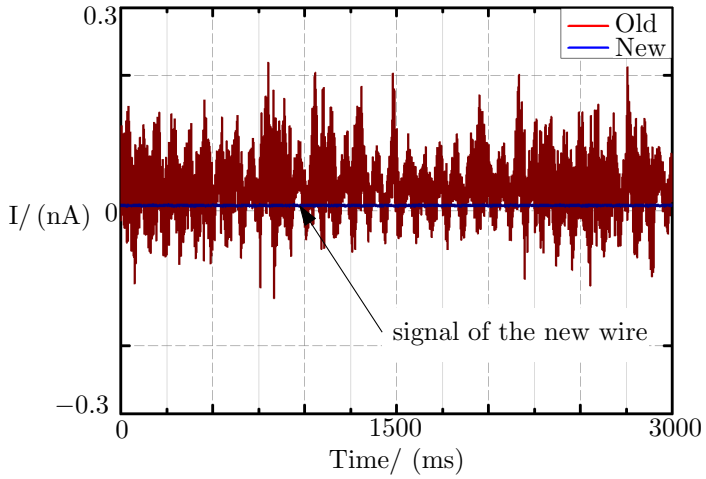

Figure 6.5: The graph of the signals of new (blue line around zero) and old wire connected to the sample. Signals from both wires are amplified by amplifier to order of 9.

After reassembly of the microscope, the image in the Figure 6.6 was measured. The image shows a realistic sharp line which could be a step edge of HOPG monolayers with a realistic sample depth (Figure 6.6). However, maintaining the tunneling current at a constant value was not possible using the feedback. The tip was probably hitting the sample during the measurement. The measured current oscillated between the maximal value of the measured current - 10 nA (the tip crashed into the sample) and the current value of 0 nA which corresponds to the situation when the tip is too far from the sample and the tunneling current is not measured.

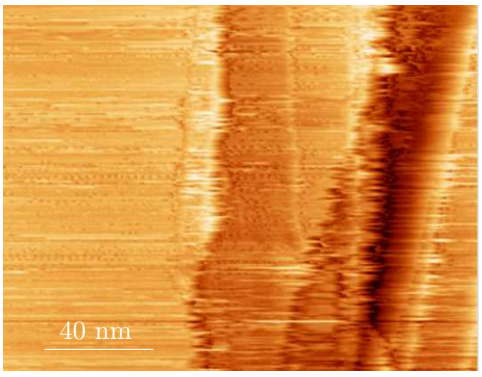

Figure 6.6: (a) Image of the HOPG surface after the damaged wire was replaced. The scale in the image does not match the real values and is only indicative because the scanner has not been calibrated yet. The image set up: $V_{\mathrm{bias}} = 0.1\,\mathrm{V}$, $I_{\mathrm{setp}} = 1\,\mathrm{nA}$.

After further examination, we noticed that the noise in wires was negligible in the lock position when the microscope head was fixed. However, in the loose position, the noise is no longer as

extreme as it was in the wire with disturbed insulation but the noise is still visible (Figure 6.5). It was found that the noise was caused by the weak electric connection between the microscope head and the frame. In our case, the microscope head was hanged on two thin stainless steel wires, which are not capable of discharging the charge and therefore the grounding of the measure is weak and noise is present in the measurement.

To solve this problem the microscope head was attached to the frame by threaded rod. In future (where the cryostat will be connected to the head via copper braid) the copper braids will improve the grounding of the microscope head, and therefore this solution will not be needed anymore. Also, this temporary solution does not affect the function of the damping platform or functionality of the microscope. The image taken after the microscope head was fixed to the frame via threaded rod is shown in Figure 6.7.

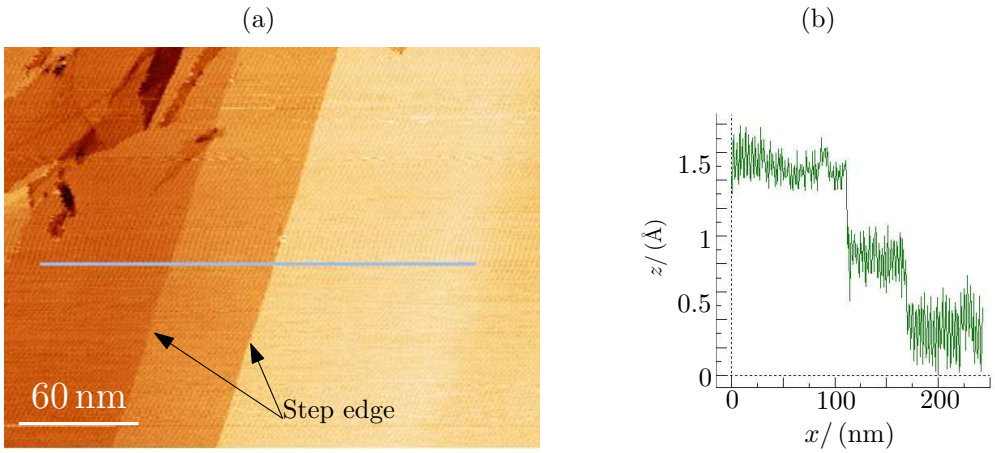

Figure 6.7: (a) Image of the HOPG surface after the microscope head was attached to the frame via threaded rod. The noise in the image was determined at 233 Hz. (b) Depth profile around the gray line. The image set up: $V_{\mathrm{bias}} = 0.15\,\mathrm{V}$, $I_{\mathrm{setp}} = 1\,\mathrm{nA}$.

In the image clear lines are visible, the straight lines are called step edges and they indicate the end of the HOPG layers. In our case they are used for calibration of the scanner in the z-axis. Moreover, the image has confirmed the functionality of the microscope. The background noise in the image can still be clearly seen. The frequency of the noise was determined to be 233 Hz. This frequency may correspond to a combined interference of working machines with human walking and noise from the surroundings. The problem with the noise is due to inefficient damping. At that moment the microscope used only damping platform for vibration isolation as was described in chapter 5. Typically one stage damping system is not sufficient and therefore second stage of damping system is planned for tests in vacuum chamber. In further tests, the microscope was suspended on the console via rubber ropes. The picture of hanging system and his vibration spectrum can be found in Figure 6.8.

Further testing has shown that the vibration is sufficiently low for measurement if the microscope is suspended. The measured images no longer showed signs of vibrations. The only problem was the instability of the tips during the measurements. However, for some measurements, the tip became stable in short periods of time (Figure 6.9). The spectrum was acquired by FFT of time-recording stretching of z axis of the scanner in the contact state (when tunneling current is generated) at one point of the sample when the feedback was switched on.

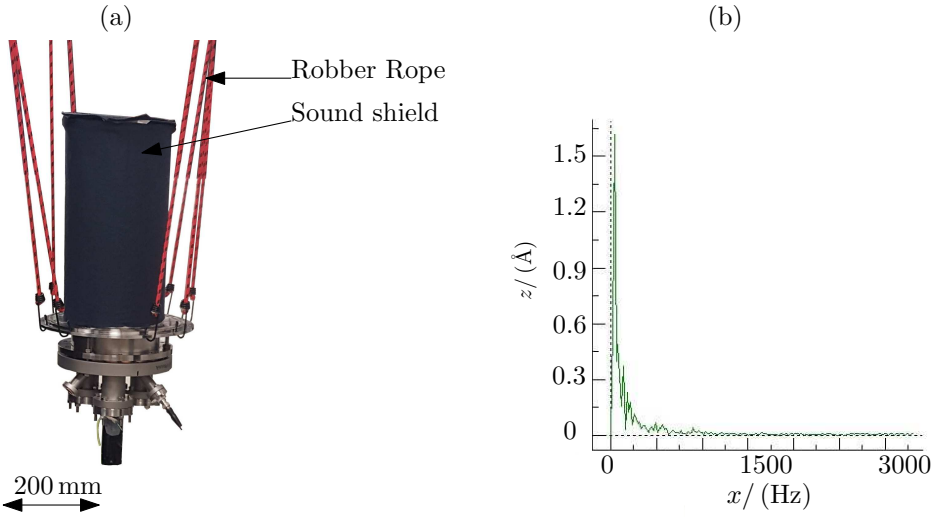

Figure 6.8: (a) The picture of the microscope which is suspended on the console via rubber ropes. For isolation of sound noise the microscope is covered by sound shield. (b) Spectrum of vibration of the microscope

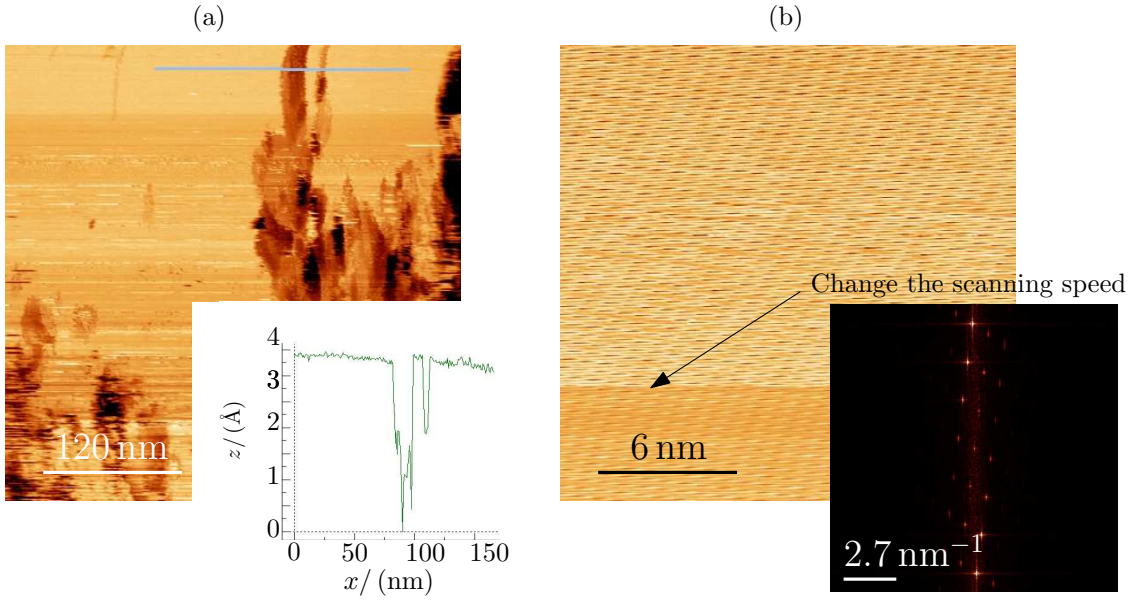

Figure 6.9: (a) Image of the HOPG surface after the STM was suspended on the console via rubber ropes with inlet depth profile around a gray line. $V_{\text{bias}} = 0.20\,\text{V}$, $I_{\text{setp}} = 0.75\,\text{nA}$. (b) The close image of the sample with visible periodical structure. During the scan the scanning speed was changed to confirmed that the periodical structure is not the noise. The inset shows its 2D-FFT. The scale in the images do not match the real values and are only indicative because the scanner has not yet been calibrated. The image set up: $V_{\text{bias}} = 0.07\,\text{V}$, $I_{\text{setp}} = 2\,\text{nA}$.

At the moments when the tip was stable, attempts were made to obtain atomic resolution. Under room temperature conditions, atoms on the surface together with the whole sample are

constantly moving due to the energy obtained from surrounding particles in form of heat. This movement is called a thermal drift [80], and therefore a low temperature measurement is required to obtain an atomic resolution for most of the samples.

The atomic resolution of the HOPG in the Figure 6.9 (b) was achieved in extra short scanning times when the entire scanning image takes a few seconds. Due to the fast scanning and temperature drift, the atomic structure is stretched to one side. To confirm the atomic resolution in our image, the scanning speed was changed during the image acquisition. Because the frequency of the lines in the image has not changed, the lines in the image are not caused by noise and they represent atomic rows. Furthermore, the FFT image obtained from the STM image shows three-fold symmetry, which is typical for atomic resolution images. In our case, the three-fold symmetry is a bit tilted which is probably caused by thermal drift and high scanning speed. If the inverse FFT is applied only on main points of three-fold symmetry (Figure 6.10 (a)), then into the final filter image the structural model of HOPG can be fit.

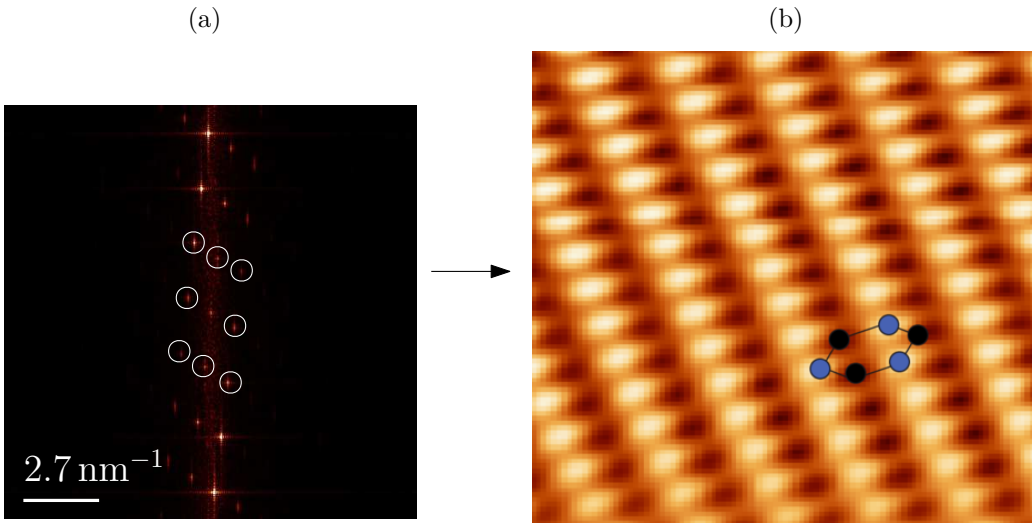

Figure 6.10: (a) Close view at the FFT image of the STM image from Figure 6.9 (b). (b) Inverse FFT of the main points of the three-fold symmetry marked by white circles. The graphite structure was put into the image which confirm the atomic resolution.

The measurements of the HOPG confirmed the functionality of the STM to achieve atomic resolution.

6.4 Testing of Experimental LT STM in Vacuum Conditions

Next step for testing the microscope was to insert the STM into the *Zeryk* chamber which is part of the *Antonin* UHV vacuum complex (Figure 6.11). To achieve better isolation of the chamber, the chamber was placed on the pneumatic legs which isolate the chamber from the vibration transfer from the floor.

After the vacuum system and the microscope were put into full operation state, the UHV conditions were reached in the chamber. All tests were carried out during the night hours when it was possible to disconnect most of the devices in the vacuum complex system. In this case, the background noise and the vibration sources in the labs became minimal. The image of the

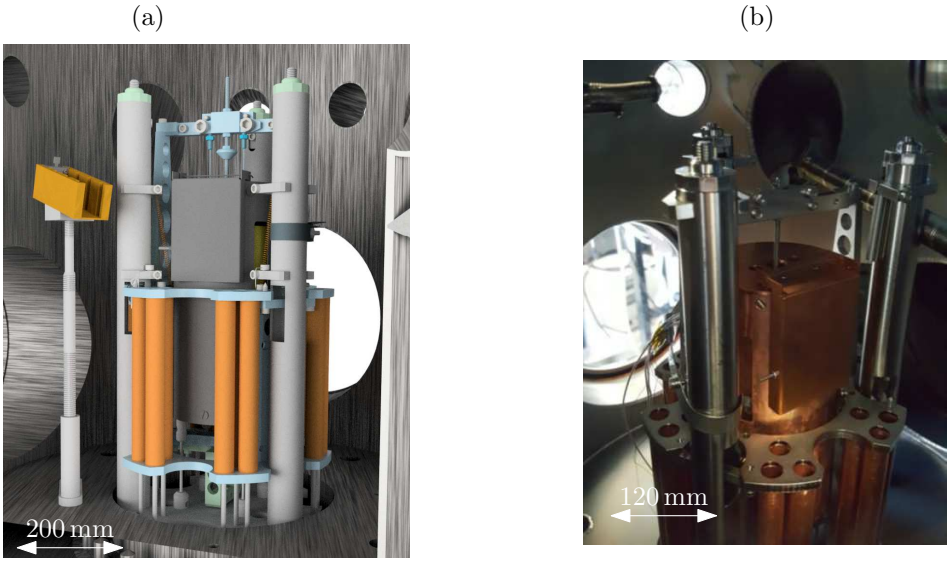

Figure 6.11: (a) The CAD model of STM in the vacuum chamber *Zeryk*, (b) the image of the microscope in *Zeryk chamber*.

final measurements can be seen in the Figure 6.12. Unfortunately, attempts to improve the tip under UHV conditions failed, but the image is sufficient to demonstrate STM functionality in UHV conditions. In addition, a measured spectrum of vibrations was similar to when the atomic resolution in air conditions was taken. However, in the Figure 6.12, the spots with vibration features are visible. These spots probably correspond to the random start of the machines around the microscope like a nearby elevator.

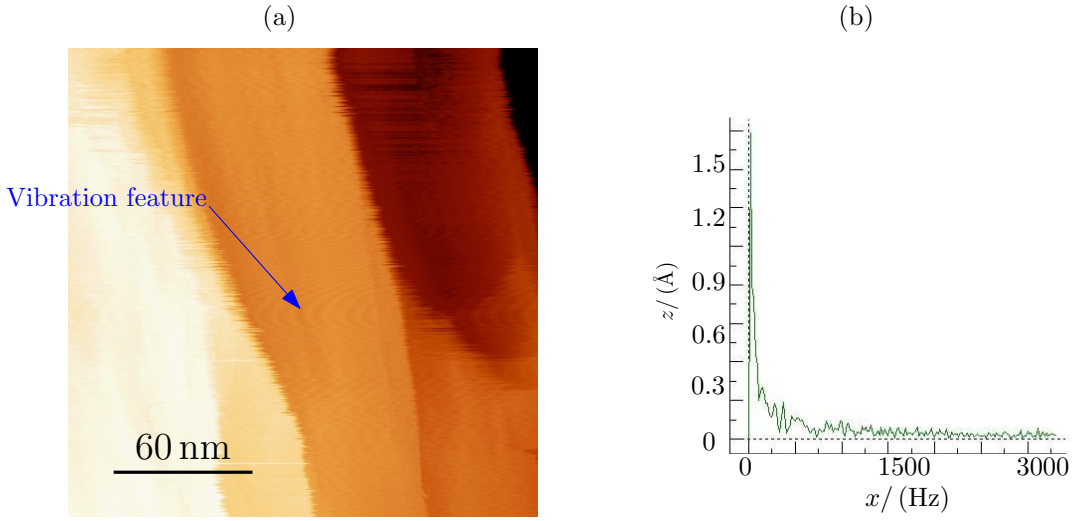

Figure 6.12: (a) Image of HOPG taken at UHV conditions. The step edge are visible, but different parts of image contain the noise features, which were caused by random start of the machines in the vacuum complex. b) Spectrum of vibration of the microscope. The image set up: $V_{\text{bias}} = 0.5\,\text{V}$, $I_{\text{setp}} = 0.75\,\text{nA}$.

6.5 Testing of Low Temperature Systems

As was already mentioned, two types of cryostats were designed and tested for our experimental LT-STM (Figure 5.7). A flow cryostat was developed in collaboration with the Czech Academy of Sciences in Brno (IST). Hovewer, during the tests (which are shown below) of the flow cryostat it was discovered, that major constructional issues prevented future use of the cryostat in the vacuum chamber *Zeryk* (Figure 5.1). Cryostat design changes were therefore suggested. Unfortunately, the production capacities of the Academy failed to deliver the cryostat before this work was completed and therefore the second cryostat was implemented and tested.

The test of the flow Cryostat was done in collaboration with Cryogenic group at institute of scientific instrument (IST) where the cryostat was mainly designed and fabricated. A special small vacuum chamber pumped by scroll pump to medium vacuum level (10^{-1} Pa) [22] was used for the low temperature test.

For tests, six temperature sensors were mounted on the microscope (Figure 6.13) and one on the cryostat input. Four PT-100 and PT-1000 sensors around the STM. The first two sensors are permanently placed on the microscope head. One was at the bottom of the tube scanner and the second was mounted on the sample palette holder. Together they were used to investigate heat transfer along the microscope head. Additional sensors were placed on the anti-vibrations weight and the radiation shield. The last two sensors were mounted on a flow cryostat and they were types CERNOX CX-1050-SD [81] LakeShore Model 350 cryogenic temperature controller was used for readout of all the sensors [82].

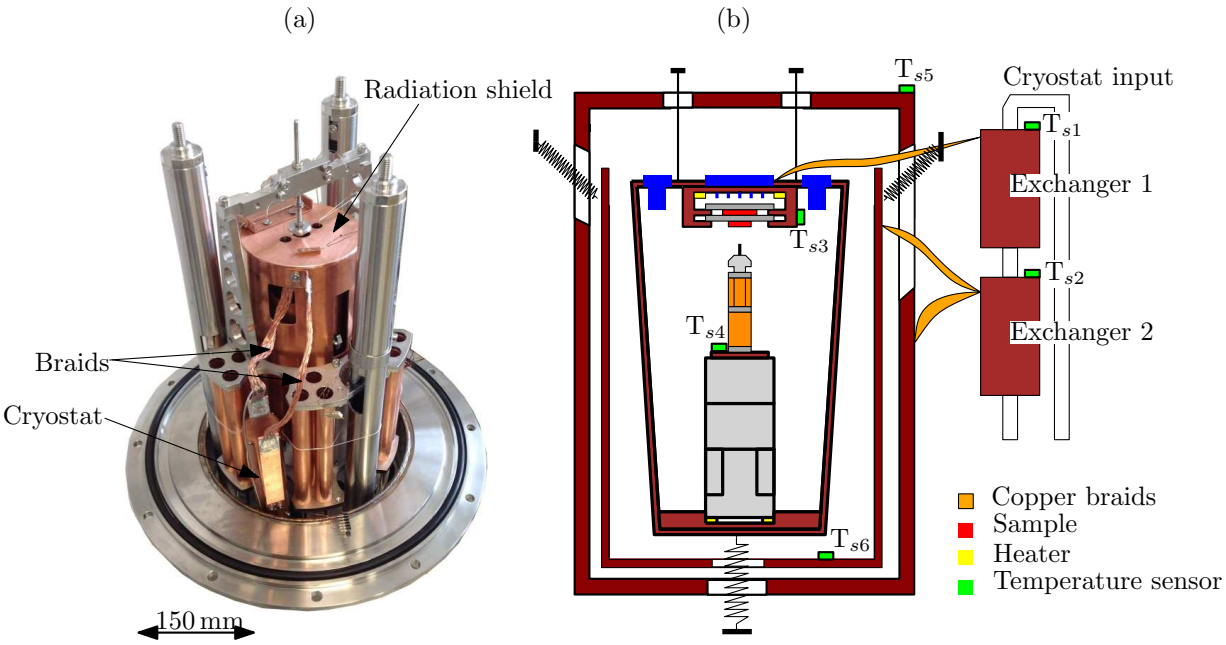

Figure 6.13: (a) The picture of the STM with mounted cryostat, (b) the diagram of cryostat implementation with the marked positions of thermal sensors and heaters.

At the first glance, it can be seen (Figure 6.13 (a)) that the cryostat has an insufficient length. In an ideal case, the top of the cryostat should be aligned with the top of the radiation shield. For short version, which was tested, long braids were needed for connecting to the cryostat and other parts of the STM. The longer the braids are, the more heat they absorbed in form of radiation from

surrounding parts (chamber and some parts of microscope which are at room temperature). The next problem of the old design of the cryostat was the position of the copper braid outputs (heat exchangers). In the old version the braid connections were placed 180 °C apart which made the installation more complicated considering that both are attached on the same side of the cryostat. In addition, for implementation of the cryostat into the *Zeryk* chamber carrying tube was too short (Figure 5.7). Those reasons made the cryostat unusable in our chamber and the cryostat had to be redesigned.

The new design of the flow cryostat is shown in the Figure 6.14. The tube carrying the heat exchangers(carrying tube) was extended and the copper connector was used in the middle of the tube for centering the exchangers in the chamber. Braid outputs are rotated 90 °C from each other for easier installation. In addition, electric feedthroughs are in part of new design to bring more connectors for heat sensors or other electric devices to the system.

(a)

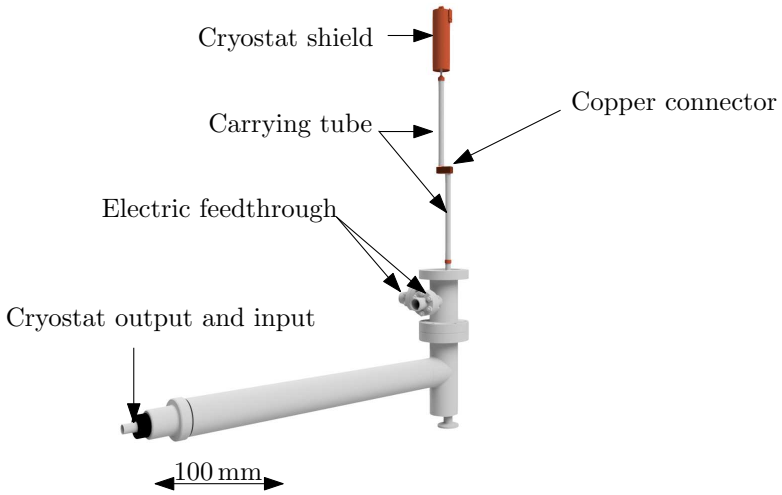

Figure 6.14: The model of tip holders design: (a) the old design of tip holder using the screw for fix the tip, (b) new design using the single-use tube for fix the tip.

6.5.1 Test of Flow Cryostat

However, in spite of the technical deficiencies, tests of the cooling system were performed with two coolant flows, liquid nitrogen and liquid helium on the old design.

Flow cryostat - Nitrogen

The Figure 6.15 shows the results of the tests for the flow system with liquid nitrogen used as coolant. As can be seen, the cryostat worked well and the exchanger reached the temperature 78.5 K in 50 minutes. The cooling time of the other parts of the microscope were longer. The minimal temperatures at each sensor which were reached after 8 hours of cooling and can be find in the table 6.1. The results show that the final temperature of the antivibration weight is higher

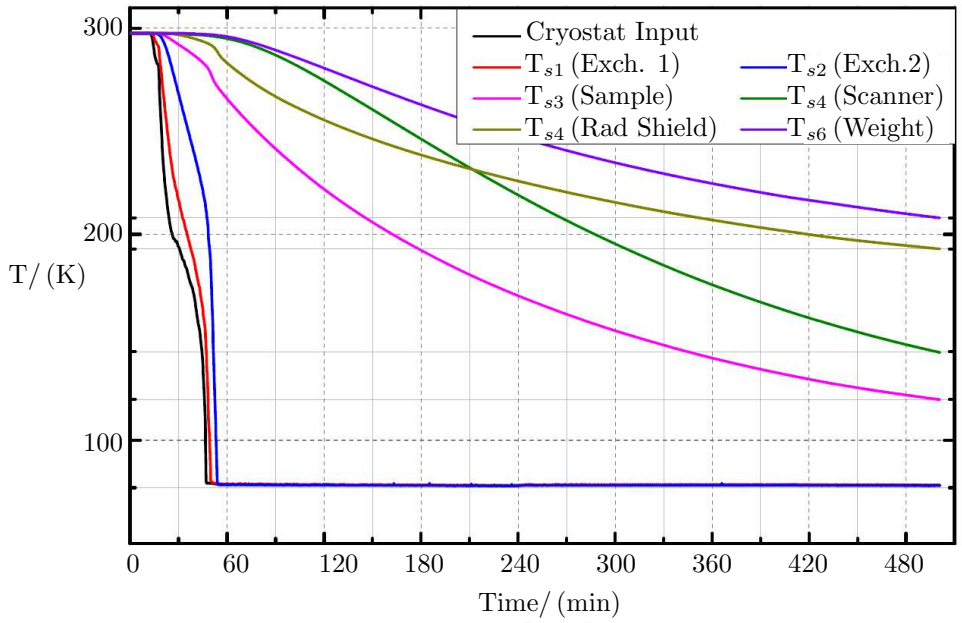

Figure 6.15: Graph of the cooling process using liquid nitrogen as a cooling medium.

than the temperature on the radiation shield and on the microscope head. This does not correspond to the theoretical model of the system. According to the model [29] the lowest temperature should be measured at the microscope head, followed by the weight and shield should be the warmest part. There are two reasons to explain why the weight is warmer than the surrounding microscope parts. The main reason of this behavior are the cables which lead to the microscope head. The cables (at room temperature) were attached to the weight before they reached the microscope head to dampen the vibrations. The second reason is that the weight hangs on three springs that are attached to the tube columns (Figure 5.2), which are at room temperature.

Table 6.1: The minimal temperatures measured at different spots of the system during cooling by liquid nitrogen

Sensor	Input	Exch. 1	Exch. 2	Sample	Scanner	Rad. Shield	Weight
Label		T$_{s1}$	T$_{s2}$	T$_{s3}$	T$_{s4}$	T$_{s5}$	T$_{s6s}$
Temperature/ (K)	78	78	78	120	143	193	208

Flow Cryostat - Helium

Another test of the cooling system was done using helium as a coolant. The cooling of the system is shown in the Figure 6.16. Again as in the previous results the exchanger worked well and reached the temperature of 4.6 K and 11 K in 30 minutes, the oscillation of readout is caused by flowing and evaporation of helium inside the cryostat. The complete results of the lowest temperatures of system parts are in summarized in the table 6.2. Unfortunately, the sensors PT-100 and PT-1000 are calibrated only down to 30 K, and therefore the data under 30 K are not available. That can be seen in the Figure 6.16 (pink curve T$_{s3}$), where the signal was lost at the temperature under

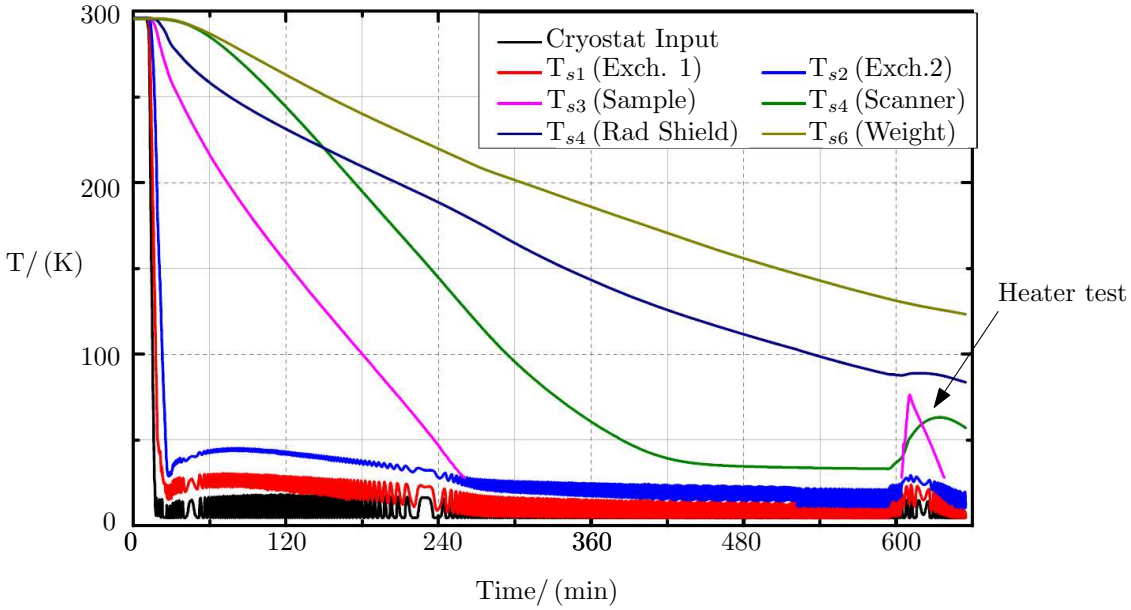

Figure 6.16: Graph of the cooling process using liquid helium as a cooling medium. At 600 minutes, temperature stabilizers (heaters) were switched on for a few seconds.

30 K and found again when the heaters were turned on. However, the STM is currently planned to be used at the liquid nitrogen temperature, where the range of sensors is sufficient.

Table 6.2: The minimal temperatures measured at the different spots of the system during cooling by liquid helium

Sensor	Input	Exch. 1	Exch. 2	Sample	Scanner	Rad. Shield	Weight
Label		T_{s1}	T_{s2}	T_{s3}	T_{s4}	T_{s5}	T_{s6s}
Temperature (K)	~ 6	~ 6	~ 6	> 33	37	83	122

During the test, the functionality of the heaters in the microscope head were also tested. The current was applied for 600 min test time and as it can be seen the temperature increase up to 79 K at the sample and 68 K at the scanner. This test confirmed the proper function of the heater. Feedback loop, however, has to be implemented for precise temperature control as can be seen on the graph in Figure 6.16 where even a short heating has affected the temperature for tens of minutes.

6.5.2 Test of Stationary Cryostat

After tests of the flow cryostat and the design a new cryostat module, tests of this stationary cryostat were performed at our faculty in the *Zeryk* chamber (Figure 6.17). In this case the weight was removed from assembly because the centering of the system in the vacuum chamber was not possible. The weights were still touching the surrounding walls, and only access for adjustment through one of the ports of the chamber (Figure 6.17 (a)). The change compared to the previous test was number of sensors which were limited due to the number of electrical contacts through

the feedthroughs. Four sensors of PT-100 or PT-1000 type were used in the test. Two in the microscope head, one at the top of the radiation shield and one at the cryostat end.

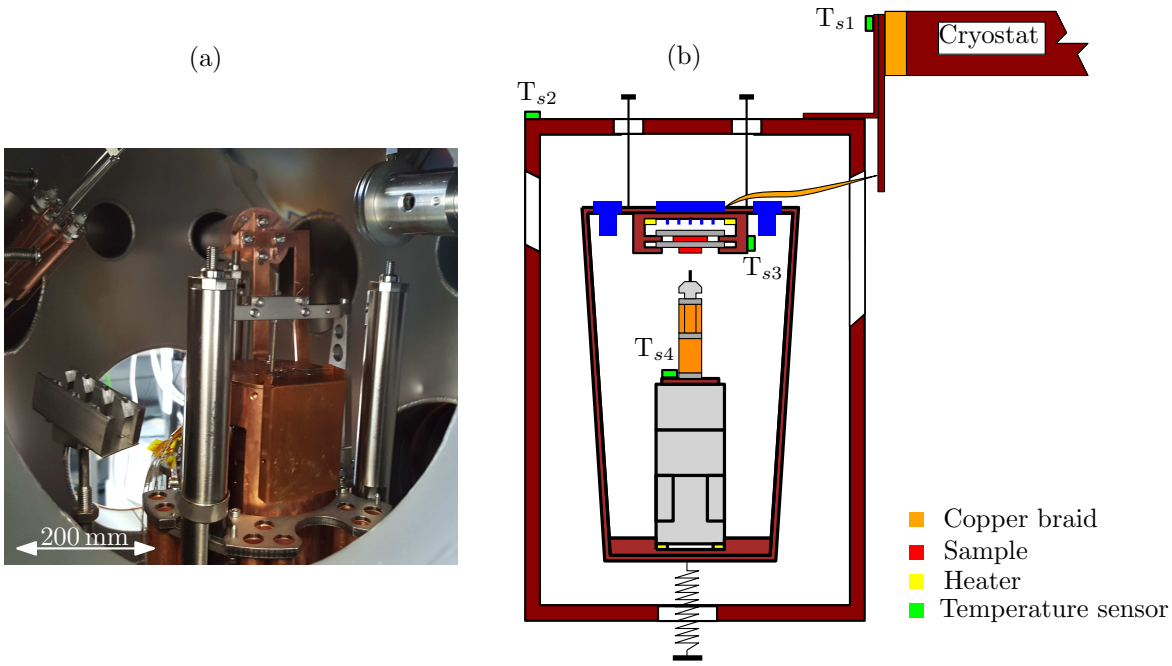

Figure 6.17: (a) The picture of the STM microscope in the vacuum chamber with connected cryostat, (b) the schema of the measure STM and cryostat with a distribution of sensors.

The cooling process can be seen in the Figure 6.18 and corresponding the lowest temperature of each curve is shown in the table 6.3.

Table 6.3: The minimal temperature measured at the different spots of the system during cooling by liquid helium and using the stationer cryostat as cooling device.

Sensor	Cryostat	Rad. Shield	Sample	Scanner
Label	T_{s1}	T_{s2}	T_{s3}	T_{s4}
Temperature (K)	79	109	112	130

During the tests, the impact of the lock mechanism system was also tested. At the start of the test, the microscope was fully locked. At this point, the microscope head was seated in the locked position and was held in this position by the locking screw pushing at its top. After 780 min (Area II) the locking mechanism was slightly loosened so that the locking bolt did not force against the microscope head. It can be noticed that the temperature first decreased drastically, after some time (but for about 30 minutes) the temperature stabilized and started to decrease more slowly than in Area I. At this point it was clear that the position of the locking system is crucial for cooling speed. Therefore, after 1160 minutes (Area III), the locking mechanism was loosened a little bit more so the microscope head still sat at the bottom of the radiation shield, but the locking bolt was no longer pushing against it. This new position has been found to be the most appropriate. When the locking mechanism was released a little bit more, the temperature on all parts of the microscope started to rise, and when the locking mechanism was tightened the temperature drop has slowed down. After 1440 min (Area IV), the microscope head was fully released. The increase

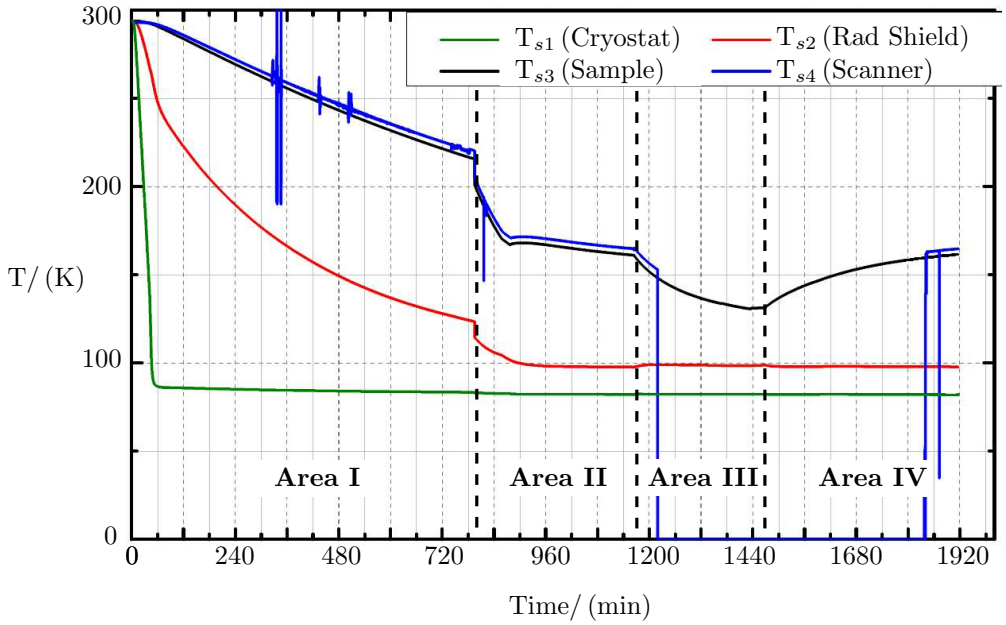

Figure 6.18: Graph of the cooling process using stationary cryostat and liquid nitrogen as a cooling medium.

of the microscope head temperature was observed. In fully released position, the heat from the microscope is removed only by the copper braids and additional heat is introduced by electric cables. This caused a problem with the warming of the microscope head, since the cables were no longer attached to any intermediate stage. Head was thus exposed to heat from the wired which came into the system at room temperature.

The solution of this problem for a future system, can be solved in two ways. The first way would be to attach a stronger braid that would take more heat out of the system, but it would also bring more vibration to the system. The second way was proposed where the wiring would be attached to the radiation shield before they go in to the system. Wires should be will be gradually cooled by a radiation shield and therefor faster cooling of microscope head and lower minimal temperature should be achieved.

SUMMARY AND OUTLOOK

This thesis deals with the UHV LT-STM. In the beginning, the basic theory of the STM is briefly discussed, together with the basic theory of individual parts of the microscope. The practical part is then divided into two parts.

Preparation of superconducting-magnetic interface

In this part of the thesis the results of my abroad experience in the SPM group of Alex ako Khajetorian in the city Nijmegen are presented. A new, long-term going project studying the superconducting-magnetic interface was launched in the group. Since the project was only in its beginning, my task was to manufacture, optimize, and subsequently test the SP-STM tips. The tip was done at he Omicron etching station. After the etching process of a chromium wire was optimized and first tips were produced, the system for testing the tips had to be made. For the testing, the Fe-Ir (111) system was chosen. The first reason of this selection was the usability of the system in the overall project (magnetic -substrate). Secondly, the reason was the existence of a published article, where instructions how to achieve the system are published. The success of the cleaning process of the iridium was confirmed by achieving atomic resolution of the Ir(111) lattice. In the next step iron was successfully grown on the Ir substrate. The etched chromium tip was then annealed in a vacuum and tested on the Fe-Ir system. By measuring the magnetic structure (probably nanoskirmions, because the lattice constant matched) on the surface of the iron, the functionality of the tip was confirmed.

In the next part of the project which was assigned to the growth study of the superconductor on the substrate (Iridium in our case). In this study was found that, by deposition of niobium on the cold sample, indeterminate shape clusters of islands are formed. If the sample was annealed long enough, two types of islands were created. Higher islands with a height of $h = 3.11\,\text{Å}$ and with a regular hexagonal shape, and smaller islands of a random sharp shape and with a visible periodic structure on the surface. The lattice constant of the periodic structure was determined to be $a = 2.31\,\text{Å}$. Then after the deposition of higher amount of niobium and annealing of the system, both types of the islands increased their size. After closer examination of the surface of higher islands and their comparison with the surface of the substrate, similarities were found. Surfaces contain the same periodic structure. Therefore it was concluded, that higher islands are most likely iridium with defects in some lattice points. The lower islands were defined as alloys and the Nb-Ir system was judged to be unsuitable for the aims of the project. As a last resort, a large amount of niobium was deposited on the surface and then the system was annealed. This was done because if the alloy of niobium and Iridium behave as a superconductor, materials in the system could be reversed (magnetic-suprecondative-substrate). The project can than continue with the system. Unfortunately, after the deposition, it turned out that the resulting structure grows island on the island instead of the closed layers and therefore the research system was left and the group switched to other materials such as Lead and Tantalum.

Experimental UHV LT STM

The second part of my thesis is focused on the experimental LT-STM microscope. In the first section of this part, the experimental LT-STM is described in details and the results from the last testing are summarized. Thanks to the experience gained in the Netherlands concerning working on a commercial microscope, I made several basic changes to the microscope before the new test started. Wires leading the main signal in the STM (from sample, tip and z-piaza) were replaced from a double-wire phosphor wires to coaxial stainless steel wires resulting in greater

signal purity. Furthermore, support plates have been designed and manufactured to guide the cables along the head. This prevents the creation of unwanted thermal and vibration bridge between the microscope head and the radiation shield. The microscope was then assembled and tested. In the course of testing, a number of problems have been identified and eliminated, which prevented the proper functioning of the STM. Few examples of the problems: a broken coaxial cable insulation, the electrical shortcut of the cables from the scanner in the clutch outside of the microscope, the insufficient grounding of the microscope head, the insufficient vibration damping. After finding and solving all of the problems, the atomic resolution was measured, which proved the microscope's functionality. Afterwards the scanner was calibrated. The latest tests were conducted in the vacuum chamber under the UHV conditions. In the test, the step edge of the HOPG was measured together with the record of the vibration spectrum. When the vibration spectrum was compared with the vibration spectrum of the STM in situation when the atomic resolution was measured, no significant difference was found. Therefore the microscope was labeled as fully functional even under vacuum conditions. However, testing of the experimental LT-STM showed few limitations of the old transport system. Therefore, new design of the sample holder, tip holder and the pallet for tip transfer was created.

The last section of the second part is focused on testing of the low-temperature systems of the experimental LT-STM - the flow and the stationary cryostat. The test of the flow cryostat was done in the academy of science at their special LT chamber. After 8 hours of cooling with liquid nitrogen, a temperature of 120 K on the samples was reached, and by cooling the microscope by liquid helium a temperature of less than 33 K was observed. In the test, serious technical deficiencies of the cryostats were discovered that would not allow cryostat to be connected to original microscope chamber. Therefore, the necessary modifications were proposed and the second cryostat (Stationary) was tested. The stationary cryostat was mounted to the microscope chamber and the minimal temperature 112 K was achieved during cooling on the sample. However, the problem with the microscope wires which lead from room temperature to the microscope head. Because of that for future test it was proposes to attache the wires to the radiation shield before connecting them to the microscope head.

BIBLIOGRAPHY

[1] FRANK, L. and J. KRÁL. *Metody analýzy povrchů: iontové, sondové a speciální metody*. Praha: Academia, 2002. ISBN 8020005943.

[2] FUKA, J. and B. HAVELKA. *Optika a atomová fyzika I. Optika*. First Edition. Praha: SPN, 1963. ISBN 20460563.

[3] YOUNG, R., J. WARD and F. SCIRE. The Topografiner: An Instrument for Measuring Surface Microtopography. *Review of Scientific Instruments*. 1972, vol. 43, pp. 999. Available from doi: 10.1063/1.1685846.

[4] BINNIG, G., H. ROHRER and E. WEIBEL. Surface Studies by Scanning Tunneling Microscopy. *Physical Review Letters*. 1982, vol. 49, pp. 57. Available from doi: 10.1103/PhysRevLett.49.57.

[5] MEYER, E., H. J. HUG and R. BENNEWITS. *Scanning probe microscopy: the lab on a tip*. Berlin: Springer, 2004. ISBN 3540431802.

[6] The Nobel Prize in Physics 1986. In: *Nobelprize.org* [online]. [2017-12-05], Available from: `http://www.nobelprize.org/nobel_prizes/physics/laureates/1986/`.

[7] CHEN, C. J. *Introduction to Scanning Tunneling Microscopy*. New York: University press, 2007. ISBN 9780199211500.

[8] HALLIDAY, D., R. RESNICK and J. WALKER. *Fyzika: vysokoškolská učebnice obecné fyziky*. Second editon. Brně: Prometheus, 2003. ISBN 8021418680.

[9] The Nobel Prize in Physics 1937. In: *Nobelprize.org* [online]. [2017-12-05]. Available from: `http://www.nobelprize.org/nobel_prizes/physics/laureates/1937/`.

[10] GRIFFITHS, D. J. *Introduction to Quantum Mechanics*. Second editon. New Jersey: Prentice Hall, 1994. ISBN 0131244051.

[11] KITTEL, C. *Introduction to Solid State Physics*. Eighth editon. Unifersity of California: John Wiley, 2004. ISBN 9789971511807.

[12] ZETTILI, N. *Quantum mechanics: concepts and applications*. Chichester: John Wiley & Sons, 2001. ISBN 0471489441.

[13] GARLEFF, J. K., *et al.* 2×1 reconstructed Si(111) surface: STM experiments versus ab initio calculations. *Physical Review B*. 2004, vol. 70, pp. 24. Available from doi: 10.1103/PhysRevB.70.245424.

[14] CHAIKA, A.N., et al. High resolution STM imaging with oriented single crystalline tips. *Applied Surface Science*. 2013, vol. 267, pp. 219-223. Available from doi: 10.1016/j.apsusc.2012.10.171.

[15] BARTELS, L., G. MEYER and K.H. RIEDER. Basic Steps of Lateral Manipulation of Single Atoms and Diatomic Clusters with a Scanning Tunneling Microscope Tip. *Physical Review Letters*. 1997, vol. 79, pp. 697. Available from doi: 10.1103/PhysRevLett.79.697.

[16] VOIGTLÄNDER, B. Scanning Probe Microscopy. Aachen:Springer, 2015. ISBN 9783662452400.

[17] WIESENDANGER, Roland. Spin mapping at the nanoscale and atomic scale. *Rev. Mod. Phys.* 2009, vol. 81, pp. 1495. Available from doi: 10.1103/RevModPhys.81.1495.

[18] SHIBATA, A., Y. KIMURA and K. TAKAYANAGI. In situ high-temperature STM study of the restructuring process on the Si(111)7 x 7 surface upon Ag deposition. *Surface Science.* 1994, vol. 303, pp. 161-170. Available from doi: 10.1016/0039-6028(94)90629-7.

[19] STONE, P., R. A. Bennett and M. Bowker. Reactive re-oxidation of reduced TiO2(110) surfaces demonstrated by high temperature STM movies. *New Journal of Physics 1.* 1999, vol. 1, pp. 8. Available from: http://stacks.iop.org/1367-2630/1/i=1/a=008

[20] SZKLARCZYK, M., *et al.* STM studies of p-Si(111) substrate in air and in electrolytic environment. *Surface Science.* 1990, vol. 237, pp. 305-3011. Available from doi: 10.1016/0039-6028(90)90542-G.

[21] COLLINS, G. Collins,K. BRADLEY and M. ISHIGAMI. Extreme Oxygen Sensitivity of Electronic Properties of Carbon Nanotubes. *Science magazine.* 2000, vol. 287, pp. 1801-1804. Available from doi: 10.1126/science.287.5459.1801.

[22] O'HANLON, J. F. *A user's guide to vacuum technology.* 3rd ed. Hoboken, NJ: Wiley-Interscience, 2003. ISBN 9780471270522.

[23] MICHAL, P. *Konstrukce nízkoteplotních ultravakuových rastrovacích sondových mikroskopů.*[Doctoral Thesis]. Brno, VUT, FSI, 2016.

[24] LIPPMANN, G. Principe de la conservation de l'electricitea ou second principe de la theorie des phenomenes electriques. *J. de Phys.* 1881, vol. 10, pp.381-394. Available from: `https://hal.archives-ouvertes.fr/jpa-00237824`.

[25] CURIE, J . and P. CURIE. Deformations electriques du quartz. *Comptes Rendus.* 1882, vol. 95, pp.914-917.

[26] VŮJTEK, M., R. KUBÍNEK and M. MAŠLÁŇ. *Nanoskopie.* Olomouc: Papírtisk, 2012. ISBN 9788024431024.

[27] FROLOV, K.V. and F FURMAN. *Applied theory of vibration isolation systems.* New York: Hemisphere pub., 1990. ISBN 0891166971.

[28] NEKULA, J. *Návrh rastrovacího tunelovacího mikroskopu STM.* [Master's Thesis] Brno: VUT, FSI, 2004.

[29] DAO, T. *Návrh nosné platformy pro nízkoteplotní UHV STM mikroskop.*[Master's Thesis] Brno, VUT, FSI, 2014.

[30] OKANO, M., et al. Vibration isolation for scanning tunneling microscopy. *Journal of Vacuum Science & Technology A.* 1987, vol. 5, pp. 3313-3320. Available from doi: 10.1116/1.574189.

[31] TICKOO, S. *Ansys Workbench 14.0 for Engineers and Designers.* Dreamtech press: CADCIM Technologies, 2012. ISBN 9350046746.

[32] CORBETT, J. P., *et al.* Advancement in tip etching for preparation of tunable size scanning tunneling microscopy tips. *Review of Scientific Instruments.* 2015, vol. 86, pp. 26104. Available from doi: 10.1063/1.4907706.

[33] STM cut-off method [online]. [2017-05-05]. Available from: http://faculty.cord.edu/jensen/STM.

[34] IBE, J. P., *et al.* On the electrochemical etching of tips for scanning tunneling microscopy. *Journal of Vacuum Science & Technology A*. 1990, vol. 8, pp. 3570-3577. Available from doi: 10.1116/1.576509.

[35] REN, B., G. PICARDI and B. PETTINGER. Preparation of gold tips suitable for tip-enhanced Raman spectroscopy and light emission by electrochemical etching. *Review of Scientific Instruments*. 2004, vol. 75, pp. 837-843. Available from doi: 10.1063/1.1688442.

[36] DUBRAVCOVÁ, V.. *Vákuová a ultravákuová technika*. Bratislava: Alfa, 1992. ISBN 8005010907.

[37] WESTON, G.F. *Ultrahigh vacuum practice*. Boston: Butterworths, 1985. ISBN 0408014857.

[38] KŘÍŽ, R. *Tabulky materiálů a předvýrobků pro strojírenství*. Ostrava: Montanex, 2001. ISBN 8072250442.

[39] Kapton® Polyimide film [online].[2017-05-05]. Available from: http://www.dupont.com/products-and-services/membranes-films/polyimide-films/brands/kapton-polyimide-film.html/.

[40] MACOR® Machinable Glass [online]. [2017-05-05]. Available from: https://www.corning.com/worldwide/en/products/advanced-optics/product-materials/specialty-glass-and-glass-ceramics/glass-ceramics/macor.html.

[41] LIGO vacuum compatible material list [online]. [2017-05-05]. Available from: http.//www.ligo.caltech.edu/docs/E/E960050-B/E960050-B.pdf.

[42] CRAWFORD, R. *Vibration isolation of large masses and vacuum chambers*. 1970. Available from: http://www.researchgate.net/.

[43] VON BERGMANN, K. *et al.* Observation of a Complex Nanoscale Magnetic Structure in a Hexagonal Fe Monolayer. *Physical Review Letters*. 2006, vol. 96, pp. 167230-167234. Available from doi: 10.1103/PhysRevLett.96.167203.

[44] HEINZE, S. *et al.* Spontaneous atomic-scale magnetic skyrmion lattice in two dimensions. *Nature Physics*. 2011, vol. 7, pp. 713-718. Available from doi: 10.1038/nphys2045.

[45] KHAJETOORIANS, A. *et al.* Atom-by-atom engineering and magnetometry of tailored nanomagnets. *Nature Physics*. 2012, vol. 8, pp. 459-503. Available from doi: 10.1038/nphys2299.

[46] EOM, D. *et al.* Persistent Superconductivity in Ultrathin Pb Films: A Scanning Tunneling Spectroscopy Study. *Phys Rev Lett.*. 2006, vol. 96, pp. 027005-027009. Available from doi: 10.1103/PhysRevLett.96.027005.

[47] HSU, Y., *et al.* Topological superconductivity in monolayer transition metal dichalcogenides. *Nature Communications*. 2017, vol. 8, pp. 14985-14991. Available from doi: 10.1038/ncomms14985.

[48] NADJ-PERGE, S., *et al.* Observation of Majorana fermions in ferromagnetic atomic chains on a superconductor. *Science*. 2014, vol. 346, pp. 602–607. Available from: doi: 10.1126/science.1259327.

[49] CAHLÍK, A. *Spectral analyzing and characterization of magnetic atoms and investigating superconducting films in low temperature STM.* [Master's Thesis] Brno: VUT, FSI, 2016.

[50] Omicron LT-STM [online]. [2017-05-05]. Available from: `http://www.scientaomicron.com/en/products/low-temperature-spm/instrumentconcepta`.

[51] LI BASSI, A., et al. Bulk Cr tips for scanning tunneling microscopy and spin-polarized scanning tunneling microscopy. *Applied Physics Letters.* 2007, vol. 91, pp. 173120-173124. Available from: doi: 10.1063/1.2800810.

[52] HUANG, D. *et al.* Etching of Cr tips for scanning tunneling microscopy of cleavable oxides. *Review of Scientific Instruments* . 2017, vol. 88, pp. 023705-023711. Available from: doi: 10.1063/1.4976567.

[53] IBE, J. P., *et al.* On the electrochemical etching of tips for scanning tunneling microscopy. *Journal of Vacuum Science & Technology A.* 1990, vol. 8, pp. 3570. Available from: doi: 10.1116/1.576509.

[54] ALBONETTI, C. *et al.* Electrochemical preparation of cobalt tips for scanning tunneling microscopy. *Review of Scientific Instruments.* 2002, vol. 73, pp. 4254. Available from: doi: 10.1063/1.1518127.

[55] Omicron etching station [online]. [2017-05-18]. Available from: `http://www.scientaomicron.com/en/products/w-tek-tip-etching-tool-/instrument-concept`.

[56] PAWLEY, J. *Handbook of Biological Confocal Microscopy.* Third edition University of Wisconsin, Madison: Springer Science+Business Media, 2006. ISBN 9780387455242.

[57] TATAU, N. and P. RUDOLPH. *Handbook of Crystal Growth: Bulk Crystal Growth.* Second edition. Germany: Elsevier, 2015. ISBN 9780444633033.

[58] CORAUX, J., *et al.* Structural Coherency of Graphene on Ir(111). *Nano letters.* 2008, vol. 8, pp. 565-570. Available from: doi: 10.1021/nl0728874.

[59] VON BERGMANN, K., *et al.* Complex magnetism of the Fe monolayer on Ir(111). *New Journal of Physics.* 2007, vol. 9, pp. 396. Available from: doi: 10.1088/1367-2630/9/10/396.

[60] WXSM software [online]. [2017-05-05]. Available from: `http://www.wsxmsolutions.com/`.

[61] VON BERGMANN, K., *et al.* Observation of a Complex Nanoscale Magnetic Structure in a Hexagonal Fe Monolayer. *Physical Review Letters.* 2006, vol. 96, pp. 167203. Available from: doi: 10.1103/PhysRevLett.96.167203.

[62] GERYK, M. *Konstrukce ultravakuové komory pro sledování struktury povrchů pevných látek metodou LEED a STM/AFM.* VUT Brno. [Master's Thesis] Brno: VUT, FSI, 2001.

[63] SOJKA, A. *Sestavení a testování nízkoteplotního mikroskopu STM.* [Bachelor's Thesis] Brno: VUT, FSI, 2015.

[64] Attocube: ANS Linear Positioners. *Attocube* [online]. [2017-05-04]. Available from: `http://www.attocube.com/attomotion/premium-line/{#}Scanner`.

[65] PT-100. *Picotech* [online]. 2017 [2017-05-05]. Available from: `https://www.picotech.com/library/application-note/pt100-platinum-resistance-thermometers`.

[66] HEANEY, M. B. *Electrical Conductivity and Resistivity*. 2003. CRC Press, 2003.

[67] SMD 2k70 rezistor [2015-05-23]. Available from: http://www.ges.cz/cz/cr1206-2k70-5-GES05300097.html.

[68] EPO-TEK H77 [online]. [2015-05-25]. Available from: http://www.epotek.com/site/component/products/productdetail.html?cid%5B0%5D=133.

[69] PZT-4. *Eblproducts* [online]. [2017-05-06]. Available from: http://www.eblproducts.com/piezotube.html.

[70] Piezoceramic Tubes [online]. [2017-02-03]. Available from: http://www.eblproducts.com/piezotube.html.

[71] CHEN, C. J. Electromechanical deflections of piezoelectric tubes with quartered electrodes. *Applied Physics Letters*. 1992, vol. 60, pp. 132. Available from: doi:10.1063/1.107348.

[72] EPO-TEK H22 [online]. [2015-05-25]. Available from: http://www.epotek.com/site/component/products/productdetail.html?cid%5B0%5D=95.

[73] Lake Shore: Cryogenic Accessories [online]. [2017-05-04]. Available from: http://www.lakeshore.com/products/Cryogenic-Accessories/Pages/Model-Landing.aspx.

[74] Ultra miniature coaxial cable SS. *Lakeshore* [online]. [2015-05-31]. Available from: http://www.lakeshore.com/products/cryogenic-accessories/cable/pages/overview.aspx.

[75] Wires. [online]. [2015-05-31]. Available from: http://www.lakeshore.com/Documents/LSTC_wire_l.pdf.

[76] Current Amplifier. [online]. 2017 [2017-06-02]. Available from: http://www.femto.de/de/produkte/stromverstaerker/variable-verstaerkung-bis-500-khz-dlpca.html.

[77] ŠULC, D., P. WEITHEMEIR and M. PAVERA. Vývoj univerzálního zařízení pro rastrovací sondové mikroskopy. *Jemná mechanika a optika*. 2014, vol. 6, pp. 1610-1615.

[78] GXSM [online]. [2015-05-27]. Available from: http://gxsm.sourceforge.net/.

[79] HOPG [online]. [2017-05-25]. Available from: http://www.brukerafmprobes.com/a-3516-hopg.aspx.

[80] LYDING, J. W., *et al.* Variable-temperature scanning tunneling microscope*Review of scientific instruments*. 1988, vol. 59, pp. 1897. Available from: doi: 10.1063/1.1140047.

[81] Cernox. [online]. [2015-05-31]. Available from: http://www.lakeshore.com/Documents/LSTC_Cernox_l.pdf.

[82] *Model 350 Cryogenic Temperature Controller* [online]. [2017-06-03]. Available from: http://www.lakeshore.com/products/Cryogenic-Temperature-Controllers/Model-350/Pages/Overview.aspx.

[83] TERSOFF, J. and D. R. HAMANN. Theory and Application for the Scanning Tunneling Microscope. *Phys. Rev. Lett.* 1983, vol. 50, pp. 1998–2001. Available from: doi:10.1103/PhysRevLett.50.1998.

[84] NAGAHARA, L. A., T. Thundat, and S. M. Lindsay. Preparation and characterization of STM tips for electrochemical studies. *Review of scientific instruments*. 1989, vol. 60, pp. 3128. Available from: doi: 10.1063/1.1140590.

[85] LÜTH, H. *Surfaces and interfaces of solids*. Berlin: Springer-Verlag, 1993. ISBN 3540568409.

[86] STROSCIO, J. A. Controlling the Dynamics of a Single Atom in Lateral Atom Manipulation. *Science*. 2004, vol. 306, pp. 5694. Available from: doi: 10.1126/science.1102370.

[87] FILIP, L. *Development and application of an UHV SPM microscope*. [Doctoral Thesis]. Brno, VUT, FSI, 2005.

[88] GROSZKOWSKI, J. *Technika vysokého vakua*. Praha: SNTL - Nakladatelství technické literatury, 1981. ISBN 000251437.

[89] VOŇKA, J. *Desing and verification of low temperature part of UHV-STM Microscope*. [Master's Thesis] Brno: VUT, FSI, 2013.

[90] SCHMID, M. and P. VARGA. Analysis of vibration-isolating systems for scanning tunneling microscopes. *Ultramicroscopy*. 1992, vol. 42-44, pp. 1610-1615. Available from: doi: 10.1016/0304-3991(92)90493-4.

[91] ČEŠPÍRO, Z. *Vakuová technika*. 1973. Praha: České vysoké učení v Praze, 1973. ISBN 5960973.

[92] NOVÁČEK, Z. *Vývoj instrumentálního zařízení pro výzkum nanostruktur*. [Doctoral Thesis]. Brno, VUT, FSI, 2014.

[93] Autodesk Inventor Professional 2015 [online]. [2015-05-31]. Available from: `http://www.autodesk.cz/products/inventor`.

[94] Coaxial Pincer Grip Wobble Sticks [online]. [2015-05-06]. Available from: `http://www.vgscienta.com/productlist.aspx?MID=376&IID=564`.

LIST OF USED ABBREVIATIONS

SPM ..... Scanning Probe Microscopy

LT-STM ..... Low Temperature Scanning Tunneling Microscopy

STM ..... Scanning Tunneling Microscopy

STS..... Scanning Tunneling Spectroscopy

SP-STM..... Spin polarized

AFM ..... Atomic Force Microscopy

NSOM ..... Near-Field Scanning Optical microscopy

MFM ..... Magnetic Force Microscopy

EFM ..... Electrostatic Force Microscopy

CHM ..... Constant Height Mode

CCM ..... Constant Current Mode

SEM ..... Scanning Electron Microscope

HEED ..... Hight-Energy Electron Diffraction

UHV ..... Ultra Hight Vacuum

SMD ..... Surface Mount Device

PCB ..... Printed cirtuit board

HOPG ..... Highly Oriented Pyrolytic Graphite

PEEK ..... Polyether ether ketone

FFT ..... Fast Fourier Transformation

LN/LHe ..... Liquid Nitrogen/Liquid Helium

LDOS ..... Local Density of States

ML ..... Monolayer

APPENDIX

CD with the CAD models and drawings

Drawing No.	List of Drawing
1.01	Sample holder
1.01.01	Pallet base
1.01.02	Counterpart
1.01.03	Anvil
1.01.04	Ceramic
1.02	Transfer Palette for Tip Holder
1.02.01	Pallet base
1.02.02	Counterpart
1.02.03	Spacer
1.03	Tip Holder